LIMITATION ON THE USE OF A SPACEBORNE SAR FOR RAIN MEASUREMENTS

Atiq Ahamad

Radar Systems and Remote Sensing Laboratory
Department of Electrical Engineering and Computer Science, University of Kansas
2291 Irving Hill Road, Lawrence, Kansas 66045-2969
TEL: 913/864-4835 * FAX: 913/864-7789 * OMNET: KANSAS.U.RSL

RSL Technical Report 8370-4

June 1994

Sponsored by:

NASA Jet Propulsion Laboratory
Pasadena CA 91109

Document No. 958522

TABLE OF CONTENTS

CHAPTER 4 CALCULATIONS AT OFF-VERTICAL ANGLES

CHAPTER 5 CALCULATION AT VERTICAL

CHAPTER 6 ESTIMATION OF THE SIGNAL IN PRESENCE OF CLUTTER

CHAPTER 7 CONCLUSIONS AND RECOMMENDATIONS

LIST OF FIGURES

ABSTRACT

A proof-of-concept experiment for remote sensing of precipitation by SAR is part of the SIR-C/X-SAR experiment. This thesis presents a feasibility study and recommendations for detection of precipitation using SIR-C/X-SAR. The principal limitation to rain measurement from a spaceborne SAR is the poor SCR (signal-to-clutter ratio). This is in part due to the system configuration and largely due to the large magnitude of echoes associated with the surface component. Two geometries apply; off-vertical and vertical pointing angles. Here we present calculations for both.

With vertical geometry a large clutter component is associated with range sidelobes of the chirped transmitter pulse. To overcome this problem a narrow transmitted pulse (3 μsec) processed without dechirping was used. Since the magnitude of the clutter over the ocean is high it is recommended that data in the chirped mode be obtained over the forest due to the significantly lower backscatter associated with it at nadir. With these recommendations, at nadir, it is believed that rain rates > 5 mm/hr may be detected. The use of a better weighting function that gives lower sidelobe levels than that used (a raised $\cos^2$) is also recommended.

At off-vertical look angles all the range cells have a large clutter component associated with them due to the geometry. The use of higher angles of incidence (θ > 60°) is recommended because of better SCR at these angles. With this recommendation, at off-vertical, it is believed that rain rates > 10 mm/hr may be detected.

Various other techniques are described and recommended to improve the minimum detectable precipitation rate. These include trying to subtract the estimate of the clutter from the combined signal and clutter and trying to separate the Doppler of the rain echo and the surface echo. With these recommendations it is believed that it is possible to detect precipitation as low as 1 mm /hr at vertical and > 5 mm/hr at off-vertical look angles.

CHAPTER I
INTRODUCTION

1.1 INTRODUCTION

The world ocean and water in and on land makes the climate of the earth uniquely suited for the sustenance of life. The process of evaporation and condensation of water vapor is essential for earth's habitability. Rainfall is clearly central to water supply. Cloud radiation and fresh water from the rainfall may significantly affect the ocean circulation and marine biomass, while variations in low-level winds may determine up-welling and movement of nutrient-rich water (Simpson, 1988). On an average, about 50% of the earth's surface is covered by clouds but the ratio of the rain to the cloud area is seldom larger than 10% (Griffith et al., 1978). Although these estimates place an upper bound of 5% on the earth's surface receiving rain at a given time, the actual percentage is much less (Barrett and Martin 1981). For the tropical zone between 30° N and 30° S, the occurrence of rain has been estimated to be about 4%, accounting for more than half the earth's rainfall (Thiele, 1987). Although contours of the global mean annual precipitation have been constructed over oceans and remote land areas, the annual rainfall at a particular location probably is known only within a factor of 2, at best (Thiele ,1987).

One of the most sought after characteristics of precipitation is the rainfall rate, R_r, defined as the volume of liquid water that falls through a unit area per unit time and normally expressed in units of mm per hour. Though rain events are dominated by lighter rainfall rates, higher rain rates account for most of the total liquid water reaching the surface. From approximate global distribution of rainfall, in the region

of highest rain rate, the of percentage time in a year the rainfall exceeds 50 mm/hr is 0.1%, or 526 min per year; it exceeds 150 mm/hr only for about 53 min annually (Crane and Blood, 1979). The contribution from the various rain rate categories to the total rainfall can be calculated from the probability density function (PDF) for the rain rate R_r. The relative contributions of the various rain rate categories to the total rainfall are obtained by multiplying the PDF by the rain rate, R_r, and integrating from zero to R_r. Available data show that the dynamic range required to characterize ocean precipitation in the tropics is less stringent than over areas with intense local convection. For example, in the GATE program, a radar that could accurately estimate rain rates between 2 mm/hr and 40 mm/hr would account for about 84 % of the total rainfall in a typical GATE area, but about only 64 % of the total rain volume over Texas, which has local convection (Chiu, 1988). However it appears that there is a correlation between the fractional area over which the rain rate exceeds a certain threshold on one hand and area-averaged rain rate on the other. If such relationships can be tuned to local climatology, for those applications in which area averaged rain rates are of primary importance, a large dynamic range may not be required.

Most first-order weather service sites have the tipping bucket and the universal weighing-gauge precipitation monitors. The tipping-bucket gauges generally accumulate the number of 0.01 inch precipitation events in a day which they utilize to compare with the accumulation in other gauges. The rain rate estimate comes from the time between these tips. The universal weighing gauge is also capable of

providing rain rate information and is the main instrument utilized to provide the 5-minute to 1-hour precipitation data. By measuring the slope of the strip chart on the gauge, the rain rate may be obtained to at-least 5-minute resolution and even 1-minute rain rates may be inferred from some charts. These charts are a good source of information for short-duration rainfall. Several investigators have developed more accurate techniques of estimating rain rate distributions directly from the rain gauges with resolution as low as 1 minute.

1.2 MICROWAVE RAINFALL MEASUREMENT

Rain drops, for many purposes, may be considered to be spherical under normal conditions (Battan,1973). Mie first devised a general theory that describes the scattering of a plane wave by a sphere. Hence, we are able to apply the Mie scattering theory to backscattering from rain drops with little approximation. For wavelengths under consideration (3 to 6 cm) it is usually possible to use the Rayleigh approximation (Battan, 1973). Various published results may be used to calculate the magnitude of the backscatter from the rain drops. Here, we are looking for an empirical relationship between the reflectivity / attenuation and the rain rate, to allow rain rate determination using any one of the available rain-retrieval algorithms. An accurate estimate of the dropsize distribution is crucial in determining these empirical relations. Observations of the dropsize distribution as a function of precipitation

intensity have been made in a variety of places and in various types of precipitation: widespread rain and snow from stratiform clouds, showery and orographic precipitation, etc. Because of the large variations observed in both time and space, the analyses of the data have been along statistical lines (Battan,1973).

The dropsize distribution most widely used in the literature are the Laws-Parsons and Marshall-Palmer distributions, which compare reasonably well with one another. One of the major attributes of the Laws and Parsons dropsize distribution (Table 2.1) is that it covers a wide range of precipitation rates. Later chapters will discuss the theoretical relationship between the dropsize distribution and the empirical relationship and reduce it to a form that suits our purpose.

Microwave rainfall retrieval techniques may be classified into

1. Passive rainfall measurements
2. Active rainfall measurements
3. Hybrid rainfall measurements.

1.21 PASSIVE MICROWAVE RAINFALL RETRIEVAL

The ability of the microwave radiometer to extract rainfall depends heavily upon the contrast between the observed brightness temperatures over raining and the non-raining regions. The power emitted by a body in radiative equilibrium is a linear function of apparent or brightness temperature in the microwave region (Simpson, 1988).

Due to the low emissivity (about 0.5) of the ocean, the ocean brightness temperature is very cold (< 150° K) (Ulaby, et al., 1986), and offers an ideal background to observe the emission from the rain at its equilibrium temperature. Land, in contrast has an emissivity of 0.7-0.9 which varies with vegetation, soil moisture, and other parameters. Thus, the brightness temperature measurements against warm and variable background appear to be inapplicable for retrieving atmospheric constituents such as rainfall.

The absorption, emission, and scattering properties of the hydrometeors depend strongly on the frequency. Low frequencies are best described in terms of their absorption/emission effects, while high frequencies are best described by their scattering effects (Ulaby, et.al, 1981). Most recent passive rainfall retrieval techniques, however, rely on multichannel approaches that utilize the known scattering-to-emission ratios at the various frequencies to infer rainfall rate.

The microwave brightness temperature depends on both the rain rate and many other atmospheric and cloud factors such as raindrop size distribution, cloud droplets, rain layer thickness, ice above the rain, inhomogeneities within the field of view, water vapor, wind speed at the ocean surface, and sea surface temperature. Multichannel techniques can retrieve some parameters along with the rainfall rate, but the behavior of the remaining parameters must satisfy some assumptions.

Various algorithms exist that utilize the brightness temperature to estimate the rainfall rate, of these:

Decision-Tree algorithm (Kummerow, 1987) estimates the rain rate by examining the brightness temperature at several frequencies. Theory and observation confirm that the brightness temperature over the ocean tend to increase with the thermal emission for low rain rates, saturate and finally decrease due to the scattering from large drops and ice. A given brightness temperature at a given frequency will, in general, correspond to two rain rates. The examination of the brightness temperatures at several frequencies resolves this ambiguity.

Dual-Polarization algorithm (Spencer, 1986) uses the polarization to resolve the ambiguity between low brightness temperatures produced by the precipitation and that produced by the ocean surface. The ocean surface, when viewed obliquely, produces radiance that is much more polarized than the precipitation.

Multichannel Statistical methods (Olson, 1986) use statistical radiative-transfer models to extract the rainfall rate from the measured brightness temperature. These models allow the prediction of up-welling brightness temperatures for any combination of atmospheric and cloud parameters. Direct approaches minimize the difference in observed and calculated brightness temperature by varying the model. Statistical techniques use model-generated brightness-temperature/rainfall relations.

1.22 ACTIVE-MICROWAVE RAINFALL RETRIEVAL

Active rainfall retrieval algorithms are generally divided into three categories. At smaller rain rates, where attenuation is somewhat insignificant, algorithms based

on backscatter power work best. Attenuation based algorithms include the surface-reference technique (Meneghini, 1983), the dual-wavelength surface-reference technique (Meneghini, 1987), the standard dual-wavelength technique (Meneghini, 1987), the height-area rainfall-threshold technique (Atlas, 1988), and the mirror-image method (Meneghini, 1985). The least squares algorithm (North, 1988; Fujita, 1983; Kieu, 1992) estimates the rain rate profile by minimizing the difference in the profiles of the observed and estimated received powers.

1.23 HYBRID MICROWAVE RAINFALL RETRIEVAL

Attempts to combine radar and microwave radiometry retrieval have been successful. The calculated brightness temperatures from airborne radar data (Simpson, 1988) agrees with the observed brightness temperatures. The multichannel linear rainfall technique described depends largely on the construction of cloud models that can accurately represent the observed brightness temperatures. With the correct model, results can be within 20 % for rainfall over an individual footprint (Weinman, 1989).

The combination of the radar and the radiometer measurements, which places constraints on the radar equation, can yield a vertical hydrometeor profile from a single-wavelength radar. The two major constraints are the surface rainfall rate and the path-integrated extinction. The extinction coefficients near the surface can come roughly from the mean surface-rainfall rate obtained from the radiometer. The

extinction coefficients become boundary condition on the radar equation. The path-integrated extinction from the approximate hydrometeor profile derived from passive radiometry can be used as a constraint on the radar equation.

Visible and IR radiometry is also widely used to confirm the presence of the clouds and measure their heights. The rain estimates in the VIS / IR radiometer are mainly from cloud observations. There is considerable interest in this technique because of the need for high spatial and temporal resolution of the precipitation events. Moreover, these methods can be used with geostationary satellites to obtain continuous coverage.

Satellite IR radiometers can differentiate between the convective and stratiform rainy areas. The convective stratiform technique attempts to define the convective areas as those with relative minima in the IR temperature field, and attempts to screen out thin cirrus. The computed anvil background temperature determines the stratiform raining area.

1.24 SPACEBORNE RAIN RETRIEVAL

It is evident that the precipitation variability apparently coupled with the changes in the underlying surface (particularly sea surface temperature) is associated with significant alteration in short-term climate, initiated in the tropics, which may lead to hemisphere-wide alteration in wind patterns and rainfall. Unfortunately the difficulty involved in accurately predicting this precipitation is an obstacle in

advancing understanding and prediction in this crucial portion of the earth system. Because of the inaccessibility of ground based sensors and the high cost of the surface radar networks, spaceborne measurements offer the only means to obtain global rainfall data.

The need for global precipitation data doesn't in itself warrant the use of spaceborne radars. To justify its use requires that it be technologically feasible and cost effective in the sense that it cannot be duplicated by a more reliable or less expensive sensor. The unique features of the radar are well recognized. Unlike the lidar, it can penetrate through rain and cloud; unlike the radiometer it can vertically profile the rain and its sensitivity is not degraded by the high emissivity of a land background. While these benefits have long been recognized, in the absence of the necessary technology they are merely potential advantages. Without the advances that have occurred in the efficiency and reliability of the power amplifiers in the microwave and millimeter wave region, in low noise receivers, and antenna technology, spaceborne radars would suffer from poor sensitivity and reliability and limited scanning capability.

One other reason for renewed interest in spaceborne radars is the change in the attitude which views the radar as one among a set of complementary sensors on the spacecraft. The sensors on the orbiter, in turn, are treated as one of the many types of observation platforms, which include airborne radars and radiometers, ground based radars and rain gauge networks, and geosynchronous weather satellites. Although this

change in thinking doesn't solve the inherent limitations of the spaceborne radar it does provide a well defined role where its capabilities may be exploited with modest implementation.

Although there is abundant literature on the measurement of precipitation from space using visible and IR sensors, microwave radiometry and radar (Atlas and Thiele, 1981), none of it has been demonstrated adequately. Atlas and Moore (1987) suggest the use of spaceborne SAR for rain measurements. Atlas et al. (1977) reported actual detection of precipitation by an airborne SAR.

1.3 CHARACTERISTICS OF PRECIPITATION

Rainfall measurements from spaceborne platforms will improve our understanding of the hydrological cycle, atmospheric circulation, climatological models, and mesoscale rainstorm characteristics. However, no single model equation or set of parameters can be used to describe all forms of precipitation. To better understand and accurately apply the available models it is necessary to discuss the various precipitation types. For our interest we will be looking into the characteristics of:

1. Stratiform precipitation.
2. Convective precipitation.
3. Hurricane precipitation.

1.31 CHARACTERISTICS OF STRATIFORM PRECIPITATION

The life cycle of mesoscale convective systems consists of four stages: 1. Formative, 2. Intensifying, 3. Mature, and, 4. Dissipating (Kieu, 1991). The convective cells dominate the total rain amounts in the formative stage (typically 2-6 hr). During the intensifying stage, the stratiform precipitation begins to account for more of the total rain. In the mature stage, the stratiform component is equal to or greater than the convective component, as the total rain gradually decreases. The stratiform rain accounts for roughly 40% of the total rain during the lifetime of the weather systems.

In the mid-latitude regions, stratiform rainfall typically has horizontal extent of hundreds of kilometers, durations exceeding one hour, and rain rates less than about 25 mm/hr. The spatial distribution of the total rainfall from one of these storms is fairly uniform. The rain rate averaged over several hours is usually similar for ground sites located up to tens of kilometers apart. This rain type usually occurs during spring and fall months and results, because of the cooler temperatures, in vertical heights of 4 to 6 km.

In the stratiform region, the mesoscale updraft (Gamache, 1982) has been found between 20 to 40 cm/s above the altitude of the 0° C isotherm and a down-draft of nearly equal magnitude below this altitude. Using VAD (velocity-azimuth display) in the different portions of the stratiform area, the horizontal boundary between the mesoscale updraft and down-draft was found to occur just below the altitude of the

0° C isotherm (3.8 km). The magnitude of these mesoscale vertical motions in the stratiform region was 30 to 40 cm/s above the 0° C isotherm, and -10 to -30 cm/s below it (Chong, 1987).

1.32 CHARACTERISTICS OF CONVECTIVE PRECIPITATION

Convective rains arise because of the vertical atmospheric motions resulting in vertical transport and mixing. Strong vertical motions characterize convective cells, while weaker mesoscale motions are present in the stratiform region. The convective flow occurs in a cell whose horizontal extent is several kilometers across. The cell usually extends to heights greater than the average freezing layer at a given location because of the convective up-welling. The cell may be isolated or embedded in a thunderstorm region associated with a passing front. Because of the motion of the front and the sliding motion of the cell along the front, this high rate usually lasts only for several minutes. These rains are the most common source of high rain rates in the U.S and Canada (Kieu,1991).

In studies of convective systems, maximum reflectivities exceed 45 dBZ*. The updraft maximum typically occurred at a height of 2.1 km. The average maximum updrafts are as high as 17 m/s. Other studies of convective systems (Chong, 1987) show that the maximum convective updrafts of up to 10 m/s were at 2.5 km along the

* Z is the reflectivity from the rain drops in the unit volume mm^6/m^3.

leading edge of the system, with a secondary maximum of 6-10 m/s above 5 km altitude 20-30 km behind the leading edge. The maximum convective down-drafts were 4 m/s.

Radars operating at non-attenuating frequencies have been used to study both the horizontal and the vertical components of the convective rain systems. Crane and Blood report that rain rate variations of 100:1 could be observed over a range of 10 km for a shower containing four intense cells. Similar measurements were made by Goldhirsh (1976), at Wallops Islands, VA. Goldhirsh (1976) also observed that the intense rain cells are elongated along the direction of motion. This direction correlated well with the average or median wind direction.

1.33 CHARACTERISTICS OF HURRICANE PRECIPITATION

Tropical cyclonic storms (Hurricanes) sometimes pass over the eastern seaboard during the August-October time period. These circular storms are typically 50 to 200 km in diameter, move at 10-20 kilometers per hour, have extended melting-layer heights up to 8 km and have high (greater than 25 mm/hr) rain rates.

Experimental studies show the importance of predominantly stratiform precipitation surrounding the eyewall to the overall rainfall pattern of hurricanes. The eyewalls of hurricanes contain the heaviest rain rates, but encompass a relative small area. The precipitation in the surrounding region (out to 110 km), while having lower mean rain rates owing to its stratiform nature, covers much more area than the

eyewall. Up to 60 % of the rainfall within the inner region is predominantly stratiform precipitation in the region surrounding the eyewall. The eyewall rain rates increase as the storms intensify and the eyewall contracts. The increase in the mean eyewall rain rate is roughly balanced by the reduction in the eyewall area as the radius of the maximum reflectivity contracts.

1.4 SIR-C / X-SAR PRECIPITATION EXPERIMENT

The SIR-C/X-SAR precipitation experiment was proposed to study precipitation detection and measurement using the C- band channel of the Shuttle Imaging Radar (SIR) along with the X-band X-SAR. The prime objective of the experiment was to demonstrate that the spaceborne (SAR) rain measurement concept, which would be extremely useful for the design and development of future global rain mapping missions. Although for climatological purposes rainfall must be observed over a long period of time, the results obtained from this proof-of-concept experiment will be useful to the studies of short-term rain phenomena and for verification of the radar-based rain-retrieval algorithms. Two other important objectives of the experiment were to establish the feasibility of measuring the rainfall motion from the radar Doppler signals, and to determine the modification of the ocean surface-scattering properties by the impinging rain-drops.

It was expected that, with the SIR-C/X-SAR capabilities, quantitative rain backscatter measurements could be obtained in moderate to intense rain rate events.

By rotating the shuttle so that the antenna points to the vertical, it is possible to obtain the mean backscatter intensities from the rain-drops and the Doppler shift caused by the rainfall motion. With this observation geometry, it was expected to collect data that could demonstrate the use of the Synthetic Aperture Radar (SAR) technique to improve the along-track resolution. The SAR images obtained over the ocean during a rain storm could be used to study the changes in the surface characteristics due to the impinging rain drops. These results are expected to have important applications on the use of the ocean surface backscatter measurements for near surface wind estimation and for rain rate estimation using path-averaged attenuation. The rain data obtained by the SIR-C/X-SAR will constitute the first used and planned rainfall data set ever obtained from a spaceborne radar.

The anticipated results of this experiment are

- Quantitative evaluation of the rainfall rate.
- Quantitative measure of the average rainfall velocity.
- Quantitative measure of the height of the rain cloud.
- Determination of achievable spatial resolution for rainfall measurement applications using synthetic aperture synthesis.
- Quantitative measure of the modification in the ocean scattering mechanism as a result of the impinging raindrops, and comparison of such results with theory and previously obtained experimental data.
- Polarization signature of the ocean and the signature's variation in the presence of

precipitation.

1.5 ORGANIZATION OF THE THESIS

This thesis is based on the proposed SIR-C / X-SAR rain measurement experiment. After the experiment was accepted there arose a need for a feasibility study. This thesis presents the study and recommendations made for detection of precipitation from the spaceborne platform. The thesis is organized as follows;

Chapter 2 describes the concept of a synthetic-aperture radar and its ability to obtain better resolution compared to a real-aperture radar when the targets in the beam volume are correlated. However, when the targets have a random component the SAR fails in obtaining this fine resolution. It is shown that the resolution obtained by the SAR when the targets are not correlated is the same as that of a real aperture radar with the same parameters as that of the synthetic-aperture radar.

Chapter 3 describes the various rain and clutter models. It also describes the relationship between the empirical rain models and the radar measured parameters. The rain rates are related to the radar reflectivity and attenuation by the power laws. The presence of the melting layer and an absence of sufficient knowledge of its electrical characteristics further complicates matters. However reasonable approximations can be made to account for it. Various ocean and land clutter models

at both X- and C-bands are considered, but only those of interest to us are presented here. The equations describing these models have been verified by comparison to the SEASAT and ERS-1 data and with aircraft and land/tower-based data. These models are very close to experimental results.

Chapter 4 discusses the geometry of the off-vertical viewing angles and calculations of SNR and SCR at these angles. The study was based on the SIR-C / X-SAR experiment and it was seen that there are two possible approaches to the rain rate retrieval. In the off-vertical mode the geometry is complicated because of the large beamwidth in the vertical direction. It is seen that all the rain cells are associated with a clutter component. This necessitates the calculation of an important benchmark, signal-to-clutter ratio (SCR). Though the SCR is important, in that it gives the minimum detectable precipitation rate, the Signal-to-noise-ratio (SNR) is also important. This chapter has both SCR and SNR calculations at off-vertical look angles. It shows that for off-vertical look angles the minimum detectable rain rate over the ocean is very high. To detect moderate rain rates (>20 mm/hr) the angle of incidence must be high (> 60°).

Chapter 5 discusses the geometry at vertical viewing angles and the SNR and SCR at these angles. Here at vertical it is assumed that the surface returns are more or less unaffected by wind speed, direction etc. Though the sidelobes of the antenna do not

affect near-vertical precipitation measurement, the sidelobes of the pulse do affect it. With the raised $\cos^2$ weighting used, the range sidelobes are high enough to affect the SCR over the ocean adversely. However, over the forest, due to the low σ^o associated with it at vertical, there is a good possibility of detecting low rain rates (> 5 mm/hr).

Chapter 6 proposes that, theoretically at-least, it may be possible to detect low rain rates even in the presence of a large clutter component. This is an extension of the estimation of a low power signal in the presence of noise if there are enough independent samples of the signal and noise. It is shown that the number of samples required for successful estimation is within reasonable bounds.

Chapter 7 discusses the assumptions made throughout the study and the conditions under which these assumptions may not hold. Also there are recommendations and comments about processing the rain data to accommodate these conditions.

CHAPTER II
SYNTHETIC APERTURE RADAR RESOLUTION

2.1 INTRODUCTION TO SYNTHETIC APERTURE RADAR (SAR)

Synthetic aperture is a radar technique, implemented from an aircraft or an spacecraft, in which the effective synthesized antenna aperture is much larger than the real antenna. The radar motion is a prerequisite of the SAR technique. There are several ways to consider a SAR, each which lead to a different implementation of the processor. The synthetic aperture is so long that it is necessary to focus the beam to the point where the target is located, much as a camera is being focussed to near objects. In an analogy with the camera we may say that the lens focussed at infinity is the normal condition for an antenna. A lens focussed on a nearby object is analogous to the focussed synthetic antenna commonly used in the SAR.

SAR is normally used to image the surface. Any moving object generate Doppler shifts that can compete with the Doppler generated by the radar motion; since the Doppler generated by radar motion is the key to SAR operation, it is difficult to overcome the problem of motion of the target in the beam volume.

SAR signal processing is coherent phase compensation that corrects for the phase-shift history of the signal reflected from a specific point on the ground during the radar motion. With this compensation, only returns from that point are constructively added during the entire observation time.

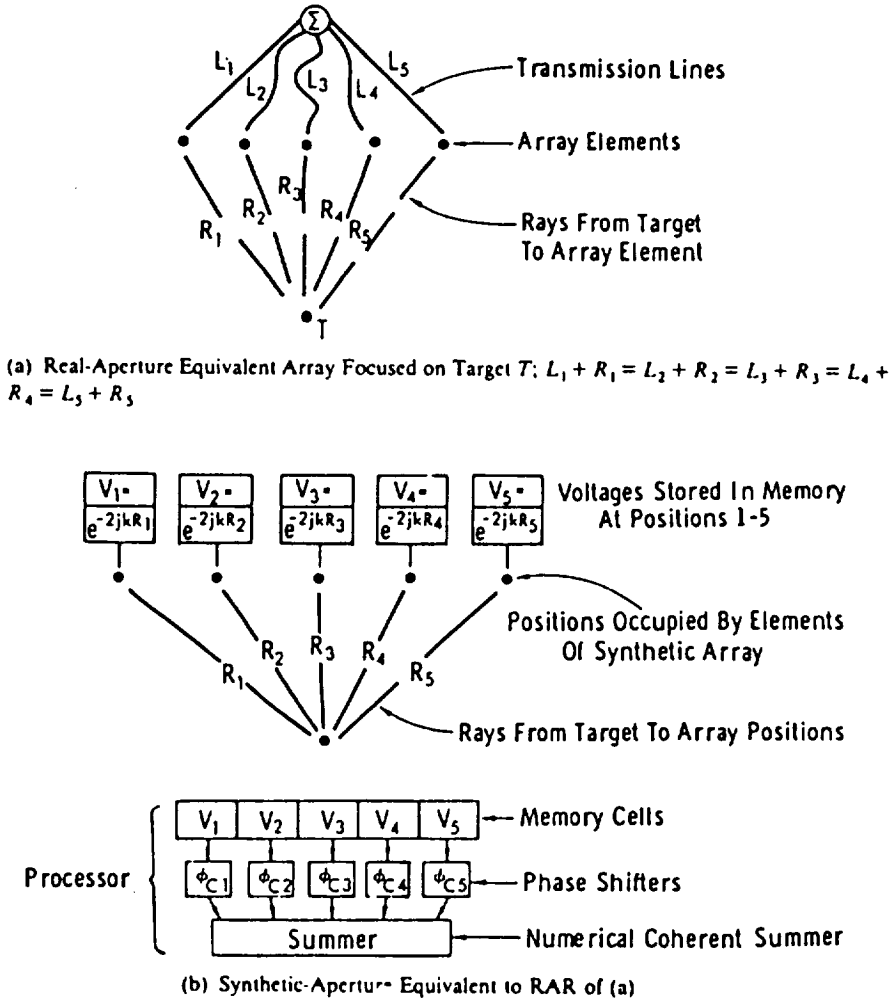

Fig. 2.1 Concept of the synthetic aperture. (Ulaby et al., 1982)

2.2 SYNTHESIZED APERTURE

To illustrate the concept of the synthetic-aperture, consider Fig. 2.1(a). The figure shows how one can build a real-aperture array of five elements focussed on the target T. Each element in the array is connected to a summing point, and all the voltages from different elements are added together at that point. The length of the transmission lines connecting each of the elements of the array to the summing point are based on the distance to the target and the position of the particular element in the array. The phase delay for each signal arriving to the summing point from the element must be the same if the total contribution is to be added in phase. When the signals add in phase the array is said to be focussed at that target point. This means that the equivalent total distance from the target to the summing point must be the same for every element, so that

$$L_1 + R_1 = L_2 + R_2 = L_3 + R_3 = L_4 + R_4 = L_5 + R_5.$$

The lengths L_i are the "equivalent free-space lengths " of the transmission line (i.e. lengths if the phase velocity in the transmission line is the same as that for the wave in space). During transmission, the signals all originate from the summing point for reception, so that during transmission the phase shift along each path is the same as that along every other path. Consequently, for the location of the target T, the total round-trip phase shift is the same for each element, and the electric fields from the different elements all add in phase. For any other point in front of the antenna, the distances between the target and the summing point differ, so the contributions from

the different array elements differ in phase, and the output is not as much as it is for a target located at the focal point T. In actual real-aperture antennas, the lengths L_1 to L_5 may not be as indicated but, may differ by a wavelength or several wavelengths in such a way that the phase relationship is maintained.

We may extend the concept of the real-aperture equivalent focussed array for a moving antenna by storing the signal voltages from the target T in memory locations as shown in Fig. 2.1(b). Here we assume that both the amplitude and the phase of the arriving signal are recorded. After all the memory locations are occupied, the contents of these locations are phase shifted by amounts needed to compensate for the differing distances R_1 through R_5. In essence we have multiplied the voltage V_i by e^{2jkR_i}. The phase correction $2kR_i$ accounts for the round-trip phase shift travelled by the signal from element i. The phasor sum of the signals is 5 times the value for one signal. If the same phase correction had been applied to signals received from different points, such a phase shift in space would be different than the correction, and the magnitude of the resultant phasor would be less. Hence, applying proper correction results in focussing the synthetic array at the location T.

In this implementation of the SAR there is no requirement for continuous motion from array element 1 to 2 to 3 to 4 to 5. The elements need not be uniformly spaced, and the motion may be such that the different element positions are not even occupied in any particular order. The only requirement is that the position of each element relative to the focal point T be known and the appropriate phase correction

applied in the processor.

Mathematically we can state this description of the total phase shift on path 1 of Fig. 2.1(a) as ϕ_{T1}, the phase shift in space on that path as ϕ_{S1}, and the phase shift on the transmission line as ϕ_{L1}. Thus we may write

$$\phi_{T1} = \phi_{L1} + \phi_{S1} = \phi_{Ti} = \phi_{Li} + \phi_{Si} = \phi_T \qquad (2.1)$$

Here the phase shift in space is

$$\phi_{Si} = 2\ k\ R_i \qquad (2.2)$$

and the phase shift on the transmission line is

$$\phi_{Li} = 2\ k_L\ L_i \qquad (2.3)$$

where k_L is the wave number for the transmission line.

The required phase shift in the transmission line is

$$\phi_{Li} = \phi_T - \phi_{Si} \qquad (2.4)$$

From (2.4) and (2.2) the length of the transmission line can be determined as

$$L_i = \frac{\phi_T - 2KR_i}{2K_L} \qquad (2.5)$$

The voltage received at the element i is therefore just

$$V_i = e^{-j2kR_i} = e^{-j\phi_{Si}} \qquad (2.6)$$

Therefore, we need a correction

$$\phi_{Ci} = \phi_{Li} = \phi_T - \phi_{Si} \qquad (2.7)$$

If we apply the correction, the resulting voltage at the summing point is

$$V = \sum_i e^{-j\phi_T} = 5\ e^{j\phi_T} \qquad (2.8)$$

(for the target at the focal point). For the synthetic-aperture it is usual to make $\phi_T = 0$ by making $\phi_{Ci} = -\phi_{Si}$.

Various schemes have been devised to perform true synthetic-aperture processing. In these processes one accumulates all the signals associated with different elements of the synthetic array and simultaneously multiplies with a correction factor. The processing may be performed in real time by multiplying each return at a particular range by different correction factors. The results of the multiplication can be stored in different locations corresponding to different synthetic-apertures being constructed.

To relate the synthesized aperture to the resolution, consider the geometry in the Fig. 2.2. The radar antenna on the airborne vehicle is shown in three positions A,B and C. At location A the forward edge of the beam first intercepts the target; at position B the beam is abreast the target and at position C the rear end of the beam is leaving the target. Thus the total possible length of the synthetic-aperture L_p is the

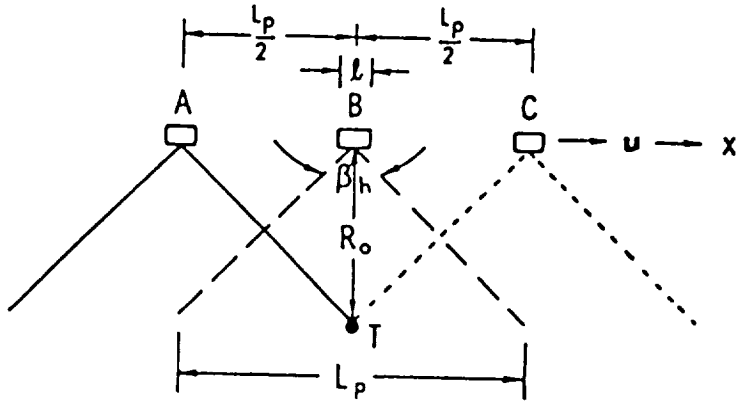

(a) Antenna Beams Illuminating Target at T

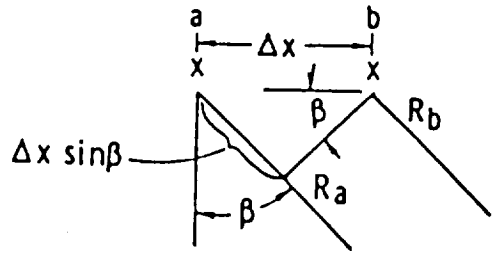

(b) Two Adjacent Elements in Synthetic Array

Fig. 2.2 General idea of the geometry of the Synthetic aperture (Ulaby et al., 1982)

resolution that would have been obtained by the real antenna in a real-aperture SLAR.

$$L_p = \beta_{hr} R_o \qquad (2.9)$$

Here β_{hr} is the horizontal or along track beamwidth of the real antenna, the subscript r is used to distinguish this beamwidth from the beamwidth of the synthetic-aperture antenna.

In part b of Fig. 2.2, two adjacent elements in the synthetic array separated by a distance Δx, are shown, with portions of the ray R_a and R_b going from these elements to the target. Since the elements are close together, the rays may be considered essentially parallel. Hence, the difference in the distance along the two rays is

$$R_a - R_b = \Delta x \sin\beta \qquad (2.10)$$

For the real aperture antenna the phase shift associated with this distance is

$$\Delta \phi_r = K(R_a - R_b) = k \Delta x \sin\beta \qquad (2.11)$$

For the synthetic-aperture array, the phase shift both as the wave goes from antenna to the target and as it returns from the target to antenna must be considered. Thus in this case

$$\Delta\phi_s = 2K(R_a - R_b) = 2k \Delta x \sin\beta \qquad (2.12)$$

For an antenna of length L (real or synthetic), where L is long enough that the beamwidth is small, the value of β associated with the first null is given by solving,

for the synthetic-aperture,

$$2kL \sin\beta \approx 2kL\,\beta = \pi \qquad (2.13)$$

and for the real aperture,

$$kL \sin\beta \approx kL\,\beta = \pi \qquad (2.14)$$

Hence the value of β associated with the first null for the synthetic-aperture is $\beta_s = \pi / 2$ Kl, whereas for the real aperture it is $\beta_r = \pi /$ Kl. This factor of two difference occurs at all angles associated with the pattern for the synthetic-aperture. Hence the beamwidth for the synthetic- aperture is half that of the real aperture having the same length.

The along track beamwidth β_{hs} for the synthetic-aperture is

$$\beta_{hs} = \frac{\lambda a_{hs}}{2L} \qquad (2.15)$$

where a_{hs} is the aperture illumination taper factor associated with the synthetic-aperture.

Using the expression for the beamwidth of the synthetic-aperture, the along-track resolution is obtained as

$$r_a = \beta_{hs} R = \frac{\lambda R}{2 L} a_{hs} \qquad (2.16)$$

This expression applies regardless of the actual length of the synthetic-aperture used. If the entire potential length L_p is used, the finest possible resolution r_{ap} for the SAR

is given by

$$r_{ap} = \frac{\lambda\, R a_{hs}}{2\, L_p} = \frac{\lambda\, a_{hs}}{2\, \beta_{hr}} \qquad (2.17)$$

Thus, the resolution attainable is inversely proportional to the beamwidth of the real antenna used in the SAR.

$$\beta_{hr} = a_{hr}\, \frac{\lambda}{l} \qquad (2.18)$$

where a_{hr} is the aperture illumination taper factor for the real antenna and l is its length. This value of β_{hr} may be used in (2.17) to obtain the potential synthetic-resolution in terms of the length of real antenna and the aperture taper factor as

$$r_{ap} = \frac{\lambda\, l\, a_{hs}}{2\, a_{hr}\, \lambda} \propto \frac{l}{2} \qquad (2.19)$$

when the illumination taper factors are the same.

Thus the finest possible resolution is just half the length of the real aperture. It is independent of the range and also the wavelength. The resolution r_{ap} is the finest possible resolution that one can attain with the synthetic-aperture radar having an antenna fixed to a spacecraft that is flying in a straight line, and for a stationary target.

2.3 RESOLUTION OF THE SAR

The range resolution achieved by the SAR is the same as that of the conventional side looking real-aperture radar (SLAR). The range resolution for the SAR is

$$r_R = \frac{c\,\tau_p}{2} \qquad (2.20)$$

where c is the speed of light and τ_p is the is the rectangular pulse width. The resolution on the ground is

$$r_y = \frac{c\,\tau_p}{2\,\sin\theta} \qquad (2.21)$$

where θ is the angle of incidence.

The resolution possible by the SAR in the azimuth direction is more complex. To obtain an expression for the azimuth resolution, let us consider the SAR as a focussed Doppler-beam- sharpening processor (see Fig.2.3). In Fig 2.3.(a) the radar is on the aircraft at a distance x_R away from the origin and at a height h. The coordinates of the radar are (x_R, 0, h). The coordinates of the target are (0, y_T, 0). The ellipse shown represents the half power contour on the ground of the beam of the real antenna carried by the aircraft. The solid outline surrounding the target and bounded in the x-direction by the edge of the beam, shows the area contributing to the return at a particular instant of time. Also shown are the contours of constant Doppler frequencies (isodops) surrounding the target, with spacing Δf_D.

A bandwidth B_{Df} of a Doppler filter is used for beam sharpening (Wiley, 1967). The Doppler frequency for the target in this case is given by

$$f_{dT} = \frac{-2\ u\ (x_R - x_T)}{\lambda\ R} \qquad \textbf{(2.23)}$$

The target location x_T is fixed, whereas the radar location x_R is varying. For the illustration the Doppler frequency is positive because x_R is negative. The Doppler frequency decreases linearly with the passage of the beam over the target, if we neglect the slight variation of the range.

Parts (b) - (f) of the figure illustrate the effect of the focussed Doppler beam-sharpening system as the target is successively illuminated first by the forward edge of the beam and later by other portions of the beam, until finally the beam passes it. The along-track length of the illuminated area on the ground is simply the resolution that would exist for the real-aperture radar having the same beamwidth.

$$r_{ar} = \beta_h\ R \qquad \textbf{(2.23)}$$

The total bandwidth of the Doppler-shifted signal that is received by the radar is the same as would be found for a real-aperture radar signal. It is given by

$$B_D = \frac{2\ u}{\lambda}\ \beta_h = \frac{2\ u\ r_{ar}}{\lambda\ R} \qquad \textbf{(2.24)}$$

where λ is the wavelength of operation, R is the slant range to the target, u is the velocity of the aircraft β_h is the horizontal beamwidth and r_{ar} is the azimuth resolution

of the real-aperture.

The Doppler beam-sharpening is accomplished by using a narrow bandwidth filter that tracks the Doppler-shifted frequency from the target. The limits on the ground defined by the filter are shown by the hatched region of width r_a. Its bandwidth is indicated as B_{Df}.

The Doppler frequency shift obtained by the beam passing by the target (see parts (b) - (f) of Fig. 2.3) is shown in part (g) of the figure. The Fig. 2.3(g) shows the limits of the tracking filter passband following the Doppler shift associated with the point target. The Doppler frequency from the other parts of the beam are discriminated against because the Doppler frequencies associated with them cannot pass through the tracking filter. The bandwidth of the filter controls the along track resolution possible. From (2.24) the possible along track resolution is

$$r_a = \frac{\lambda R}{2 u} B_{Df} \qquad (2.25)$$

2.4 SAR RESOLUTION IN RAIN

SAR can use the full synthetic-aperture only when the targets in the pulse volume are correlated, i.e., their phase positions remain essentially fixed. This is because the coherent phase compensation corrects for specific phase shifts from a point, only returns from that point are constructively added. To find the maximum

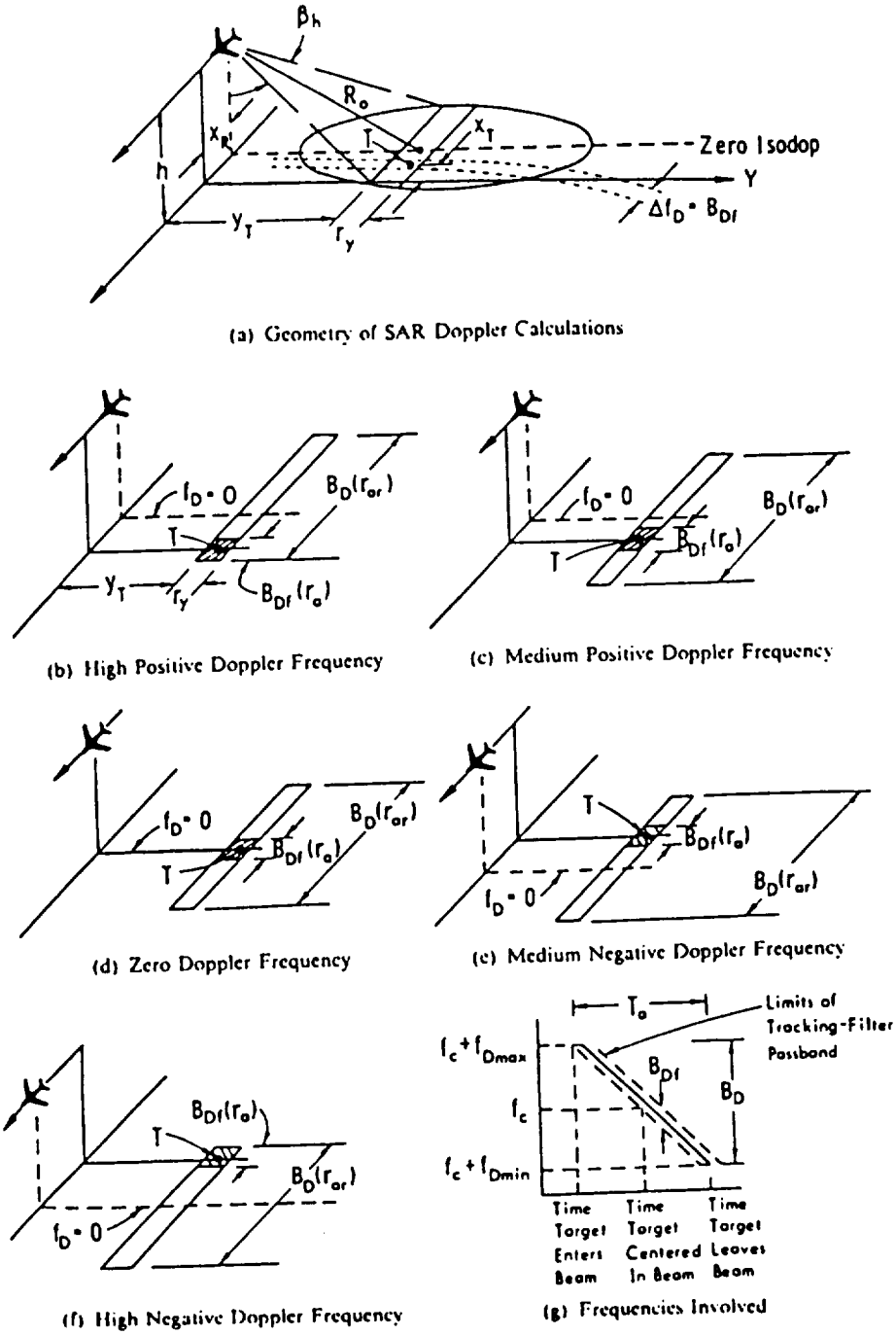

Fig. 2.3 Doppler beam sharpening SAR. Concept assumes a narrow-band Doppler filter. (Ulaby et al., 1982)

possible aperture that can be synthesized during T_a, the time during which the target is illuminated, let us consider the bandwidth between the isodops for a SAR.

$$B_{df} = \left(\frac{2\ U\ r_{as}}{R\ \lambda} \right) \qquad \textbf{(2.26)}$$

where U is the velocity of the platform, R is the range and the others have their usual meaning. The ratio between the synthetic-aperture length L_s and the time T_a to pass that length is simply the platform speed. Thus the maximum possible aperture that can be synthesized during the integration time T_a is

$$L_s = U\ T_a \qquad \textbf{(2.27)}$$

A larger Doppler spread (σ_{vs}) leads to shorter integration time. For a smaller synthetic-aperture where the resolution element is large, Atlas and Moore (1987) show that the Doppler bandwidth is

$$B_{df}(precip) = 4\ \frac{\sigma_{vs}}{\lambda} \qquad \textbf{(2.28)}$$

From (2.28) we may write

$$r_{as} = 2\ \sigma_{vs}\ \frac{R}{U} \qquad \textbf{(2.29)}$$

and also

$$L_s = \lambda \frac{U}{4\,\sigma_{vs}} \qquad (2.30)$$

and the synthetic-beamwidth is

$$\beta_s = 2 \frac{\sigma_{vs}}{R} \qquad (2.31)$$

All this means that the synthetic-beamwidth varies and is broadened in proportion to the Doppler spectral width of the target. Further, it means that the number of pulses that can be coherently integrated and the effective length of the synthetic-aperture L_s are inversely proportional to σ_{vs}.

This applies only when

$$\sigma_{vs} < \frac{\lambda\, U}{6\, L_n} \qquad (2.32)$$

where

U = the velocity of the spacecraft in m/s,

L_n = length of the along-track real aperture,

σ_{vs} = standard deviation of the Doppler velocity spectrum,

For X-SAR the standard deviation of the Doppler velocity (due to the wind turbulence, shear, etc.) must be less than 3.75 m/s for a three-fold improvement in the resolution for the SAR, compared to the RAR (i.e., for the synthetic-beamwidth to be one-third of the real beamwidth).

This indicates that the effective beamwidth increases with increases in σ_{vs}, the

spread of the target Doppler spectrum. Further, the integration gain decreases with σ_{vs} because the number of pulses that can be coherently integrated along track is proportional to the target coherency time and thus inversely proportional to σ_{vs}. Therefore, the echo power is independent of the resolution. The echo power is identical to the conventional radar with an along-track beamwidth equal to the real beam used in the SAR. The SNR equation for the SAR looking at the rain will be the same as that for the real-aperture radar except when the SAR prf exceeds that required for Nyquist sampling of the Doppler spread. (Atlas and Moore, 1987)

CHAPTER III
MODELS USED IN THE CALCULATIONS

3.1 INTRODUCTION

To determine the signal-to-noise ratio (SNR) of the signal returned from rain, the scattering coefficient of the rain must be known. Though theoretically it is possible to model the rain as discrete scatterers (apply Mie scattering theory with Rayleigh approximation), it is not possible to describe all the different rain types by a single equation. This is in part due to the drop distribution of the volume scatterers. Here, in this study, for the SNR and SCR calculations to be of any use rain rate must be the principal variable. It is easier to use empirical relationship developed by meteorologists for these calculations. These empirical relationships can be linked to the Rayleigh approximations by use of model dropsize distributions.

The SCR calculations require knowledge of the surface scattering coefficient in addition to the scattering coefficient due to rain. The rain-measurement experiment is to be primarily over ocean and forest. Although various mechanisms can be used to describe the ocean backscatter, here we must select an ocean-surface echo model that shows variations with wind speed, angle of incidence and aspect angle (direction of wind with respect to the radar boresight).

Tropical forest clutter at vertical is unrelated to wind, and varies little with time of day or season. The actual measured scattering coefficient over the Amazon at Ku band rather than a model, will be used in the SCR calculations (Ulaby, et.al, 1986) (Schroder et al., 1985).

3.2 BACKSCATTER FROM THE OCEAN

Radar measurements of backscatter from the ocean were first made under controlled conditions during World War II. At that time, and for many years thereafter, the measurements were made to increase knowledge about the nature of the sea clutter that obscures radar echoes from surface targets and submarine periscopes. The NASA earth-resource program in 1964 gave impetus to the radar observation of the sea for research. This was followed by a series of airborne experiments leading to the use of radar scatterometer to measure windspeeds and culminated in the Skylab S-193 and Seasat space-based scatterometer experiments.

Radar backscatter from the ocean at most angles of incidence is strongly related to the speed and direction of the wind. When the wind starts to blow over the calm ocean, the first waves formed are due to frictional drag. As these short waves build up, non-linear interactions transfer energy to waves with larger amplitudes and longer wavelengths. This interaction and transfer continues until the equilibrium is reached. For angles of incidence above 20° the predominant radar scattering mechanism is Bragg scattering, while at near-vertical incidence angles the mechanism is a quasi-specular one in which geometric or physical optic techniques can be used. The amplitude of the radar signal beyond 20° is dominated by the Bragg-resonant ripples and the local angle of incidence.

The variation of the scattering coefficient (σ°) with wind speed for a particular radar look direction is reasonably well described by

$$\sigma^{o} = A\ U^{\gamma} \qquad (3.1)$$

where U is windspeed in meters per second and A and γ depends on the polarization, angle of incidence (θ), look direction, and frequency. Expressing (σ^{o}) in dB, (3.1) can be written as

$$\sigma^{o}(dB) = 10 \log \sigma^{o} = 10 \log A + 10\gamma \log (U) \qquad (3.2)$$

An orthogonal regression procedure is used to fit a straight line relation between (σ^{o}) and log (u). Values for the exponent γ are obtained for different radar and ocean parameters.

3.21 SURFACE ECHO MODEL

To obtain the surface-echo model we decided to use data from the wind-vector measurements. The use of the radar scatterometer to determine the surface wind vector over the ocean is a proven technique. The Skylab S-193 Radscat instrument allowed measurements over much of the world ocean surface, but there were very few concurrent surface observations. The measurements were compared with an underflight by the AAFE Radscat instrument, and the values of the σ^{o} observed by the two instruments were within 0.5 dB of each other. This indicated that the calibration of the two instruments were very close and were accurate in the absolute sense because they were calibrated independently. Fig. 3.1 and Fig. 3.2 are data from this experiment.

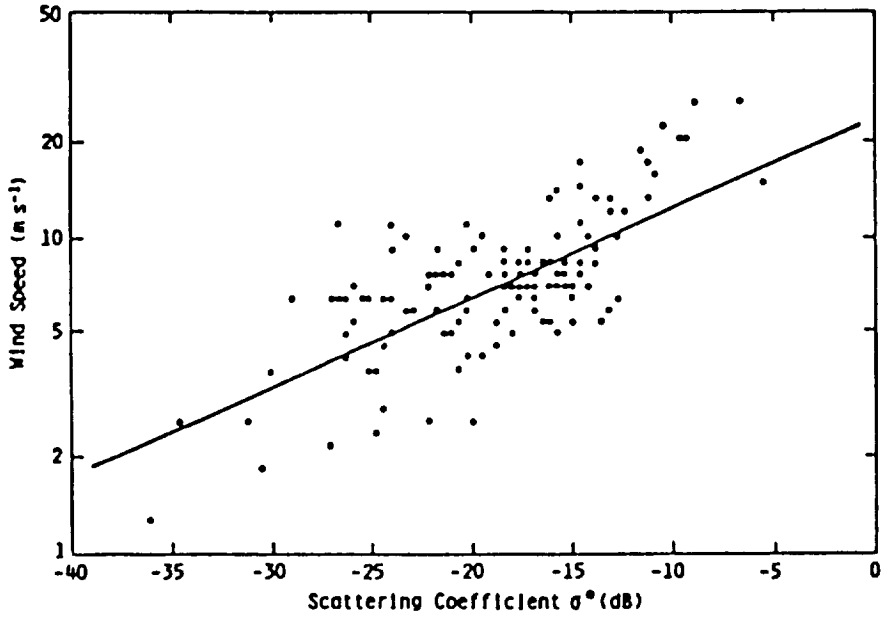

Fig. 3.1 Regression fit for Skylab σ^{o} measurements at 50° angles of incidence. (Moore and Young, 1977)

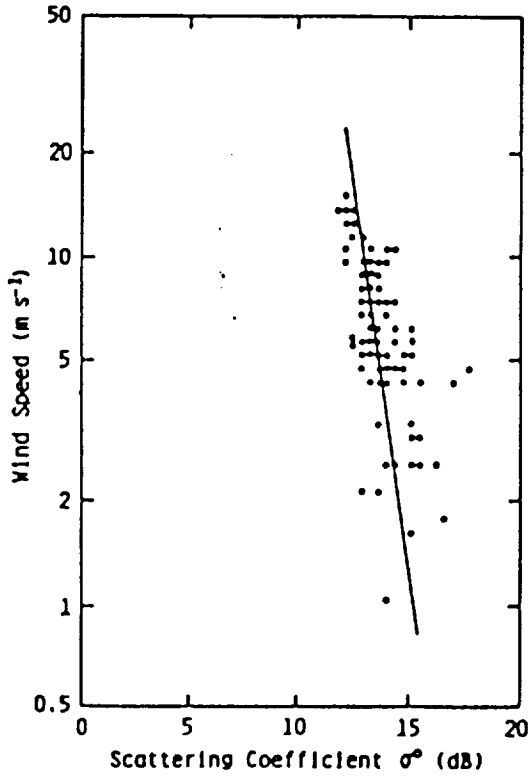

Fig. 3.2 Regression fit for Skylab σ^{o} measurements at near vertical incidence. Note the difference in response near vertical and away from vertical shown in Fig. 3.1.

The AAFE Radscat was the best calibrated airborne instrument used prior to 1980 in measurement of radar sea returns. Experiments with this instrument were aimed at improving the knowledge of the wind speed and directional response. The data were analyzed by both the NASA Langley Research Center group and workers at The University of Kansas and the City University of New York.

The circle-flight experiment, developed by Jones et al. (1978) at NASA Langley Research Center, allowed the accurate measurement of azimuth variation of echoes from the sea for the first time. An example of such measurement is shown in Fig. 3.3. Previous measurements were only for up, down, and cross winds. A basic model function for azimuth variation was developed from the Jones measurement:

$$\sigma^{o} = A + B\ \cos\phi + C\ \cos 2\phi \qquad (3.3)$$

A comparison with theoretical results of Chan and Fung (1977) is given in Fig. 3.4. Theory and experiment correspond, allowing for the variation in measurements. Because of the excellent calibration of the AAFE Radscat, and because there were many flights accompanied by high quality surface observations, this was one of the most reliable aircraft wind-response data sets available until recently.

Soofi (1978) developed an empirical model to calculate the magnitude of the ocean returns. This model matches closely with the AAFE Radscat, SEASAT and SKYLAB data (Schroeder, et al., 1985). It also accounts for various wind speeds and aspect angles (direction of the wind with respect to the radar boresight).

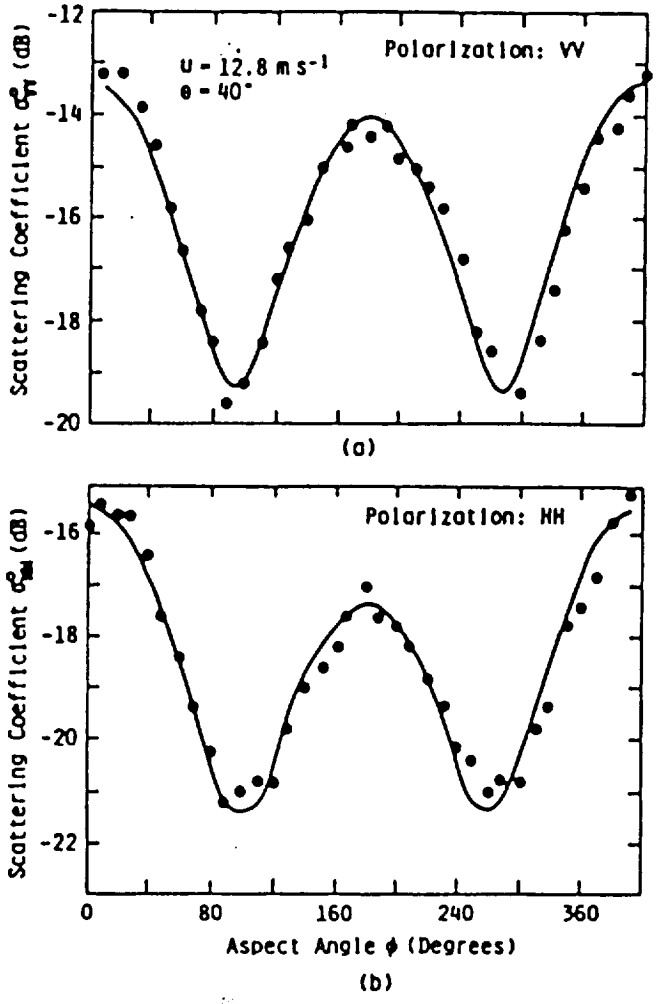

Fig. 3.3 Example of the circle-flight observation of the azimuthal variation of σ^o at 13.9 GHz, along with the regression fit (Moore, et al., 1978)

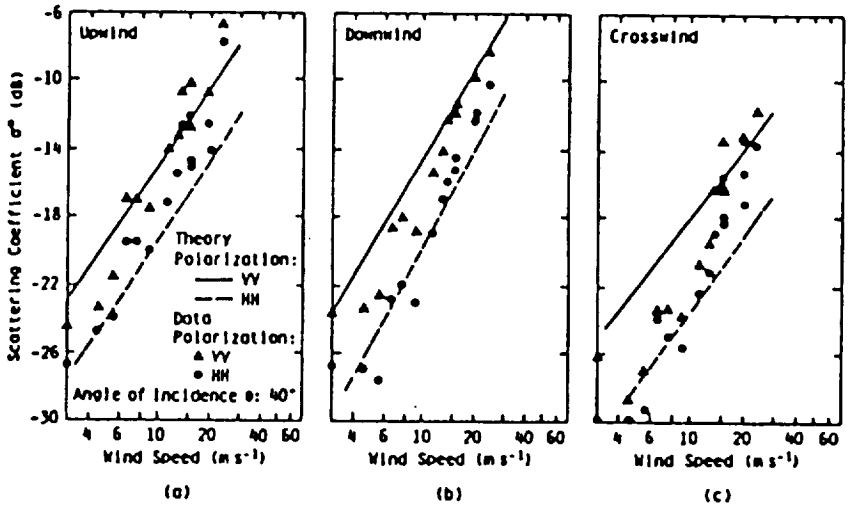

Fig. 3.4 Comparison of AAFE Radscat 13.9 GHz σ^{o} measurement with theory of Chan and Fung (1977)(Moore, et al., 1978)

The equation for this ocean-clutter model is

$$\sigma^{o}_{db}(f,\theta,W,\phi) = A + B\cos\phi + C\cos 2\phi \qquad (3.4)$$

where the coefficients A, B and C take values depending on the polarization used. For the polarization of interest (VV) the values of A, B and C are functions of wind speed, angle of incidence and frequency.

$$A = (-24.642 + 10.8256\ \log W) + (-0.1983 - 0.0017\ \log W)\,\theta$$

$$+ (1.1725 - 0.6191\ \log W)\,f + (-0.0123 + 0.0124 \log W)\,f\,\theta$$

$$B = (0.4337 - 0.7041\ \log W) + (-0.0085 + 0.0143\ \log W)\,\theta$$

$$+ (-0.0082 + 0.0153\ \log W)\,f + (0.0004 - 0.006\ \log W)\,f\theta$$

$$C = (0.1619 + 1.4160\ \log W) + (-0.0086 + 0.0089\ \log W)\,\theta$$

$$+ (0.0067 - 0.0124\ \log 2)\,f$$

Here the frequency is in GHz, the wind speed in m/s and the angle in degrees. This model predicts the value of the coefficients within about 2 dB. The maximum error occurs at 4 GHz.

Schroeder, et.al (1982) proposed the SASS (SEASAT-A Satellite Scatterometer) model based on data at 13.9 GHz. This is an empirical function giving

the relationship between the ocean normalized radar cross section and the wind vector at a height of 19.5 meters above the surface. The relationship is defined in the form of a table (Table 3.1(a)) which gives the two coefficients G and H in the equation

$$NCRS(dB) = 10[G(\theta,\phi) + H(\theta,\phi)\ \log_{10} U] \qquad \textbf{(3.5a)}$$

where θ is the radar incidence angle, ϕ is the angle between the wind direction and the radar look direction, and U is the neutral stability wind speed in meters per second. The variation of the NRCS (σ^o) with the surface wind speed obtained from Soofi's and the SASS model are compared in Fig. 3.5. Though the model proposed by Soofi is good for preliminary calculations, it was never in the form of published results. The models are close for upwind direction and downwind direction, but the crosswind values differ.

For C-Band there were recent models available from ESA based on the ERS-1 experiment. ESA's CMOD4 (Ad Stoffelen, et al., 1992) gives the model as a complex transfer function. The transfer function is given by

$$\sigma_0 = K_b\ [1+k_1\ \cos(\phi)+k_3\ \tanh(k_2)\ \cos(2\phi)]^{1.6}\ 10^{(\alpha+\gamma\ \Psi(v+\beta))}$$

where α, β, γ are coefficients in Table 3.1(b) (Ad Stoffelen, et al.,1992) and Legendre polynomials of the first and second order and ϕ is the direction with respect to the beam. k_1, k_2, k_3 are functions of the coefficients and the wind velocity v. The Legendre polynomials have θ, the angle of incidence as their variable.

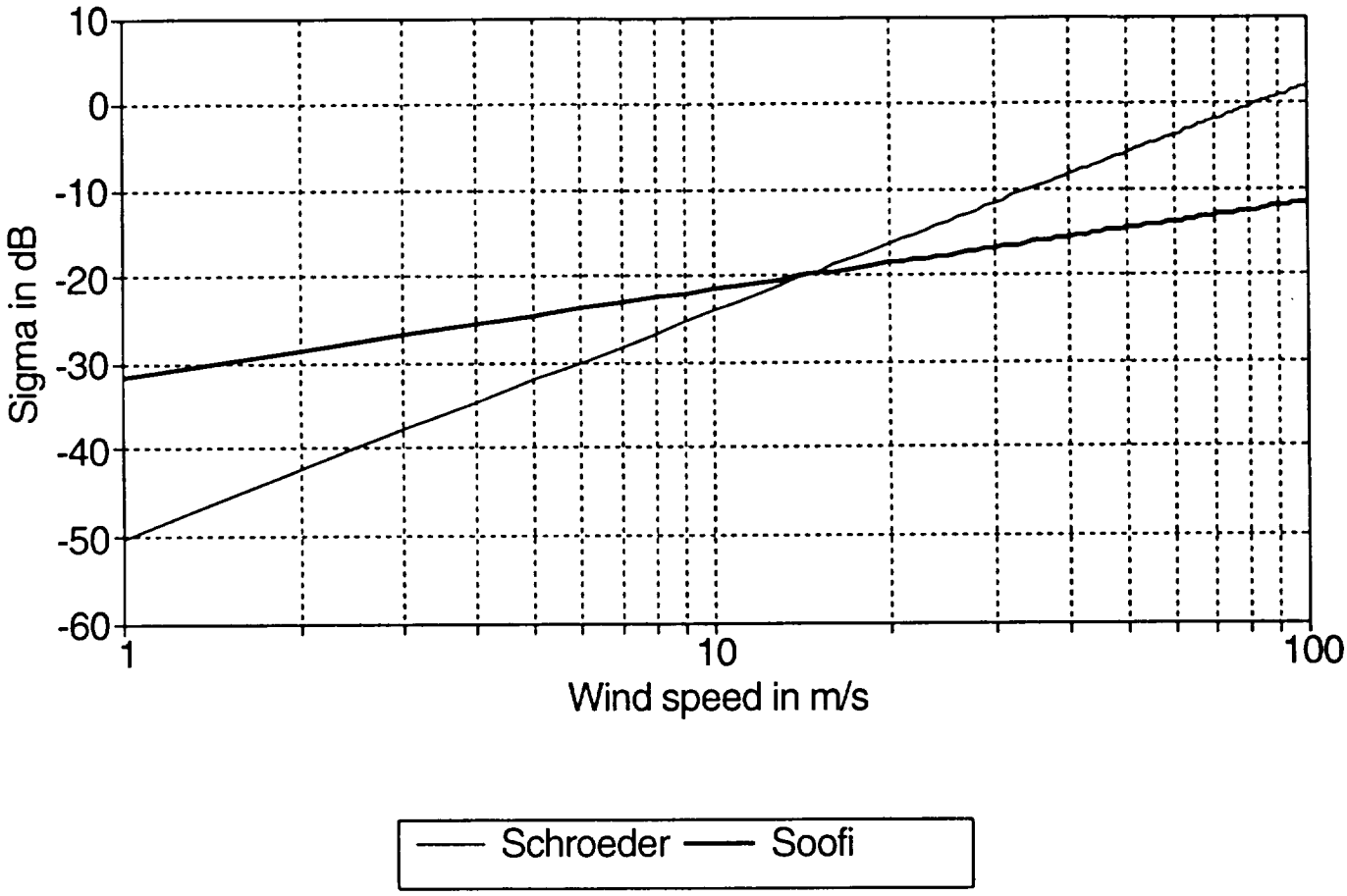

Fig. 3.5 Comparison of the scattering coefficient (σ) of the ocean surface obtained from the SASS (Schroeder) and Soofi's model at 9.7 GHz, 60°, cross wind.

Preliminary calculations of the backscatter at C-band based on the CMOD4 model show an unusually high γ. Soofi's model of backscattering from the ocean is inconsistent with this. However, Soofi's C-band model is based on interpolation rather than actual experiment. Further, CMOD4 is in the form of published results, based on the ERS-1 experiment. Hence the CMOD4 model is preferred over Soofi's C-Band model; a comparison between the two is shown in Fig. 3.6.

3.22 EFFECT OF RAIN ON SURFACE RETURN

The modification of the backscatter due to impinging rain drops may be important. In the area of the ocean where it is raining, the cross section increases due to the impinging rain drops. Moore, et al. (1979) showed that, for a given wind speed, the backscatter cross section depends on the rain rate, as shown in Fig. 3.7. Hansen (1986) later conducted both laboratory and field experiments that show a significant enhancement of the echo intensity as a result of the splashes and ripples due to the impinging raindrops. This enhancement of the radar return applies only for low wind speeds. At high wind speeds the effect of rain rate on backscatter modification is lost; i.e., the backscatter at these high wind speeds is independent of the rain rate (Moore, et al., 1979; Blivens and Norcross, 1988) as seen in Fig. 3.7.

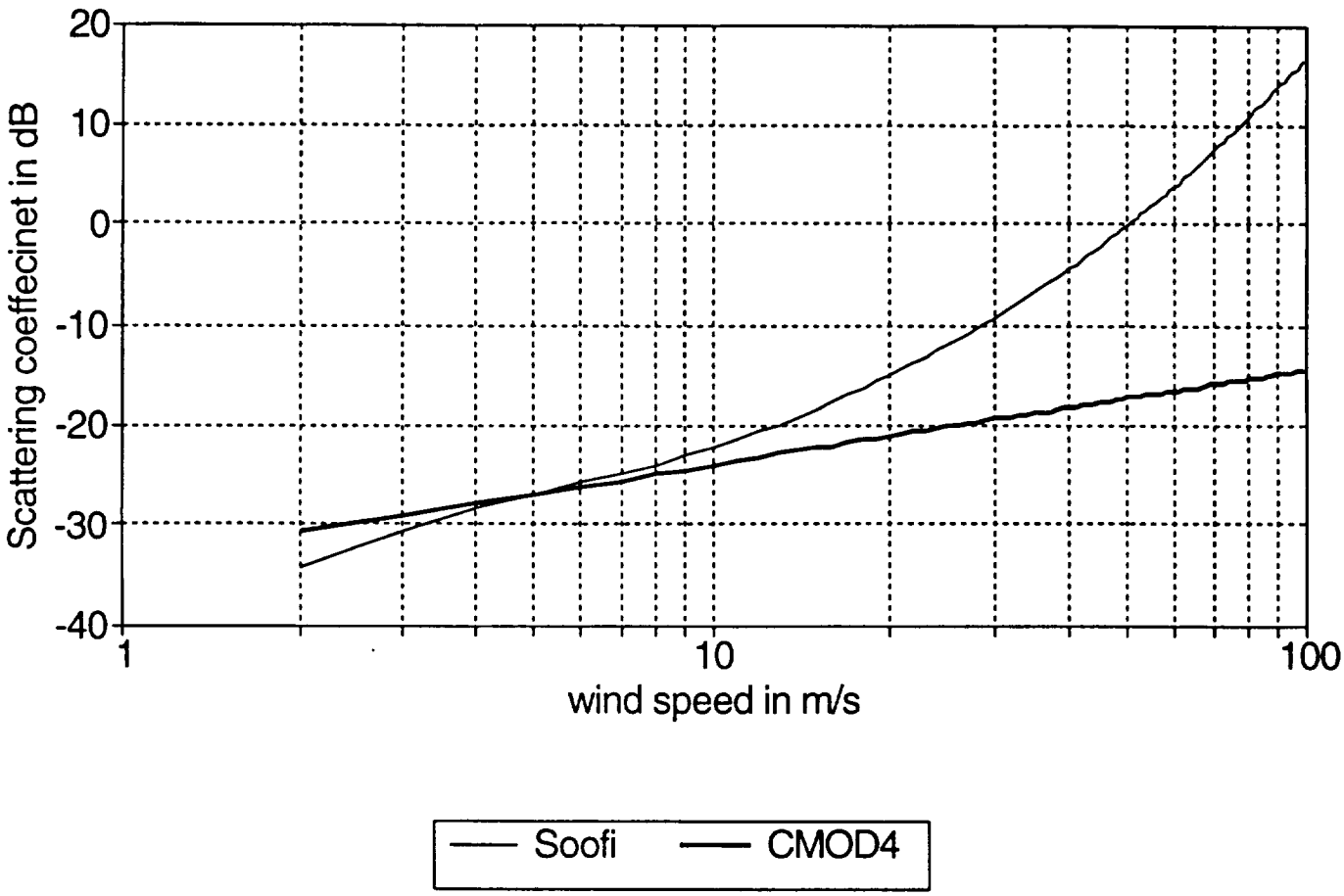

Fig 3.6 Comparison of the scattering coefficient (σ) of the ocean surface obtained from the CMOD4 and Soofi's models at 9.7 GHz, 60°, Cross wind.

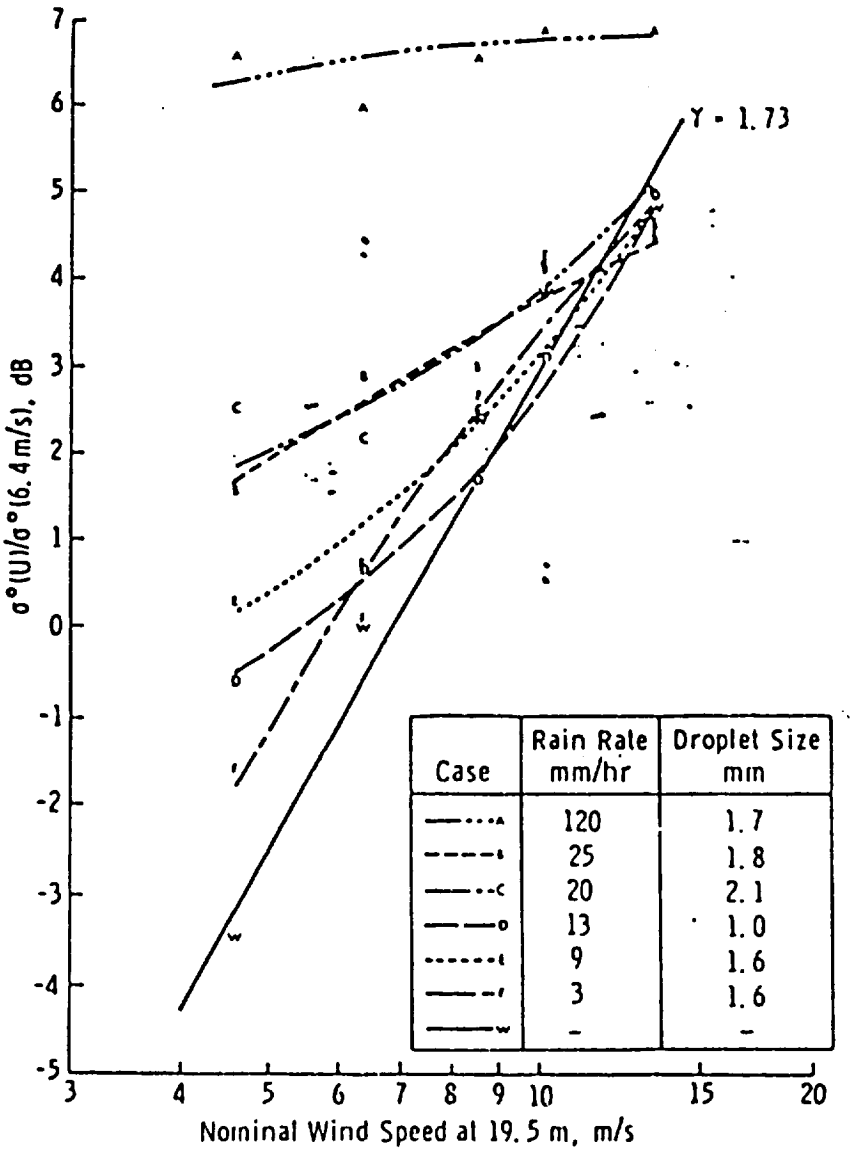

Fig. 3.7 Experimental results indicating the loss of backscatter modification of the ocean surface due to impinging rain drops, at higher surface wind speeds.(Moore et al., 1979)

3.3 BACKSCATTER FROM THE RAIN

Mie first devised a general theory that describes the scattering of a plane wave by a sphere. Mie theory shows the backscattering cross section of a spherical drop (Battan,1973):

$$\sigma_b = \frac{\pi a^2}{\chi^2} \left| \sum_{m=1}^{\infty} (-1)^m (2m+1) (a_m - b_m) \right|^2 \quad (3.6)$$

where a is the drop radius and ϕ equals $2\pi a/\lambda$. The coefficient a_m and b_m are in terms of spherical Bessel functions and Hankel functions of the second kind, with arguments χ and n_c, the complex refraction;

$$n_c = n - i\kappa \quad (3.7)$$

where n is the ordinary refractive index and κ is the absorption coefficient of the material involved. For spheres that satisfy the Rayleigh condition ($\chi << 1$), the backscattering cross section of a single particle is proportional λ^{-4}. That is, (Battan, 1973)

$$\sigma_b = \frac{\pi^5}{\lambda^4} |K|^2 D^6 \quad (3.8)$$

where K is related to the complex permittivity n_c and is approximately 0.92 when the scatterer is liquid water, over the wavelength band most commonly used in meteorology (Table 3.2). Summing over N_v particles per unit volume, the rain

volume backscattering coefficient σ_v is expressed as

$$\sigma_v = \sum_{i=1}^{N_v} \sigma_b(D_i)$$

$$= \frac{\pi^5}{\lambda^4} |K|^2 \sum_{i=1}^{N_v} D^6 \qquad (3.9)$$

We can write $\Sigma_i D^6 = Z$, the reflectivity, which is usually given in mm^6/m^3.

Radar meteorologists have derived an empirical power law, the Z-R relationship, from the available data. That is,

$$Z = a_1 R_r^{b_1} \qquad (3.10)$$

where a_1 and b_1 have been found to depend on the dropsize distribution, rain type, rain rate, frequency, and region. The coefficients differ markedly at small and large values of R_r. However, with the exception of orographic rains, most differ only slightly at rainfall intensities between 20 and 200 mm/hr. Although it is clear that the Z-R relation is useful, the values of the coefficients a_1 and b_1 have to be selected judiciously. A single Z-R relation for all types of rain cannot account for the variations for different types of rain (Table 3.3) Battan (1973) calculated the Z-R relation using the Mie scattering theory. Table 3.4 shows the various relationships for different wavelengths and dropsize distributions. Clearly for a given wavelength, but for different rain rates, a_1 takes drastically changing values (Table 3.4). However, for

modest and small rain rates, assuming the value of a_1 to be around 300 and b_1 to be about 1.5 is reasonable. Here we use the relation

$$Z = 300 \; R_r^{1.5} \tag{3.11}$$

to describe the rain reflectivity. The scattering coefficient of the rain is described by

$$\sigma_v = \frac{\pi^5 \; 300 \; R_r^{1.5}}{\lambda^4} \; |k|^2 \tag{3.12}$$

when λ is in centimeters and rain rate R in mm/hr.

3.31 ATTENUATION IN THE RAIN VOLUME

The attenuation experienced by the radar returns from the rain may be attributed to two effects: 1. Absorption, and 2. Scattering of the power away from the radar beam (Ulaby, et.al, 1981). This is because, in the cloud or rain volume, the scatterers are usually assumed to be randomly distributed within the volume. Thus, there are no coherent phase relationships between the fields scattered by the individual particles.

Mie scattering theory leads to two cross sections; the total scattering cross-section Q_s and the absorbing cross-section Q_a. The extinction cross-section Q_t is the sum of Q_s and Q_a. The extinction cross-section is the area which, when multiplied by the incident intensity, gives the total power removed from the plane wave by the

particle. The absorption cross section is the area which, when multiplied by the incident intensity, gives the power dissipated as internal heat in the particle. Atmospheric gases, cloud droplets, and Rayleigh raindrops act as absorbers, but both scattering and absorption are notable for non-Rayleigh (large) raindrops.

Assuming that the Rayleigh condition is valid (i.e.,$\chi << 1$), the Mie scattering and absorption cross sections reduce to the corresponding Rayleigh scattering and absorption cross sections. That is (Ulaby, et.al, 1981)

$$k_s = \int_{r_1}^{r_2} p(r) Q_s(r)\ dr \qquad (3.13)$$

where k_s is the volume scattering or absorption coefficient, p(r) is the dropsize distribution, Q(r) is the scattering or absorption cross-section of the sphere of radius r in m^2, r_1 and r_2 are the upper and lower limits of drop radii contained in the cloud. Expressing (3.13) in terms of scattering efficiency $\xi_s = Q_s/\pi r^2$ and the dimensionless parameter $\chi = 2\pi r/\lambda$ the scattering coefficient gives

$$k_s = \frac{\lambda^3}{8\pi^3}\int_{\chi_1}^{\chi_2} \chi^2\ p(\chi)\ \xi_s(\chi)\ d\chi \qquad (3.14)$$

where the limits on the integral cover the entire range of possible values of χ. Expressing (3.13) in terms of absorption efficiency $\xi_a = Q_a/\pi r^2$ and the dimensionless parameter χ, the absorption coefficient is

$$k_a = \frac{\lambda^3}{8\pi^3} \int_{\chi_1}^{\chi_2} \chi^2 \; p(\chi) \; \xi_a(\chi) \; d\chi \qquad (3.15)$$

For a given dropsize distribution the volume extinction coefficient for k_{er} (= $k_s + k_a$) is

$$k_{er} = \frac{\lambda^3}{8\pi^3} \int_{\chi_1}^{\chi_2} \chi^2 \; p(\chi) \; \xi_{er}(\chi) \; d\chi \qquad (3.16)$$

Here, as previously defined, $\chi = 2\pi r/\lambda$ and $\xi_{er}(\chi)$ is the Mie extinction coefficient for rain given by

$$\xi_{er}(n, \chi) = \frac{2}{\chi^2} \sum_{m=1}^{\infty} (2m+1) \; Re[a_m + b_m] \qquad (3.17)$$

Here Re signifies the real part of a_m and b_m, the Mie coefficients (Ulaby, et.al, 1981, pp 291).

From the practical point of view it is desirable to relate the extinction coefficient for rain k_{er} directly to the rain rate R_r. The relationship commonly used in literature (Gunn and East, 1954) is of the form

$$k_{er} = \kappa_1 \; R_r^b \qquad (3.18)$$

where κ_1 is in dB km^{-1} per mm hr^{-1}, R_r is the precipitation rate in mm hr^{-1} and b is a dimensionless parameter. The coefficients κ_1 and b, which are functions of the

wavelength λ, are determined by fitting (3.18) to computed values of k_{er} for the known dropsize distributions. The dropsize distributions in turn determine the precipitation rate R_r through the relation

$$R_r = 6\pi \ 10^{-4} \sum_{i=1}^{N_v} v_i \ d_i^3 \qquad (3.19)$$

where $v_i(ms^{-1})$ is the terminal velocity and $d_i(mm)$ the diameter of the i^{th} rain drop and $N_v(m^{-3})$ is the total numbers of drops per unit volume. Table 3.5 (Ulaby, et.al, 1981) provides list of values for κ_l and b at each of the several microwave frequencies.

3.4 RADAR EQUATION FOR METEOROLOGY

The basic radar equation for any target is

$$P_r = \frac{P_t \ G^2 \ \lambda^2 \ \sigma}{(4\pi)^3 \ R^4} \qquad (3.20)$$

where the variables have their usual meaning.

If $\Sigma \ \sigma_i$ is the average total backscatter cross section of particles per unit volume (m^3), the radar cross section may be expressed as

$$\sigma = V_m \ \Sigma \sigma_i \qquad (3.21)$$

where V_m is the volume of the resolution cell. We can use the Rayleigh approximation when the dropsize is $<< \lambda$ to write.

$$\Sigma_i \sigma_i = \frac{\pi^5 \Sigma D^6}{\lambda^4} |K|^2 \qquad (3.22)$$

where is λ in centimeters and K is a factor involving the complex permittivity. Using (3.12) we may write the radar equation as

$$P_r = \frac{P_t G^2 \pi^2 V_m}{64 \lambda^2 R^4} 300 Z^{1.5} |K|^2 \qquad (3.23)$$

This radar equation does not include the various system losses, nor does it account for attenuation due to clouds, rain, the ice melting layer and the atmosphere. Additional factors added to (3.23) can account for this.

$$P_r = \frac{P_t G^2 \lambda^2 V_m \eta L_s L_b^2}{(4\pi)^3 R^4} 10^{-0.1 K_{er}} \qquad (3.24)$$

is the final form of the radar equation for meteorology obtained by substituting additional factors to account for losses.

where

$$\eta = \frac{\pi^5 300 R^{1.5} |K|^2}{\lambda^4} 10^{-10} \qquad (3.25)$$

G is the gain, B is the bandwidth, L_s is the system loss, L_b is the signal loss due to absorption by the ice melting layer, η is the rain reflectivity, K_{er} (3.18) is the attenuation due to rain. The other parameters have their usual meaning.

Dividing (3.24) with the noise power we can calculate the SNR. The volume

of the rain resolution depends upon the angle of incidence. These volume calculations, based on the geometry at different angles of incidence, are given in the next two chapters.

CHAPTER IV
CALCULATIONS AT OFF-VERTICAL ANGLES

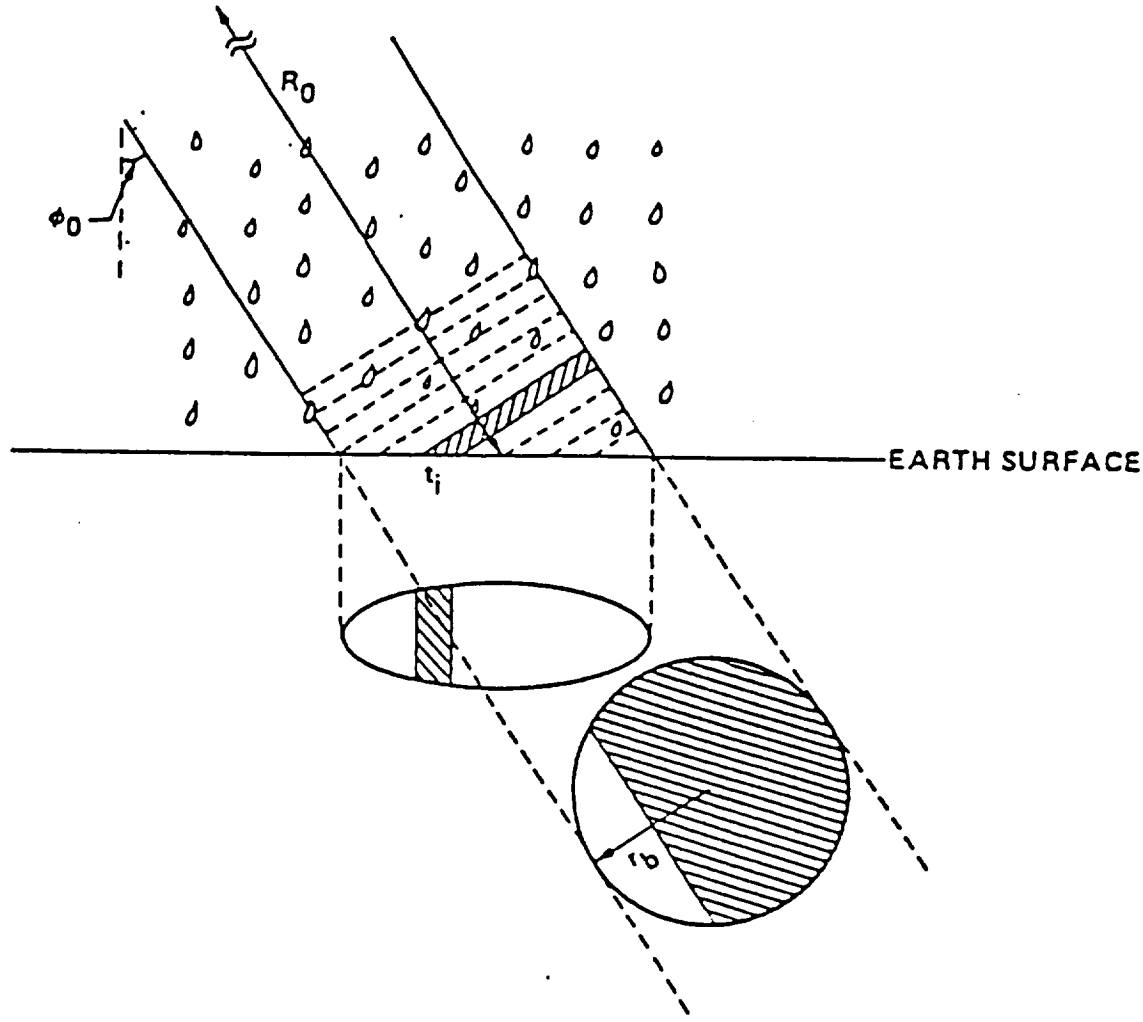

Fig. 4.1(a) Off-Vertical look geometry illustrating that the surface returns arrive simultaneously with the rain echo.

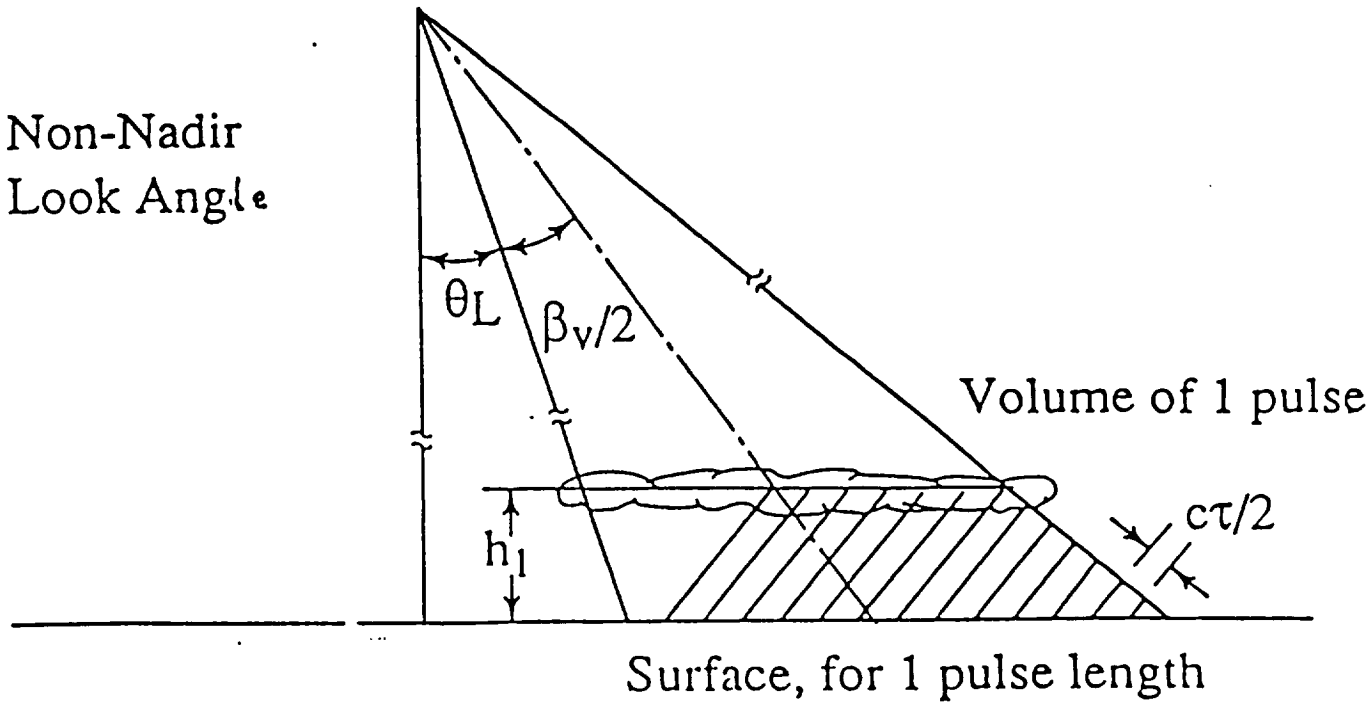

Fig. 4.1(b) Off-vertical look geometry for the plane earth case used to calculate the pulse volume.

4.1 INTRODUCTION

For vertical incidence and a narrow transmitted pulse, the backscattered power from the hydrometeors arrives at the receiver prior to the large surface contribution. At non-vertical viewing angles, however, the surface return arrives simultaneously with the desired echo (see Fig. 4.1(a)). Thus, the surface clutter can mask the returns due to the rain at the surface. To calculate the SNR and the clutter coupled to the resolution element, the volume of the scattering element and the corresponding surface area coupled to it must be calculated. For the SAR the volume encompassed by the radar beam is similar to that of a real aperture radar. Thus each resolution element in the radar beam will be similar to that of the real aperture radar.

When the radar is pointing off-vertical, some of the resolution elements in the rain volume have different characteristics. This is in part because of the finite height of the rain volume. It is possible to identify different resolution cells in the rain volume based on whether they are completely or partially rain filled.

4.2 GEOMETRY

The geometry shown in Fig. 4.1(b) is for non-vertical viewing angles making the plane-earth assumption. Here, for simplicity in approximate calculations, we assume a sharp beam edge and neglect the sides of the mainlobe and sidelobes. More exact calculations would require accounting for true beam shape, but these simplifying assumptions enable us to define range cells that are sharply beam limited. Thus we

may divide the beam into three well defined regions and allows computation of the dimensions of the observed volume as a function of the look angle. This assumption may not hold true in reality but SCR calculations are made on cells that are close to ideal. The beam below the cloud top is divided into range cells corresponding to a slant-range resolution of 15 m. The swath R_s on the ground for vertical beamwidth β_v and satellite height h is

$$R_s = h\,[\,\tan(\theta_1) - \tan(\theta)\,] \qquad (4.1)$$

where

$$\theta_1 = \beta_v + \theta \qquad (4.2)$$

and

$$R_{s1} = (h - h_1)\,[\tan(\theta_1) - \tan(\theta)\,] \qquad (4.3)$$

is the swath width at the cloud top, and h_1 is the thickness of the rain. Computation of the swath gives us an idea of the coverage possible by the X-SAR mission.

The number of rain-filled cells is

$$n = \frac{R_{1max}}{r_R} \qquad (4.4)$$

where

$$R_{1max} = \frac{h_1}{\cos(\theta_1)} \qquad (4.5)$$

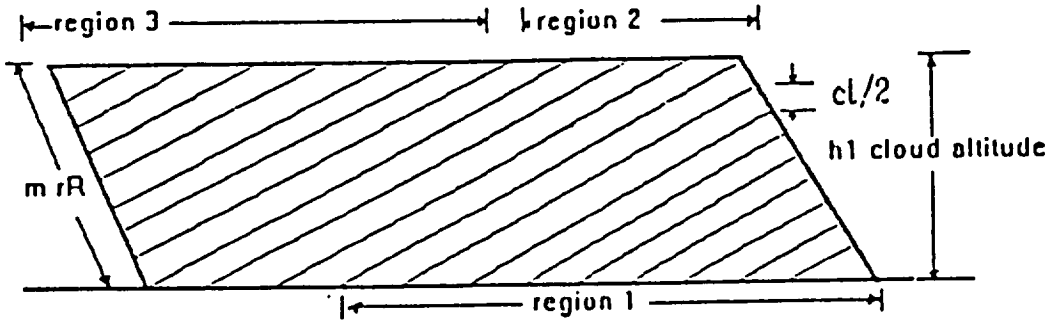

off nadir geometry illustrating the three regions of intrest

Fig. 4.2 Geometry at off-vertical look angles, with completely rain filled volume, identifying three regions.

is the range in the rain-filled volume and r_R is the range resolution. Fig. 4.2 shows three cases of cell lengths.

Region 1. Pulse position at the end of the return that extends up to the edge of the beam, not to the rain top.

Region 2. Pulse position in the center of the return that extends from the ground to the rain top.

Region 3. Pulse position at the start of the return that extend from the inner edge of the beam to the cloud top and includes no ground return.

If we assume that the rain extends throughout the swath, most of the returns correspond to those in region 2. Further, since we can calculate the signal-to-noise ratio and the signal-to-clutter ratio using the real-aperture parameters, the width of a cell in the direction normal to the plane of the paper, for power calculations is

$$r_{an} = \beta_a \, [R - n r_R] \qquad (4.6)$$

where β_a is the azimuth beamwidth, R is the slant range to the ground, r_R is the range resolution and n is the cell number, measured from maximum R backward.

4.21 CELL VOLUME CALCULATIONS

In region 1 (longest range) the volume of the n^{th} cell from the bottom is

$$V_n = L \, r_R \, r_a \qquad (4.7)$$

where

$$L = n\, r_R \cot(\theta_1) \qquad (4.8)$$

is the length of the rain cell in the plane of incidence and normal to the ray from the radar to the rain. The width of the rain cell in the direction normal to the plane of the paper is r_a, r_R is the slant-range resolution and θ_{av} is the average angle of incidence.

In region 2 (center of the beam) the volume is the same for all pulses.

$$V_n = r_a\, r_R \frac{h_1}{\sin(\theta_{av})} \qquad (4.9)$$

Here θ_{av}, the average angle of incidence, is used when calculating the range to the pulse volume (bounded by concentric spheres) to avoid the complication arising because it varies slightly across the beam. The ground area coupled to the rain cell in the above two cases is

$$A = r_R \left(\frac{r_a}{\sin(\theta_r)} \right) \qquad (4.10)$$

where θ_r is θ_1 in region 1 and θ_{av} in region 2.

In region 3 (shortest range) there is no ground return. The length of the cell is

$$L = m\, R_r \cot(\theta) \qquad (4.11)$$

where m is the index starting from the top. The cells in region 3 are valid only for the assumed beam and minimal antenna sidelobes.

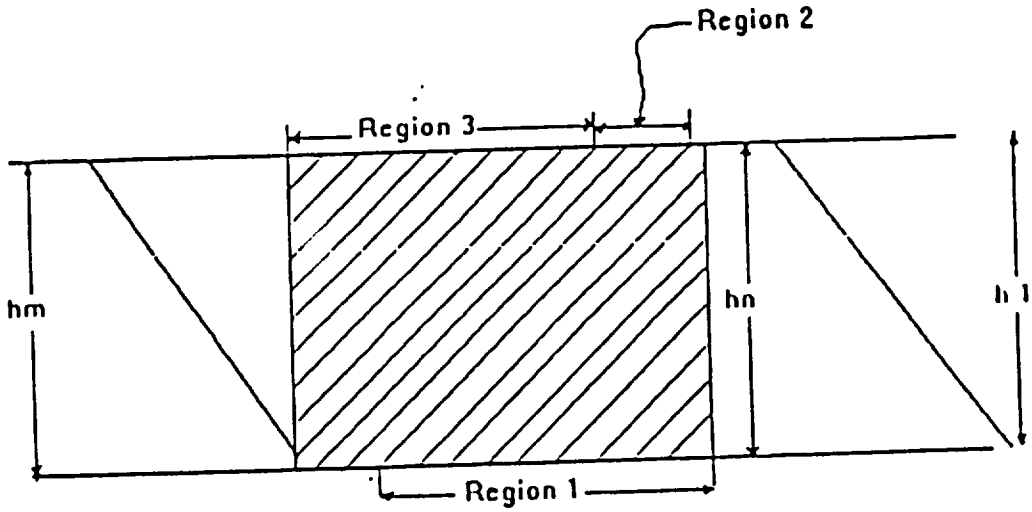

Fig. 4.3 Geometry at off-vertical look angles illustrating that even with partially rain filled volume, there are three regions identified.

Even if the rain cell fails to fill the swath completely three similar regions may be identified, but the number of constant volume rain cells is less, as seen from Fig. 4.3.

Region 1 The region for which returns come from the far edge of the rain cell.

Region 2 The region for which returns come from near the center of the cell.

Region 3 The region for which returns come from near the edge of the cell.

The volume of the rain cells at the center is the same as that in region 2 of the completely filled beam. However, for region 1, if

$$h_n = n\left(\frac{r_R}{\cos(\theta_{av})}\right), \tag{4.12}$$

and the length of the cell is

$$L = \frac{h_n}{\sin(\theta_{av})} \tag{4.13}$$

and the volume of the cell can be written as

$$V_n = r_R^2\, r_a \left(\frac{n}{\cos(\theta_{av})\,\sin(\theta_{av})}\right) \tag{4.14}$$

where n is an integer and h_n is defined as the distance to the pulse intersection with the outer edge of the cell.

In region 3

$$h_m = m\left(\frac{r_R}{\cos(\theta_{av})}\right) \tag{4.15}$$

where m is an integer value corresponding to the cell number (starting from the top) and h_m is the height to the intersection of the range cell with the inner edge of the rain cell. The length of the cell from this point to the top is

$$L = \frac{h_m}{\sin(\theta_{av})} \tag{4.16}$$

The volume of the rain cell in this region is

$$V_m = r_a \, r_R \left(\frac{h_m}{\sin(\theta_{av})} \right) \tag{4.17}$$

which reduces to

$$V_m = m \, r_a \left(\frac{r_R^2}{\sin(\theta_{av}) \cos(\theta_{av})} \right) \tag{4.18}$$

Thus the volume of the resolution cell in the rain is a function of the look angle and the range resolution only, since r_a is assumed to be a constant.

For plane-earth geometry, the look angle and the incidence angle are the same. However, for the spherical Earth they are not. Since the rain height is small compared to the satellite height, we can use incidence angle in the calculations (i.e., we may use all the equations discussed previously with incidence angles rather than the pointing angle).

4.3 SIGNAL-TO-CLUTTER RATIO

The backscatter method uses the returned echo from the rain to compute the rain rate. For non-vertical angles of incidence, however, the surface returns arrive simultaneously with the desired echo and increase in magnitude as the range gates within the mainbeam begin to intersect the surface (see Fig. 4.1(a)). Thus, the surface clutter can mask the return due to the rain. For the backscatter method to work, the echo from the rain should be substantially above the surface echo to allow separating them. Hence, we compute the **signal-to-clutter ratio** (SCR). This is defined as the ratio of the desired signal (rain return) to the clutter signal (surface return). Since the surface and rain are excited by the power from the same transmitter, one need not use the radar equation in its entirety for these calculations. The scattering coefficient for the rain has the units m^3 but the scattering coefficient of the ground has the units m^2. To compare the returns, one must multiply the rain returns by the volume of the rain cell and the surface returns by the area of the surface coupled to the corresponding rain cell.

The scattering coefficient for the rain from (3.22) when λ is in cm is (an additional factor 10^{-10} accounts for change in the units)

$$\sigma_v = \frac{\pi^5}{\lambda^4} Z |K|^2 10^{-10} \qquad \textbf{(4.19)}$$

The volume of the rain cell is given by

$$V = r_R \, r_a \, L \tag{4.20}$$

where r_R is the range resolution, r_a, the azimuth resolution and L is the length of the rain cell, discussed in the previous section. Since the scattering coefficient of the ground calculated from the model is in dB, we can get the total cross section by adding 10 log(ground area) to σ_{dB}, obtaining σ_{gdB} as

$$\sigma_{gdB} = \sigma^{\circ}_{dB} + 10 \log(r_a \, R_{s1}) \tag{4.21}$$

where r_a and R_{s1} are from geometry discussed in the previous section.

To determine how much the rain signal lies above the ground signal we compute

$$\Delta\sigma_{dB} = \sigma_{vl_{dB}} - \sigma_{g_{dB}} \tag{4.22}$$

where

$$\sigma_{vl_{dB}} = 10 \log(\sigma_r) \tag{4.23}$$

and

$$\sigma_r = \sigma_v \, V \tag{4.24}$$

Now let us introduce the concept of ideal rain cells. An ideal rain cell is defined as a resolution cell that has a completely rain-filled volume. Clearly these are the kind of rain cells that are of interest for our calculations. From the previous discussion it is clear that the rain cells in region 2 come close to our definition of an

ideal rain cell.

4.31 SIGNAL-TO-CLUTTER RATIO IN THE MAIN PART OF THE RAIN

Let us now consider a more realistic case, including attenuation effects. For non-vertical look angles, if the entire beam volume is assumed to be rain filled, all the returns from the ground are attenuated. Further, as we move from the top to bottom of a rain cell, the signal is attenuated increasingly as shown in Fig. 4.4. To consider this type of attenuation for each rain cell (only using Region 2), we must determine the attenuation factor for different path lengths. Thus the actual surface echo is

$$\sigma_s = \sigma_o \, e^{-\alpha \, 2 \, R_{1max}} \, A_o \qquad (4.25)$$

where R_{1max} is the range in the rain. The actual rain echo is given by

$$\sigma_r = r_R \, r_a \, L \, \sigma_v \, k_{er} \qquad (4.26)$$

where

$$k_{er} = \int_0^{R_{1max}} e^{\int_R^{R_{1max}} -\alpha \, dR} \, dl \qquad (4.27)$$

This accounts for the different ranges for the same rain cell.

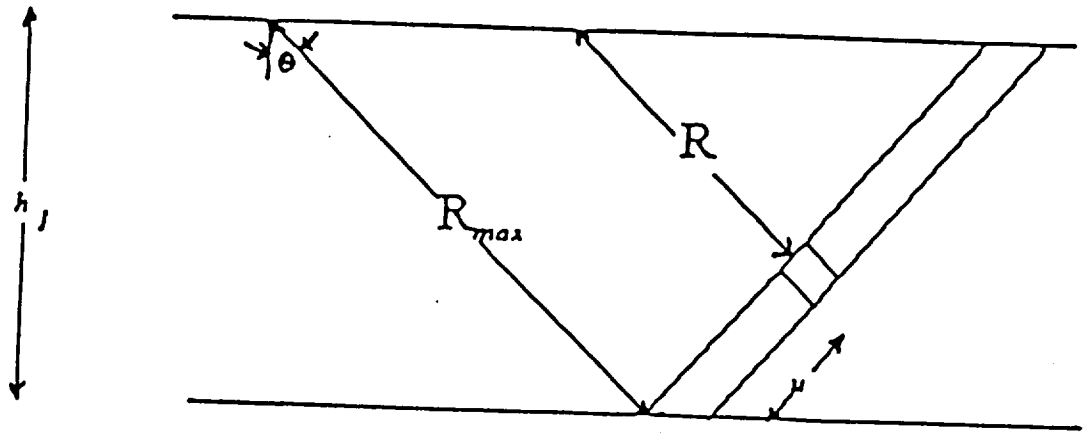

Fig. 4.4 Increasing attenuation of the returns from the same rain cell as we move from the top to the bottom. This is due to the longer path traversed through the rain volume by the returns from the bottom compared to those from the top.

The rain return involves

$$\sigma_v \, e^{-\int_R^{Rmax} \alpha \, dR} \, V_m \qquad (4.28)$$

where V_m is the volume and σ_v is the scattering coefficient and α is the attenuation coefficient in nepers/km. Since the range changes along the same rain cell (see Fig. 4.4) it is necessary to integrate the attenuation over these ranges. We can write (4.28) as

$$\sigma_v \, V_{eff} = r_a \, r_R \, \sigma_v \int e^{-\alpha \int_R^{R_{max}} dR} \, du \qquad (4.29)$$

From Fig. 4.4

$$\frac{R}{R_{max}} = \frac{(u_{max} - u)}{u_{max}} \qquad (4.30)$$

which may be written as

$$R = \frac{(u_{max} - u)}{u_{max}} \, R_{max} \qquad (4.31)$$

Now substituting $R_{max} = h_1 / \cos\theta$ and $u_{max} = h_1 / \sin\theta$ in (4.30) we have

$$R = \left(1 - \frac{u \sin\theta}{h_1}\right) \frac{h_1}{\cos\theta} \qquad (4.32)$$

and substituting in (4.32) in (4.29) we have

$$\sigma_v V_{eff} = r_a r_R \sigma_v e^{-\frac{\alpha h_1}{\cos\theta}} \int_0^{u_{max}} e^{\alpha u \tan\theta} du \qquad (4.33)$$

Evaluating the integral, and making the substitution $u_{max} \tan\theta = h_1 / \cos\theta$ we have

$$\sigma_v V_{eff} = \frac{r_a r_R \sigma_v}{\alpha \tan\theta} (1 - e^{-\frac{\alpha h1}{\cos\theta}}) \qquad (4.34)$$

Now, if we write

$V_{eff} = r_a r_R L_{eff}$ and compare both sides, we see that

$$L_{eff} = \frac{1 - e^{-\alpha R_{max}}}{\alpha \tan\theta} \qquad (4.35)$$

The equation is used to account for the variation of the attenuation in the same rain cell. This works only for α large enough that L is not limited by the beamwidth. If L be the actual length of the cell we may write $L_{eff} = K_{er}L$, where K_{er} is the attenuation factor. Evaluating

$$k_{er} = \left(\frac{1 - e^{-\alpha 2 R_{1max}}}{h_1 \alpha} \right) \cos(\theta) \qquad (4.36)$$

which is the two-way attenuation of each rain cell. Here R_{1max} is the range in the rain volume, and α from Table 3.5, is the attenuation coefficient in nepers/km, using the dB-to-nepers conversion. Substituting (4.36) in (4.26) will give the attenuated rain echo; similarly subtracting ($2 \alpha_{dB} R_{1max}$) from (4.25) will give the attenuated surface

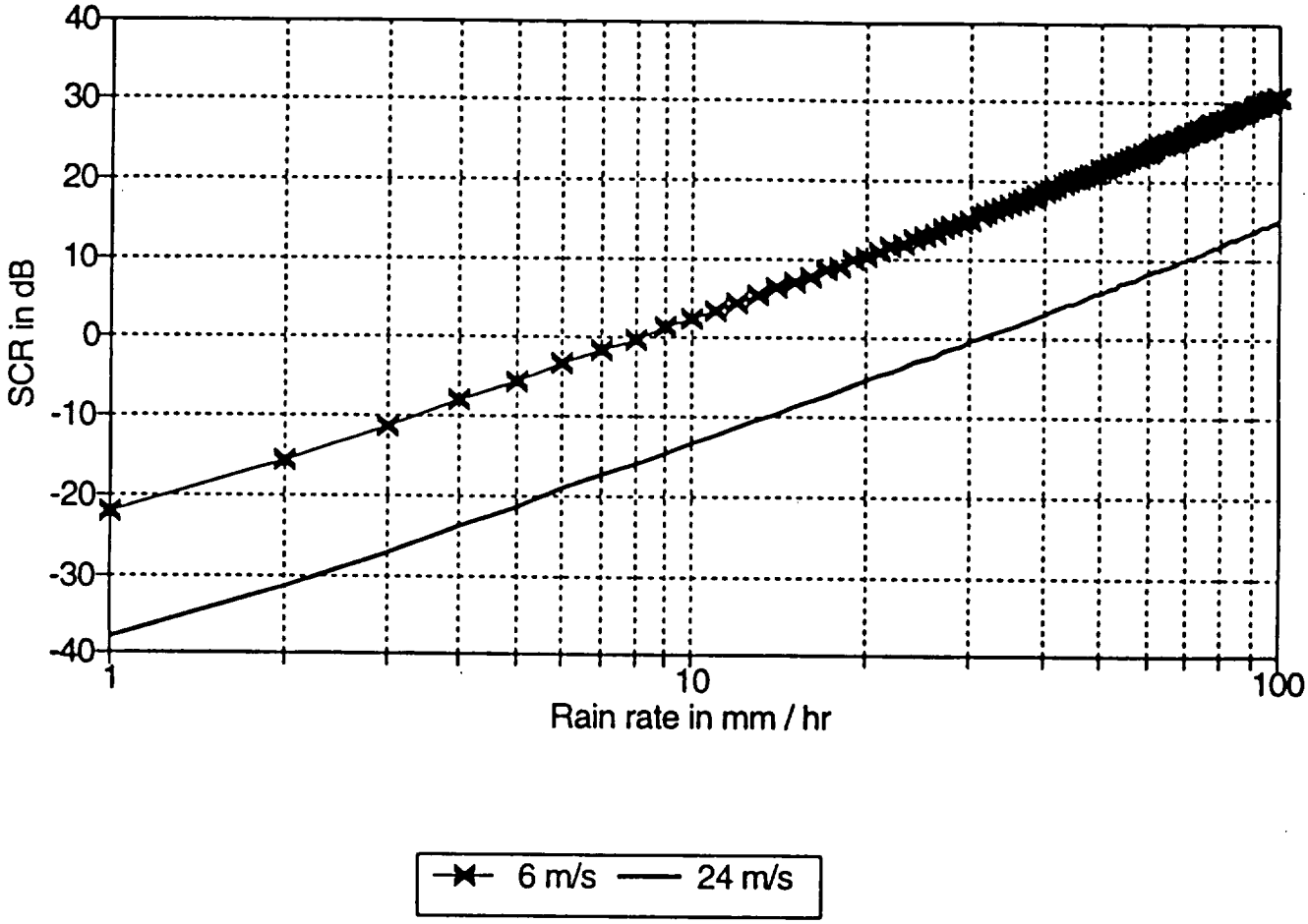

Fig. 4.5(a) Plot of the SCR in dB vs Rain rate in mm/hr at X-band, 60°, cross wind, for the given wind speeds.

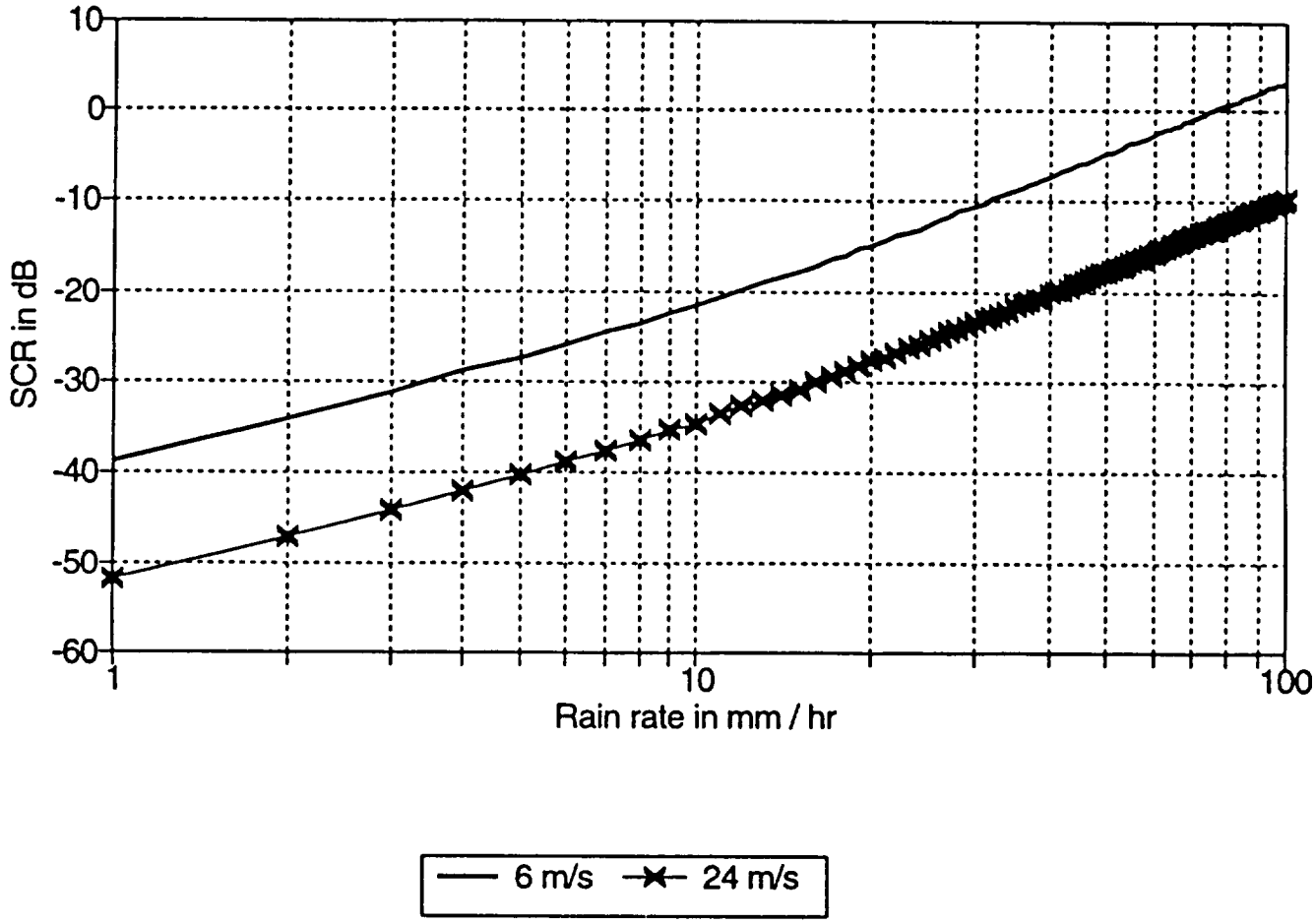

Fig. 4.5(b) Plot of the SCR in dB vs Rain rate in mm/hr at C-band, 60°, cross wind, for the given wind speeds.

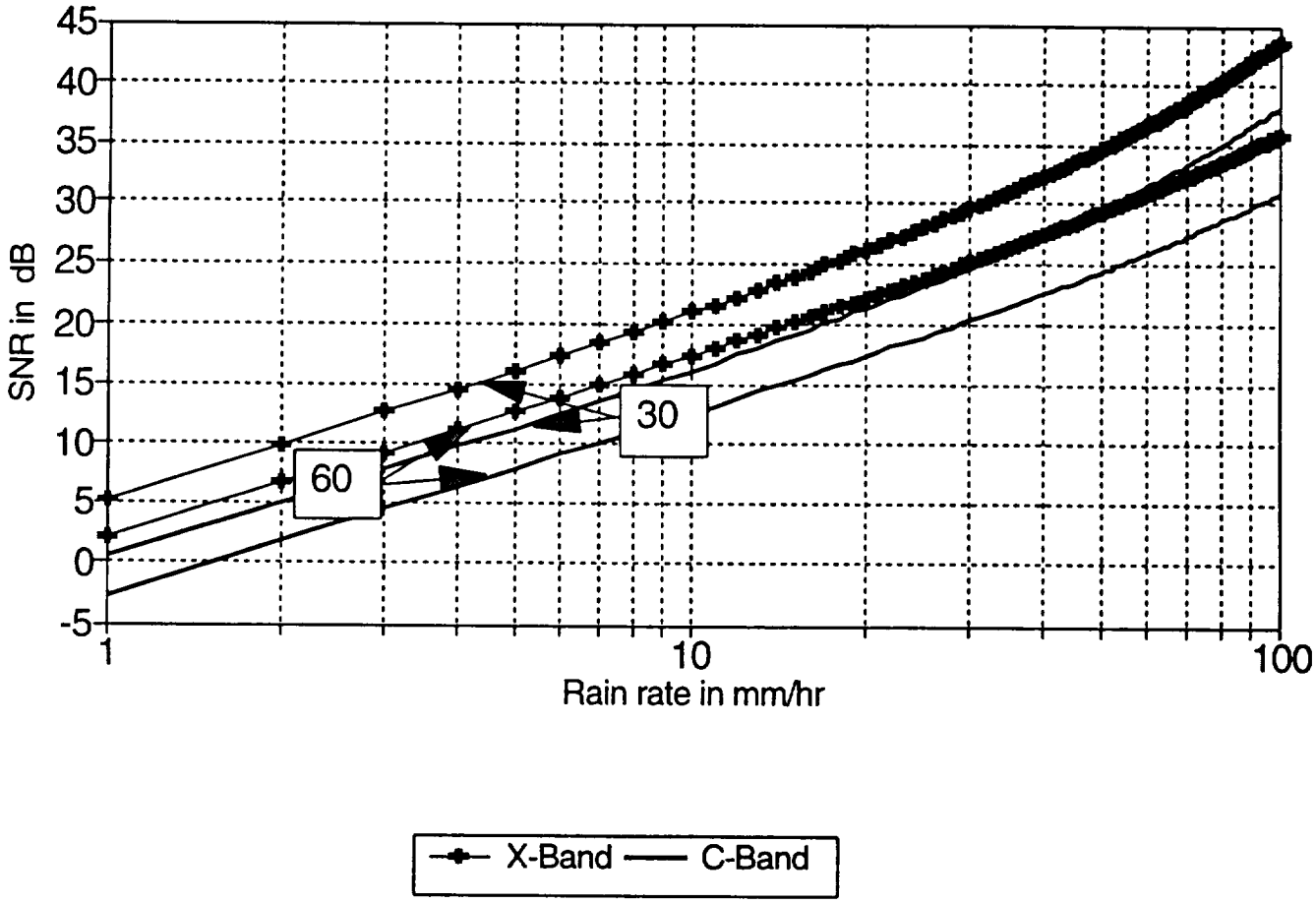

Fig. 4.6 Plot of the SNR in dB vs Rain rate in mm/hr at X and C bands for look angles of 30° and 60°.

$$\eta = \frac{\pi^5\ 300\ R^{1.5}|k|^2}{\lambda^4}\ 10^{-10} \qquad (4.39)$$

G is the gain, B is the bandwidth, L_s is the system loss, L_b is the signal loss due to absorption by the ice melting layer, η is the rain reflectivity, k_{er} is the attenuation due to rain from (4.28), and F is the receiver noise figure. The other parameters have their usual meaning. The plots in the Fig. 4.6 are made from the data generated using (4.30) for different angles of incidence at X-and C-band.

This SNR calculation is based on the assumption that the entire beam volume below the cloud top is rain-filled. If this is not true the SNR will decrease. The result of this is that the minimum detectable rain rate increases for fixed SNR. Studies show that a typical rain storm diameter for rain rates of 10 to 15 mm is 10 to 15 km (see Fig. 4.7) (Goldhirsh and Rowland, 1982). Thus, relative large storm diameters may be expected at lower rain rates, and the probability of partial beam filling along track is low. If however the cross-track beam is only partially filled we may consider the region 2 discussed earlier to a be special case of regions 1 and 3; i.e., there will be at least a few ideal rain cells.

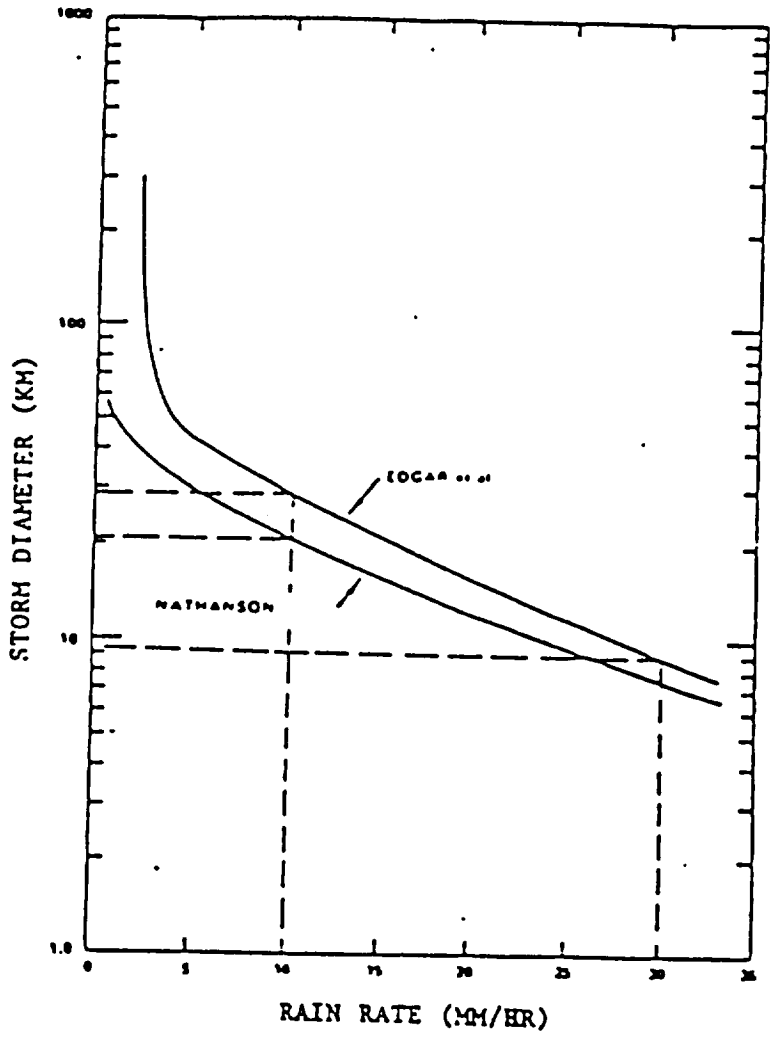

Fig. 4.7 Typical rainstorm diameter for the given rain rates (Goldhirsh and Rowland, 1982)

CHAPTER V
CALCULATIONS AT NADIR

5.1 INTRODUCTION

In Chapter-IV it was concluded that it would be possible to measure rain rates in excess of 30 mm/hr at angles of incidence greater than 60°. Here we consider the radar pointed at vertical. At vertical it is seen that, due to the non ideal nature of the transmitted pulse, there is considerable clutter coupled with the rain echo. When measurements are made at vertical, the problems are somewhat different than at the angles well away from vertical. Further, the geometry is different because of the presence of both beam-limited and range limited conditions. This means that the volume of the resolution cell depends upon its position in the beam.

5.2 GEOMETRY

The echo power for the SAR is identical to that for the conventional real aperture radar, using the same antenna. Hence, will use the same geometry as that of real-aperture for power calculations. Fig. 5.1 shows the geometry for the vertical incidence. The rain volume may be divided into three regions:

Region 1. where there is partial beam filling due to the pulse intercepting the cloud top.

Region 2. where the cells are assumed to be completely rain filled.

Region 3. where the rain cells intercept the surface.

Here we consider calculations only for those cells that are completely rain filled (ideal rain cells).

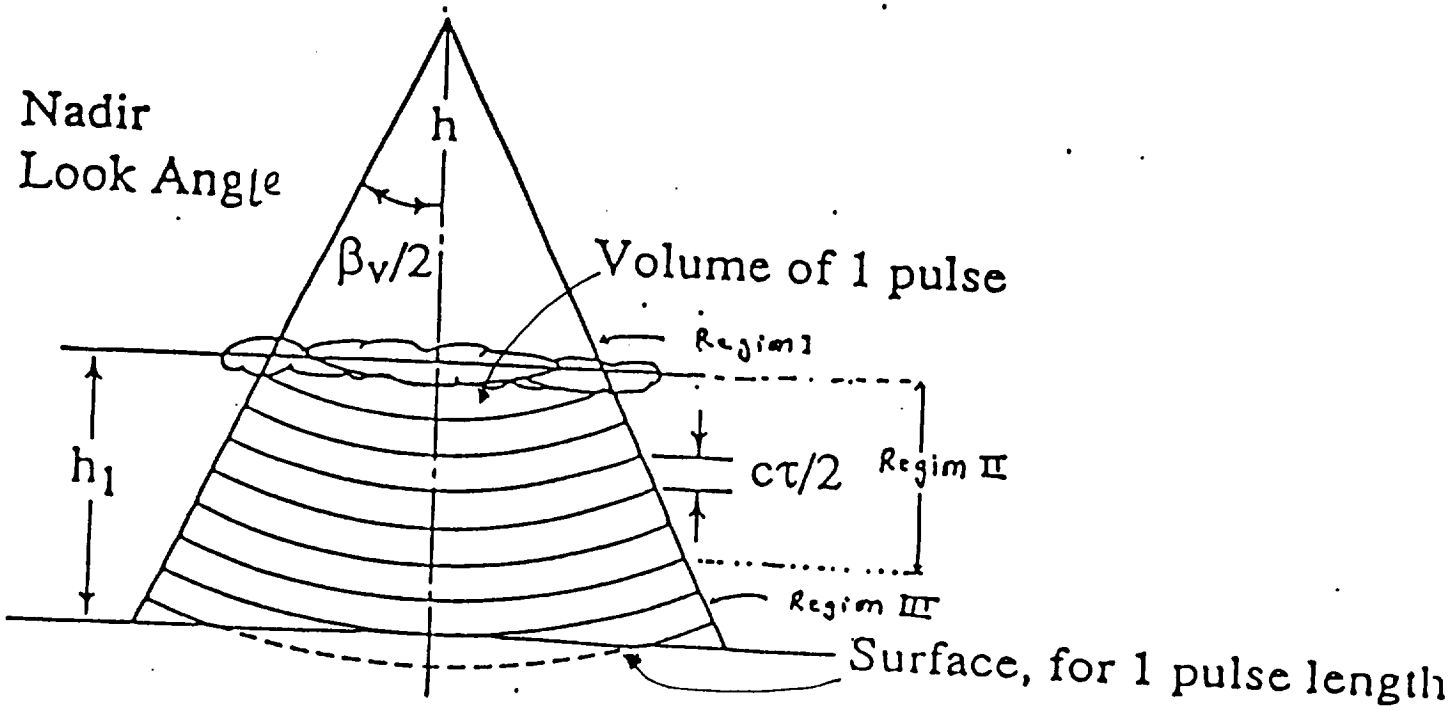

Fig. 5.1 Geometry at vertical illustrating the volume of one pulse and identifying three regions.

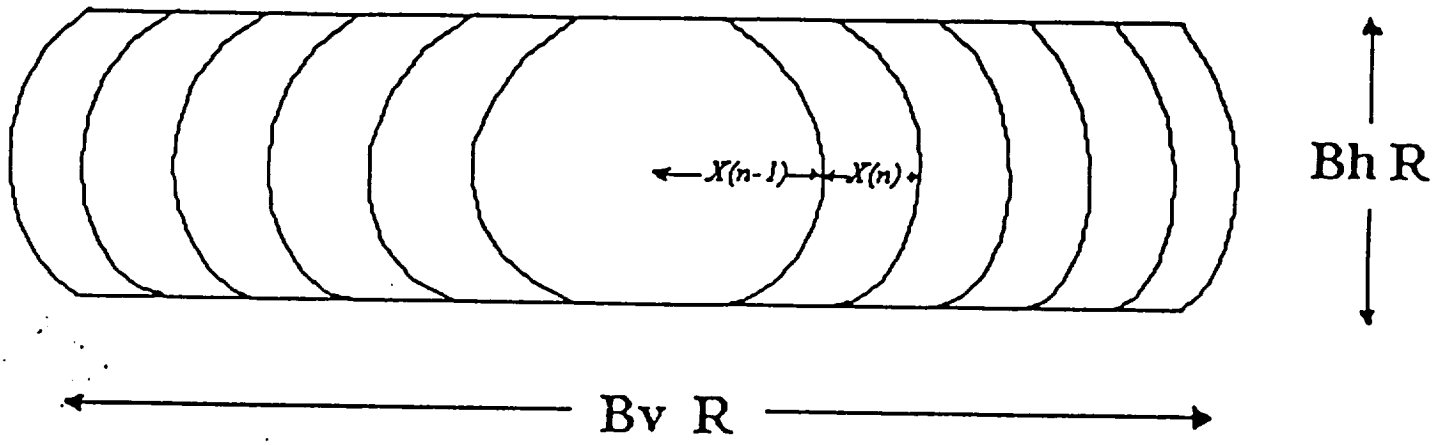

Fig. 5.2 Geometry at vertical on the ground. This is used to calculate the area of the surface coupled to each range cell.

return, where α_{dB} is the attenuation dB/km. We substitute these attenuated returns in (4.22) to obtain a realistic estimate of the SCR; this is plotted in Fig. 4.5(a) and 4.5(b) for X- and C-bands.

It is seen that for low rain rates the X-band signal lies far below the clutter for lower angles of incidence of ($\theta < 50°$). However, for higher angles, the clutter lies below the signal for moderate rain rates at low wind speeds. At C-band the clutter is very large, Fig. 4.5(b).

4.4 THE SIGNAL-TO-NOISE RATIO

From Chapter-III we have the radar equation for meteorology. From Fig. 4.2 the volume of the radar beam for the off-vertical look angle may be expressed in terms of the horizontal and the vertical beam widths for a pulse of duration τ as

$$V_m = \frac{\pi}{4} \frac{\beta_h R h_1 c \tau}{2\sin(\theta_{av})} \qquad (4.37)$$

where h_1 is the thickness of the rain region. This volume corresponds to the cells of interest; i.e., the ideal rain cells discussed in the previous sections. The resulting equation for the SNR is

$$SNR = \frac{P_t}{K T B F} \frac{G^2 \lambda^2 \beta_h c \tau h1 \eta L_s L_b^2}{512 \pi^2 R^3 \sin(\theta_{av})} k_{er} \qquad (4.38)$$

where

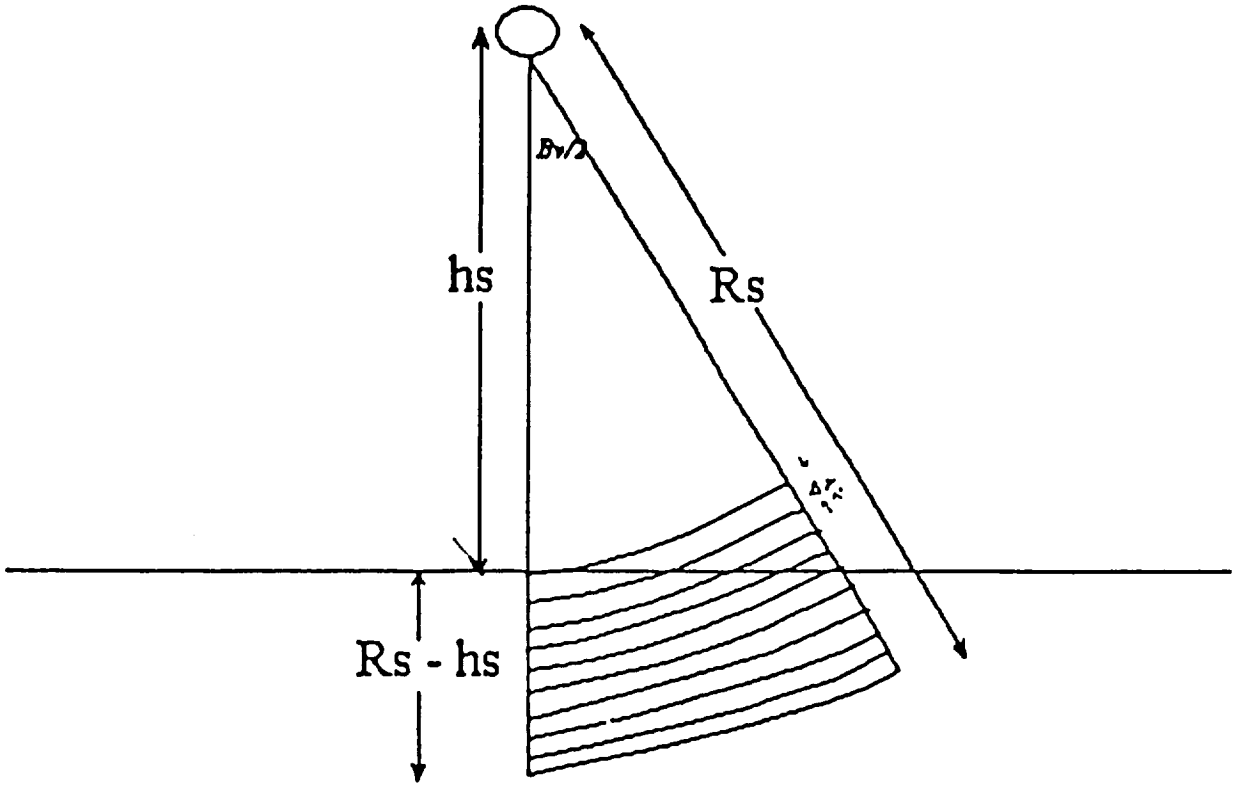

Fig. 5.3 Geometry to calculate the total number of range cells cluttered with the surface echo.

The volume of these rain cells is

$$V_n = \frac{\pi}{4}\ \beta_h\ \beta_v\ r_R\ R_n^2 \qquad \textbf{(5.1)}$$

where R_n is the range to the cell in question, β_h and β_v are the horizontal and the vertical beam widths, and r_R is the vertical resolution. The factor of $\pi/4$ accounts for the elliptical shape of the beam. The ground area coupled to each cell except the first can be calculated, assuming the area is approximately rectangular (see Fig. 5.2), as

$$A_n = 2\ \beta_h\ R_n(\ x(n)\ -\ x(n-1)\ ) \qquad \textbf{(5.2)}$$

and the ground area coupled to the first cell is given by

$$A_1 = 2\ \beta_h\ R_n\ x(1) \qquad \textbf{(5.3)}$$

where

$$x(n) = R_n \sin(\theta_n) \qquad \textbf{(5.4)}$$

$$\theta_n = \cos^{-1}\left(\frac{h_s}{R_n}\right) \qquad \textbf{(5.5)}$$

and

$$R_n = h_s + n\ r_R \qquad \textbf{(5.6)}$$

We define h_s as the shuttle altitude, R_n as the range to the particular cell in question and n as the cell number ranging from 1 to m. To calculate m, the total number of cells coupled to the ground, we use the relation

$$m = \frac{R_s - h_s}{r_R} \qquad (5.7)$$

where R_s is the maximum slant range to the ground (see Fig. 5.3)

$$R_s = \frac{h_s}{\cos(\beta_v/2)} \qquad (5.8)$$

5.3 SIGNAL-TO-NOISE RATIO

From Chapter-III, the radar equation for meteorology for vertical look angle is

$$SNR_n = \frac{P_t}{K\ T\ B\ F} \frac{G^2\ \lambda^2\ \beta_h\ c\ \tau\ \eta\ L_b\ L_s}{1024\ \pi^2\ R^2}\ k_{er}[Rr] \qquad (5.9)$$

where

$$\eta = \frac{\pi^5\ 300\ R^{1.5}\ |k|10^{-10}}{\lambda^4} \qquad (5.10)$$

Here G is the gain, B is the bandwidth, L_s is the system loss, L_b is the signal loss due to absorption by the melting ice layer, η is the rain reflectivity, F is the receiver noise figure, and the other parameters have their usual meaning.

C-2.

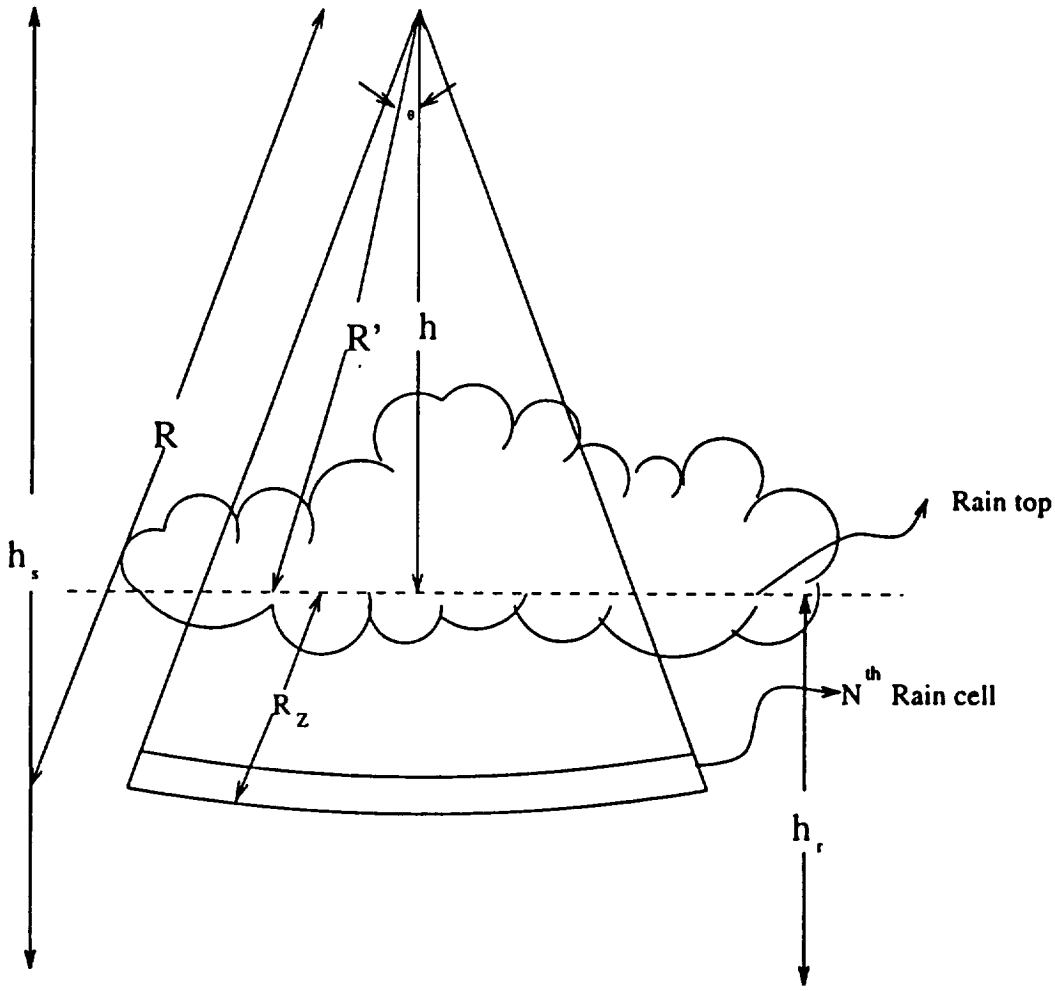

Fig. 5.4 Vertical geometry modified to illustrate that the volume of the range cell changes within the rain volume due to beam spread.

From Fig. 5.4 it is seen that the volume occupied by the rain above each rain cell changes from one end of the cell to the other. This is due to the fact that pulse volume is curved whereas the rain top is not. Hence the signal from the cell edge suffers less attenuation than the center. To account for this it is necessary to integrate the attenuation over the entire pulse volume. Here it is necessary to make the assumption that the cell has constant attenuation in the azimuth direction. The rain returns involve

$$\sigma_v \frac{\pi}{4} \beta_h r_R \int_{-\frac{\beta_v}{2}}^{\frac{\beta_v}{2}} R^2 e^{-\alpha R_z} dR \qquad (5.11)$$

we may write R = (h + n r_R) where n is the cell number under consideration, r_R is the range resolution and h is the height to the shuttle from the rain top. To account for the variation of the distance travelled by the signal in the rain volume it is assumed that the beamwidth can be divided into number of small angles. From Fig. 5.4

$$R_z = h + n r_R - \frac{h}{\cos\theta} \qquad (5.12)$$

where θ varies from - βv/2 to βv/2. Substituting (5.12) in (5.11) for the rain returns we have

$$\sigma_v \frac{\pi}{4} \beta_h r_R (h + n r_R)^2 \int_{-\frac{\beta_v}{2}}^{\frac{\beta_v}{2}} e^{-\alpha \left(\frac{h(\cos\theta - 1)}{\cos\theta} + n r_R \right)} d\theta \qquad (5.13)$$

Here the attenuation coefficient

$$k_{er} = \int_{-\frac{\beta_v}{2}}^{\frac{\beta_v}{2}} e^{-\alpha\left(\frac{h\,(\cos\theta - 1)}{\cos\theta} + n\,r_R\right)}\, d\,\theta \qquad (5.14)$$

$$k_{er}[Rr] = \int_{-\frac{\beta_v}{2}}^{\frac{\beta_v}{2}} e^{-2\,\alpha[Rr]\,\left(h_d\left(\frac{\cos(\theta)-1}{\cos(\theta)}\right) + h_k\right)}\, d\theta \qquad (5.15)$$

where

$$\alpha[Rr] = \frac{b\,Rr^{\,c}}{8.66} \qquad (5.16)$$

The values of *b* and *c* depend on the frequency used (see Table 3.5), h_d is the shuttle's height above the top of the rain cell and h_k is the distance of the rain cell from the rain top. Using (5.9) we plot the SNR in dB vs rain rate in Fig. 5.5 for X- and C-bands.

Only calculations for the cells that are entirely rain filled are presented here. For partially rain-filled cells, the SNR decreases in proportion to the rain-filled volume.

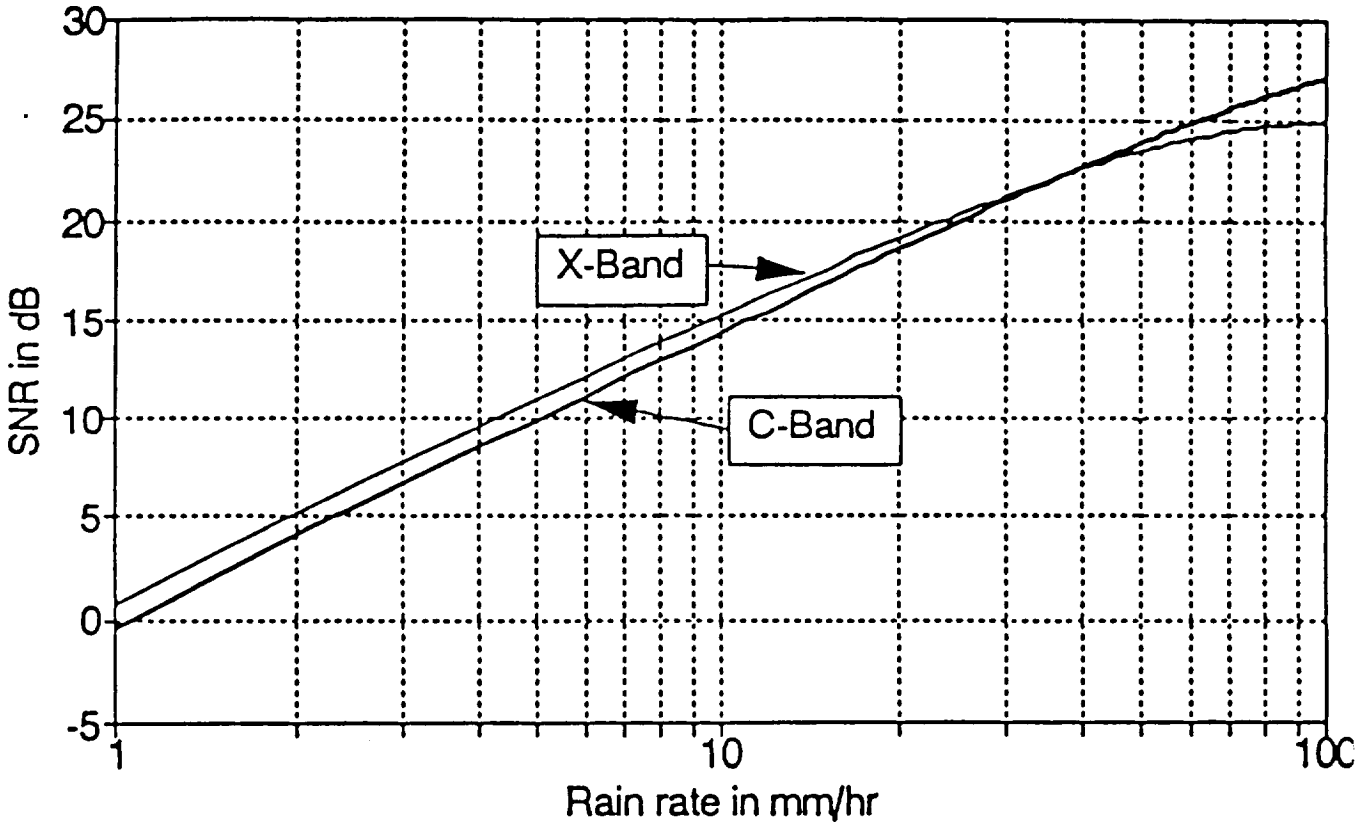

Fig. 5.5 Plot of the SNR in dB vs Rain rate in mm/hr at X- and C-Band for the vertical geometry.

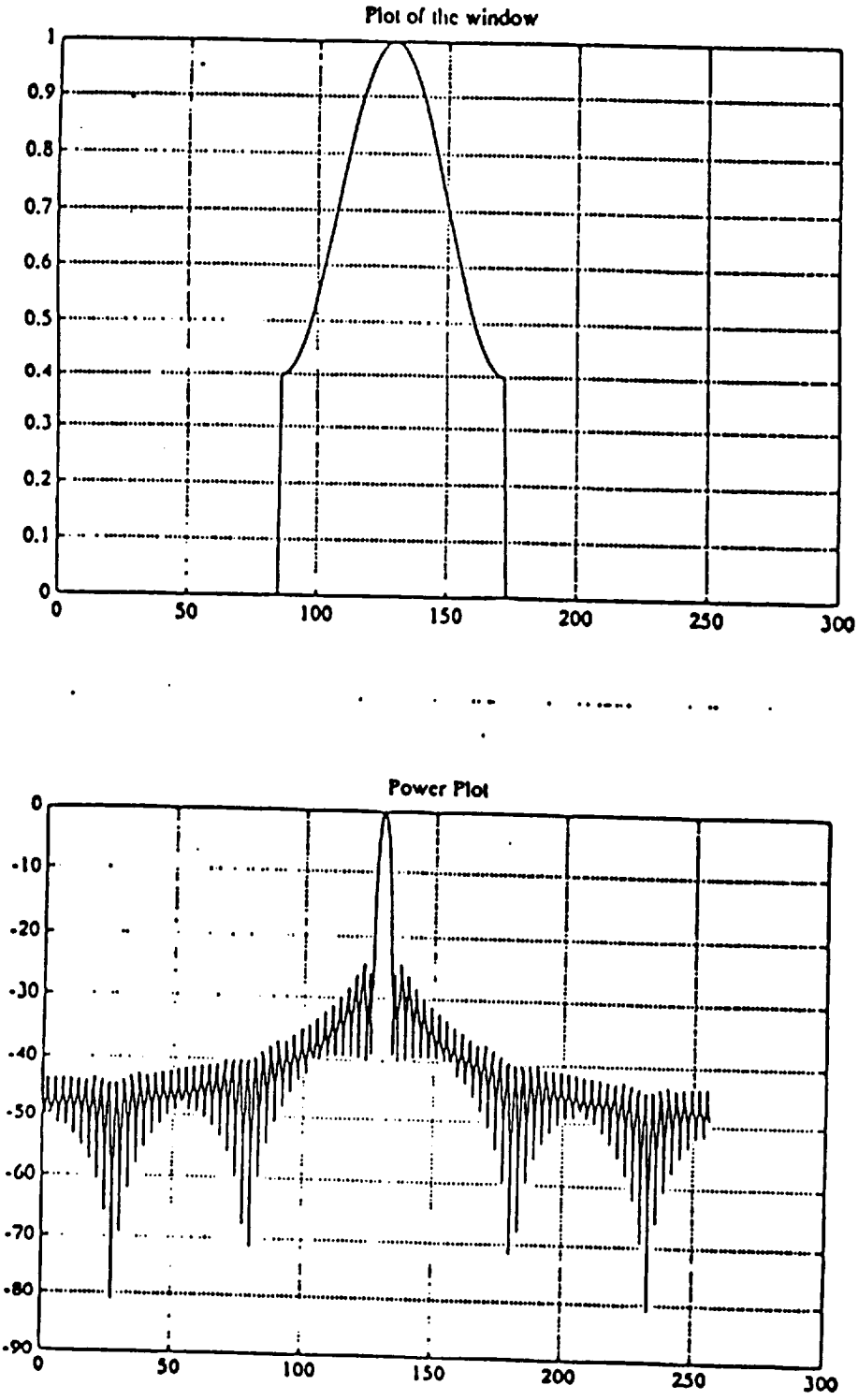

Fig. 5.6 Range sidelobes of a pulse with a raised $\cos^2$ weighting with a 0.4 pedestal.

5.4 SIGNAL-TO-CLUTTER RATIO.

The backscatter method uses the returned echo from the rain to compute the rain rate. For vertical incidence the surface returns, coupled by the antenna sidelobes, arrive simultaneously with the desired echo and increase in magnitude as we approach cells near the surface. Since the echo from the rain should be substantially above the surface echo, we compute the SCR.

The scattering coefficient of the rain, when λ is in centimeters, is

$$\sigma_v = \frac{\pi^5}{\lambda^4} Z |K|^2 10^{-10} \qquad \textbf{(5.14)}$$

Using the appropriate volume from (5.1) and the extinction coefficient from (5.15)

$$\sigma_r = \sigma_v V \frac{k_{er}[Rr]}{\beta_v} \qquad \textbf{(5.18)}$$

and the appropriate area coupled to the rain cell from (5.2) in

$$\sigma_g = \sigma_o(A_n), \qquad \textbf{(5.19)}$$

where the magnitude of σ^o depends on the type of surface. We compute the SCR

$$\Delta\sigma_{dB} = \sigma_{r_{dB}} - \sigma_{g_{dB}} \qquad \textbf{(5.20)}$$

where

$$\sigma_{r_{dB}} = 10 \log(\sigma_r) \qquad \textbf{(5.21)}$$

and

$$\sigma_{gdB} = 10 \log(\sigma_{gT}) \qquad (5.22)$$

For the ideal case, the clutter coupled to the rain returns by range sidelobes is negligible. However in practice the surface return from range sidelobes arrives at the receiver at the same instant as the desired rain echo. The range sidelobe level with a raised $\cos^2$ window is low, with the first side lobe about 21 dB down. However, due to the very large magnitude of the surface clutter and due to the fact that the side lobes fall too slowly (see Fig. 5.6), almost all rain cells in the present configuration have significant clutter coupled to them. Fig. 5.6 shows that the magnitude of the sidelobes that are coupled to the surface echo depends on the cell for which the calculations are made. Further, the sidelobes that are coupled to the ground return change in magnitude with the cell under consideration. To account for this, using (5.7) and the cell number under consideration, it is possible to obtain the exact number of side lobes coupled to the ground. Their magnitude $Sl_{dB}(n)$, can be obtained from the figure. The weighted clutter coupled to the cell under consideration is obtained as

$$\sigma_{gT}(R_r) = \sum_n \sigma_g(R_r, n)\ 10^{0.1\, Sl_{dB}(n)} \qquad (5.23)$$

where

$$\sigma_g(R_r, n) = \frac{A_n\, K_{er}[Rr]\ 10^{0.1\,\sigma_o}}{\beta_v} \qquad (5.24)$$

Since the vertical-incidence surface echo is so strong, returns due to the antenna

sidelobes are negligible compared to those due to the range sidelobes. Hence all clutter calculations are made using the range sidelobes.

Near vertical incidence the signals produced by the Bragg-scattering mechanism are dominated by those produced by the geometric optics or physical-optics mechanism. In this region the slopes are such that one can achieve specular reflection from the facets on the surface of the sea, and many facets having narrow backscattering patterns are close enough to the specular condition that signal returned from them by the quasi-specular mechanism are strong. At and near vertical incidence the strongest reflection would occur with a perfectly flat surface or one that was very undulating. As the surface gets rougher, more of the vertically incident energy is scattered away from the radar receiver. Hence the radar backscattering decreases with the increasing wind-speed and wave height near vertical, whereas it increases with increasing wind speed at angles beyond 12°.

In vegetation scattering, the air-vegetation boundary usually is unimportant. Hence, in general we have a combination of volume scattering in the vegetation layer and surface scattering by the underlying ground. It is seen that the surface scattering decreases rapidly with increasing θ for angles close to vertical, while the volume scattering decreases very slowly with increasing θ. Unless the canopy is dense we expect that the backscatter due to the soil to be at-least as important as the volume scattering. In tropical rain forests, the canopy is dense enough that we need not consider the backscatter from the soil.

For vertical incidence the scattering coefficient of the ocean at 13.9 GHz is close to 12 dB for wind speed of 10 m/s (Schroeder, et al.,1985) and that of forest to be -6 dB (Ulaby, et al.,1986). Using (5.20), plots of the SCR for various rain thicknesses over ocean are compared with SCR over forest for rain thickness of 1 km at X-band (see Fig. 5.7(a)).

The transmitted pulse is chirped and the weighting used is a raised $\cos^2$ with a 0.4 pedestal. Ideal $\cos^2$ weighting is difficult to achieve because of the imperfection in amplitude and phase response and various non-linearities in amplifiers. However, even if the ideal $\cos^2$ weighting could be achieved it would widen the range resolution. Fig. 5.7(b) shows the comparison between the SCRs obtained using a raised $\cos^2$ window and an ideal $\cos^2$ window over the ocean at X band. Fig. 5.7(c) and 5.7(d) show corresponding comparisons at C band. From the figures it is seen that the X-band and C-band SCR with a raised $\cos^2$ window is poor over the ocean for shallow rain thickness. However over the forest the SCR appears to be reasonable even for shallow rain thickness with a raised $\cos^2$ window. Further for both X and C bands the SCR is expected to be good even for shallow rain thickness over ocean if an ideal $\cos^2$ weighting could be achieved. The X-SAR has the capability of transmitting a short 3 μsec pulse and processing it without dechirping it (Fuk Li, 1994). This results in a wider range resolution (450 m) but the sidelobe problem is eliminated. This means that rain at an altitude as low as 500 m above the ground can be detected.

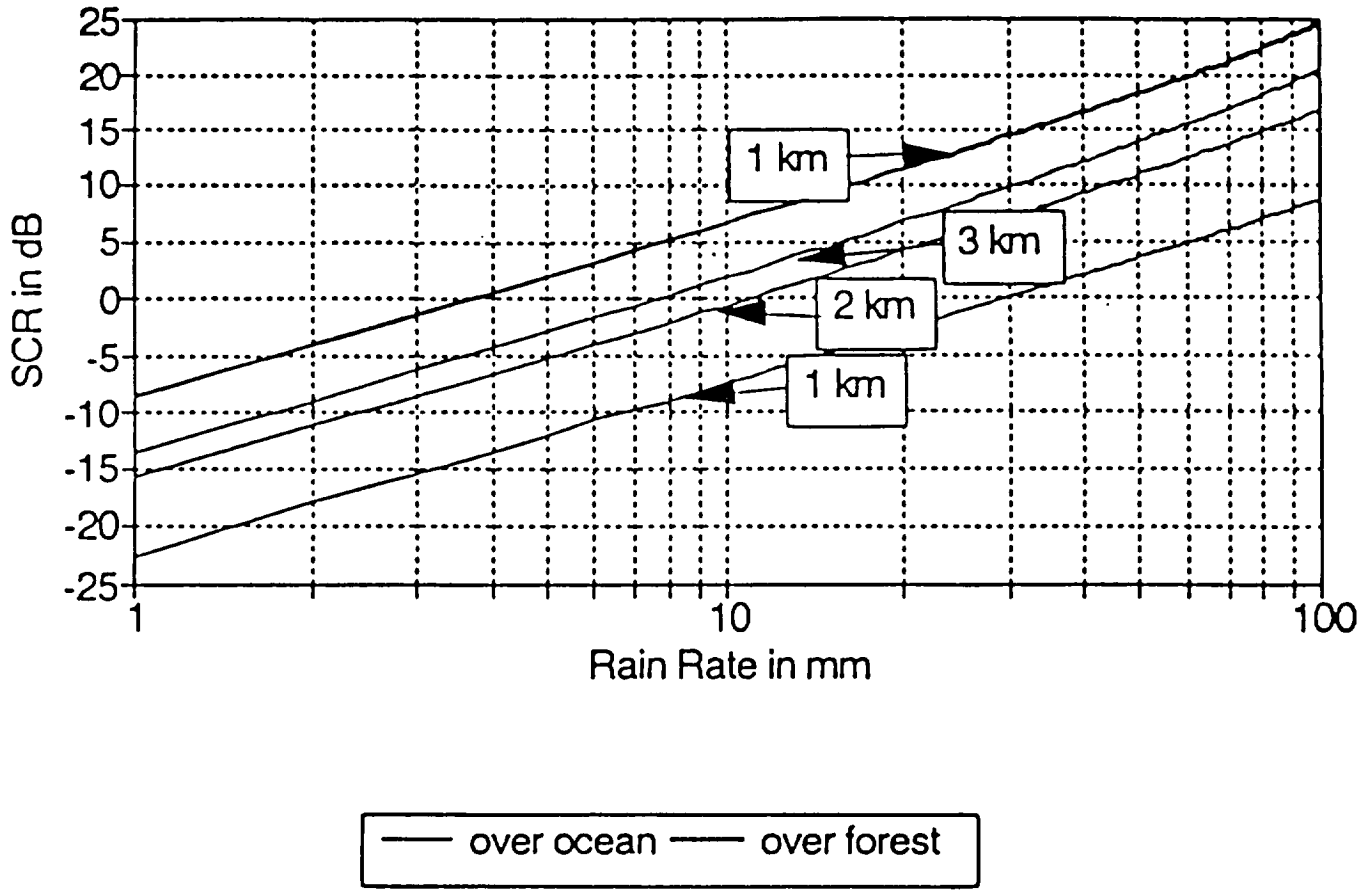

Fig. 5.7(a) Comparison of the SCR in dB vs Rain rate in mm/hr over forest to that over ocean at X-band for the vertical incidence.

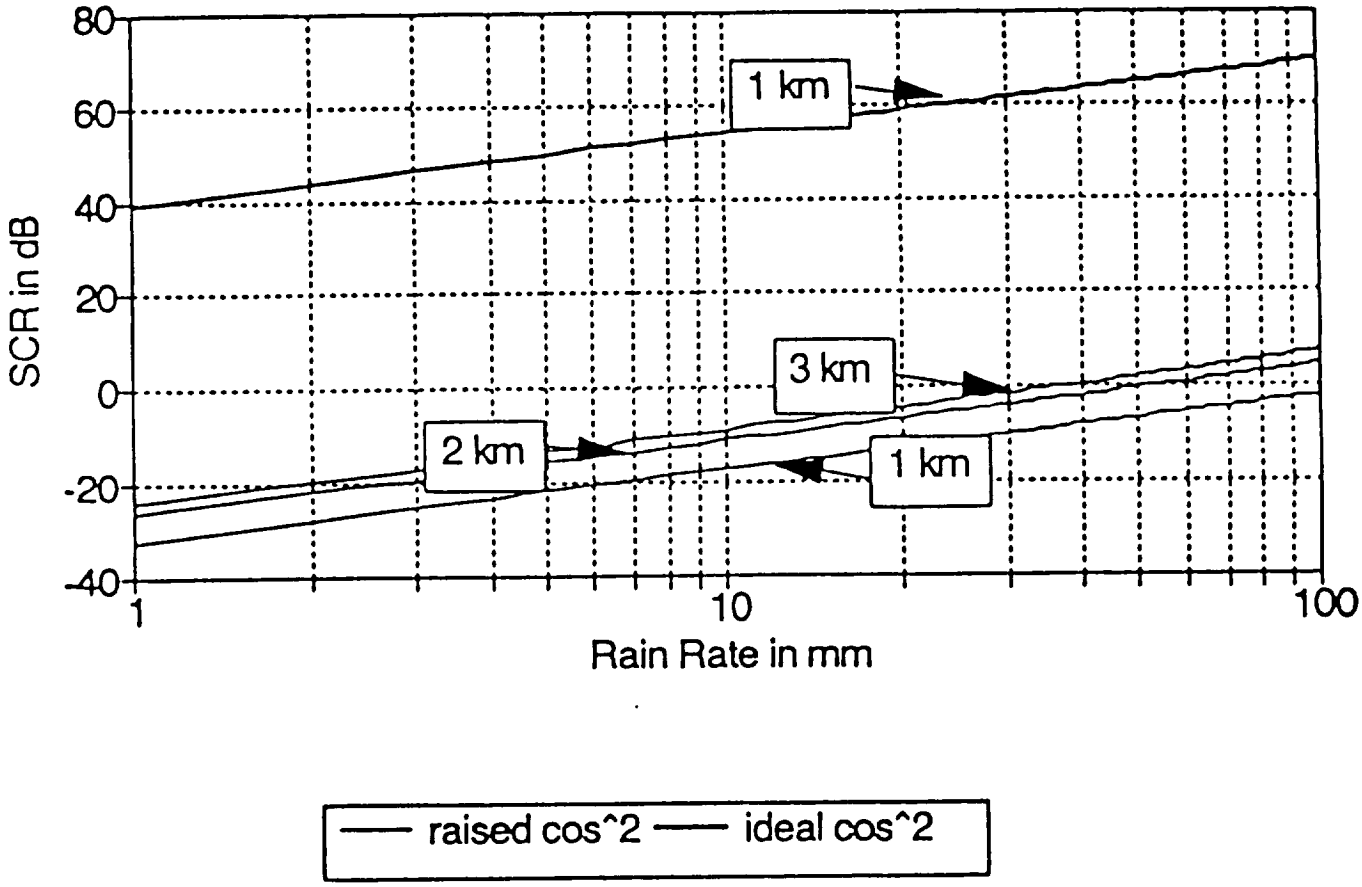

Fig. 5.7(b) Comparison of the SCR in dB vs Rain rate in mm/hr over the ocean at X-band, vertical incidence, obtained by using the raised $\cos^2$ weighting to that obtained by use of ideal $\cos^2$ weighting.

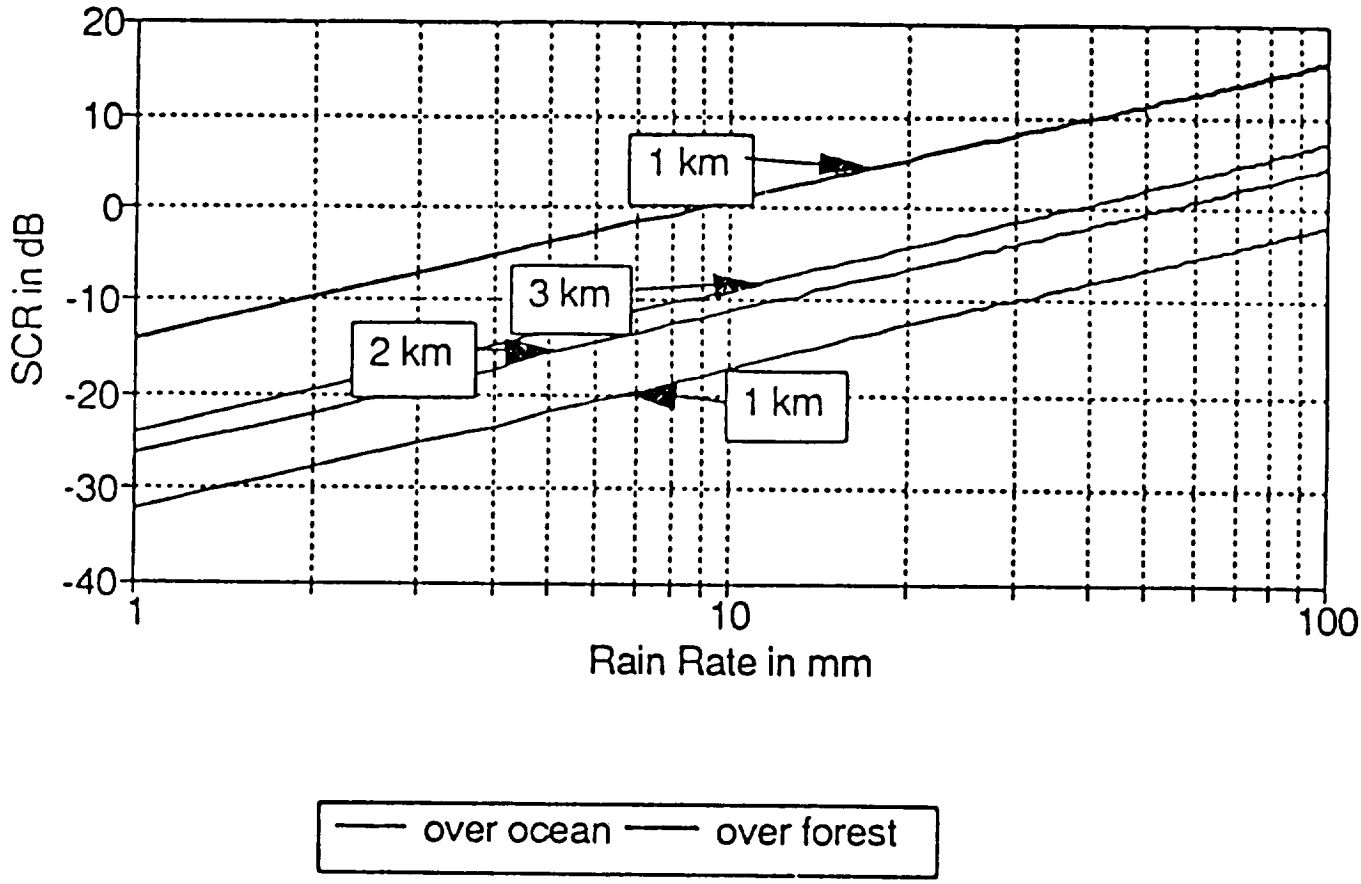

Fig. 5.7(c) Comparison of the SCR in dB vs Rain rate in mm/hr over forest to that over the ocean at C-band, vertical incidence.

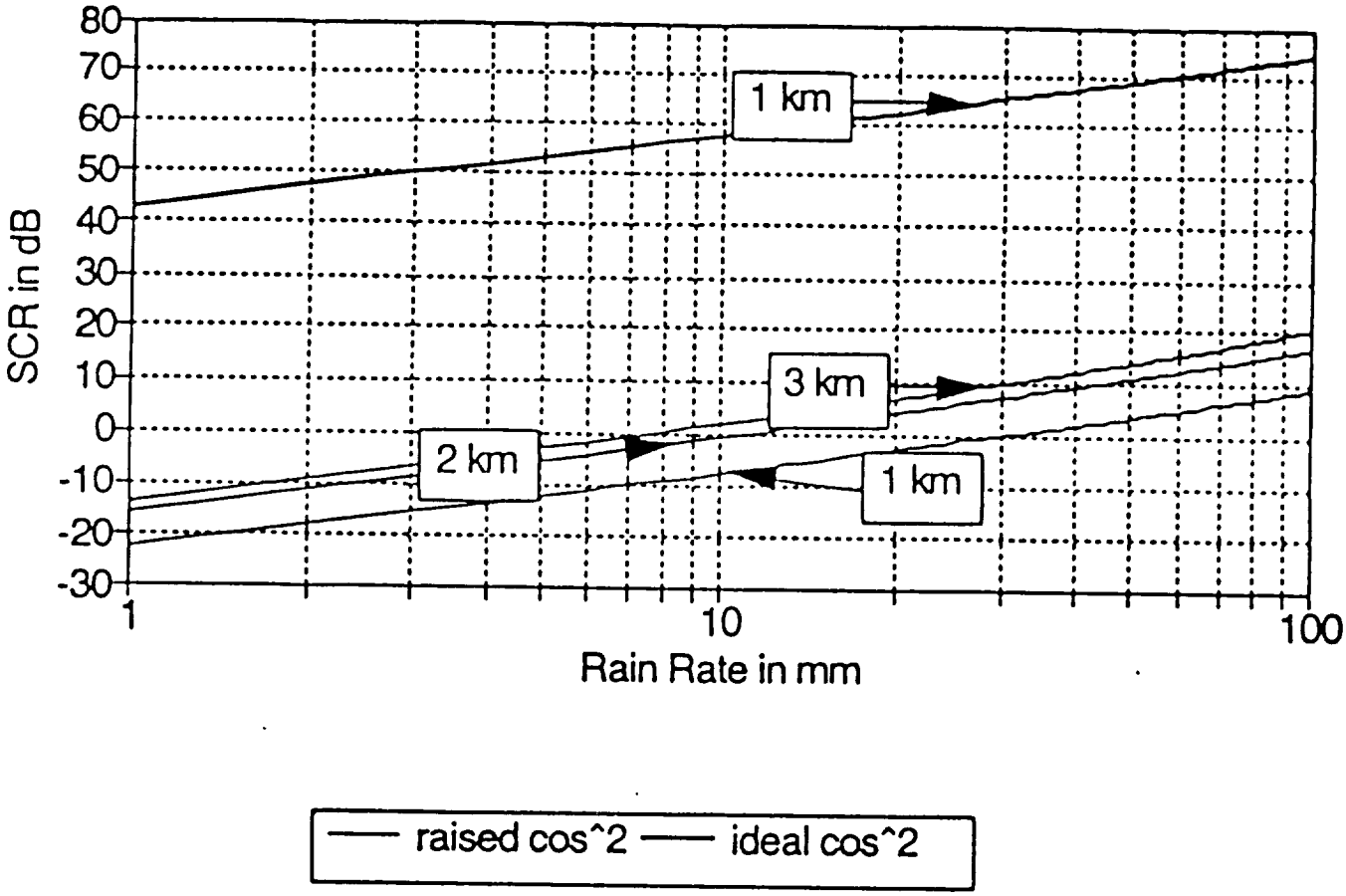

Fig. 5.7(d) Comparison of the SCR in dB vs Rain rate in mm/hr over the ocean at C-band, vertical incidence, obtained by using the raised $\cos^2$ weighting to that obtained by use of ideal $\cos^2$ weighting.

CHAPTER VI
ESTIMATION OF THE SIGNAL IN THE PRESENCE OF LARGE CLUTTER

6.1 INTRODUCTION

The principal limitation for the use of a spaceborne imaging SAR as a rain radar is the surface-clutter problem. Signals may be estimated in the presence of noise by averaging large numbers of independent samples. We applied this method here to obtain an estimate of the rain echo by averaging a set of N_c samples of the clutter in a separate measurement and subtracting the clutter estimate from the combined estimate.

Chapters IV and V show that there is adequate signal-to-clutter ratio (SCR) for the experiment to be feasible only at high rain rates that have a small probability of occurrence. However, signals from smaller rain rates that are more common are swamped by the surface clutter. The model used in the SCR calculations at X-band is the SASS model described by

$$NCRS(dB) = 10\,[G(\theta,\chi) + H(\theta,\chi)\,\log_{10} U] \qquad \textbf{(6.1a)}$$

and the model used in the SCR calculations at C-band is the ESAs CMOD4 described by

$$\sigma_0 = K_b\,[1+k_1\cos(\phi)+k_3\tanh(k_2)\cos(2\phi)]^{1.6}\,10^{(\alpha+\gamma\,\Psi(v+\beta))}$$

Fig. 4.5(a) and (b), which have plots of SCR vs rain rate for off-vertical angles of incidence, show that, at lower rain rates, the SCR (in dB) is negative. This is also the case for vertical incidence, as seen from Fig. 5.7(a) and Fig. 5.7(c). This situation is analogous to the estimation of a low signal in a noisy environment. It is possible to

estimate the signal even when the SNR (in dB) is negative, if many independent samples are available. We extended this concept to estimating the signal with negative SCR.

6.2 MEASUREMENT IN THE PRESENCE OF CLUTTER

A radiometer operates with a signal-to-noise ratio (SNR) that is much less than unity, and radars with a reasonable number of independent samples of fading can operate with an SNR of the order of unity or even less. Two samples may be considered as independent if they are far enough apart so that the correlation between them is essentially zero, which usually occurs when the spacing between the samples is large compared with the reciprocal of the bandwidth. Each pixel in a side-looking airborne radar (SLAR) image usually represents an average of several independent samples, although the number is small. Each synthetic-aperture radar (SAR) pixel could represent only one sample, but it usually contains 3 or 4 samples (multilook).

At the input of the receiver the received voltage is the sum of the mean values of the signal v_s' and the noise v_n.

$$V_r = V_s' + V_n \tag{6.2}$$

The mean value of the received power is the sum of the mean values of the signal and noise power because the random phase causes cancellation of the cross terms in the mean, giving

$$P_r = P_s' + P_n \ , \qquad (6.3)$$

where P_n is the noise power.

Now, the signal power may be broken up into two components $P_s' = P_s + P_c$, where P_s is the power returned from the rain and P_c is the power returned from the surface. We may express the mean received power in terms of the SNR S_n and SCR S_c as

$$P_r = P_s\left(1 + \frac{1}{S_n} + \frac{1}{S_c}\right) \qquad (6.4)$$

When N_r independent square-law-detected samples of the received signal are averaged, the standard deviation of the average is

$$\sigma_{rdN} = \frac{P_s}{\sqrt{N_r}}\sqrt{\left(1 + \frac{1}{S_n} + \frac{1}{S_c}\right)} \qquad (6.5)$$

When the SNR is high enough the estimate of clutter alone can be obtained by averaging a set of N_c samples of clutter in a separate measurement. The standard deviation of the clutter alone is (neglecting noise)

$$\sigma_{cdN} = \frac{P_c}{\sqrt{N_c}} \qquad (6.6)$$

An estimate of received signal can be obtained by taking the difference between estimates of combined signal and clutter and clutter alone.

$$P_s = P_{rd} - P_{cd} \tag{6.7}$$

The variance of either a sum or difference of two independent random variables is the sum of the variances of the individual components, hence the variance of signal alone is

$$\sigma_s^2 = \sigma_{rdN}^2 + \sigma_{cdN}^2 \tag{6.8}$$

Now if we assume that compared to the SCR, the SNR is very high, and substitute from (6.5) and (6.6) we obtain

$$\sigma_s^2 = \frac{P_s^2}{N_r}\left(1 + \frac{1}{S_c}\right) + \frac{P_c^2}{N_c} \tag{6.9}$$

Rearranging

$$\frac{\sigma_s}{P_s} = \sqrt{\frac{\left(1 + \frac{1}{S_c}\right)^2 + \left(\frac{1}{S_c}\right)^2 K}{N_r}} \tag{6.10}$$

where $K = N_r / N_c$. When $N_r = N_c$ K is 1. We may use (6.10) as a measure of the estimate of signal in presence of clutter. Solving for the number of independent samples N_r, for K=1, we have

$$N_r = \frac{\left(1 + \frac{1}{S_c}\right)^2 + \left(\frac{1}{S_c}\right)^2}{\left(\frac{\sigma_s}{P_s}\right)^2} \tag{6.11}$$

At lower SCR the number of samples required for successful estimation increases rapidly.

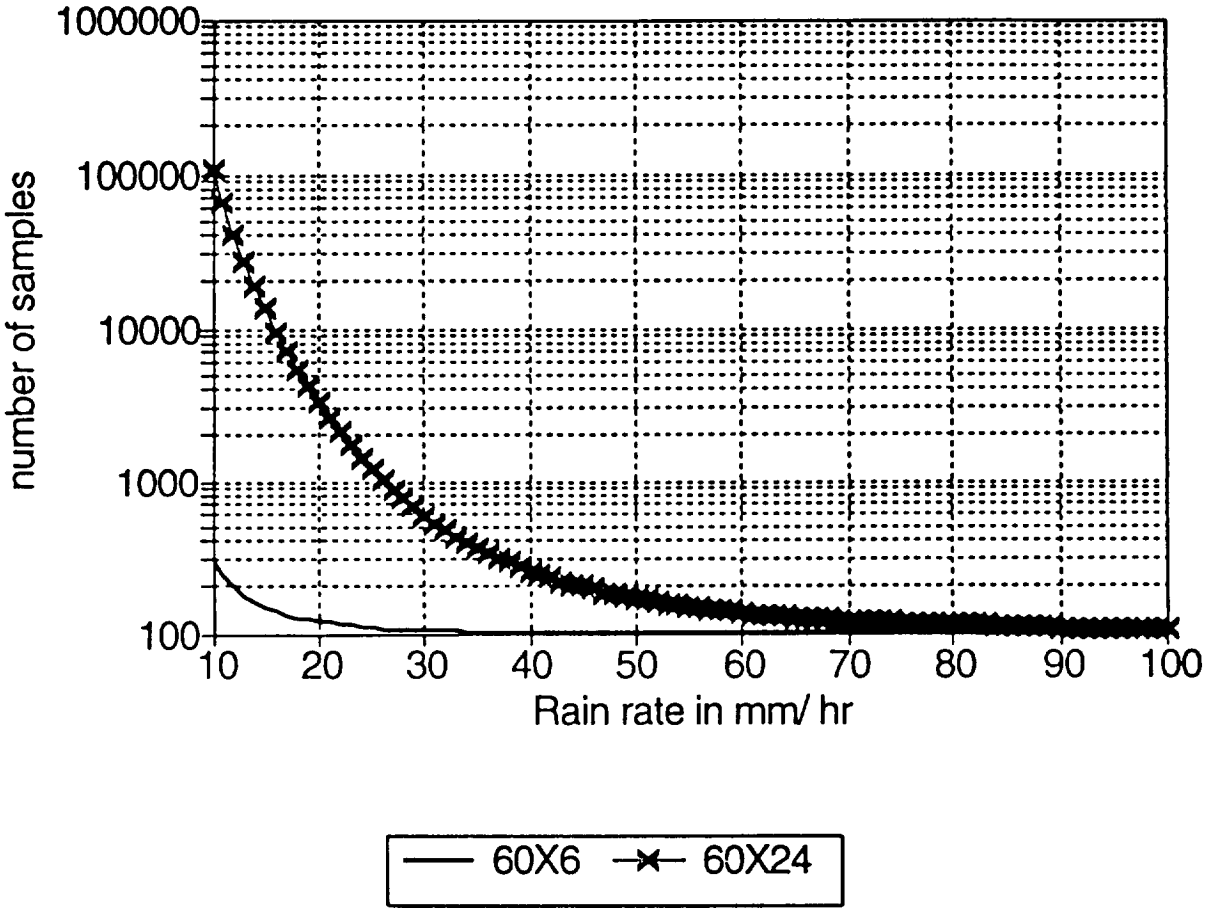

Fig. 6.1(a) Number of samples required to estimate the signal within 10% at 60°, X-Band for 6 m/s (60X6) and 24 m/s (60X24) cross wind.

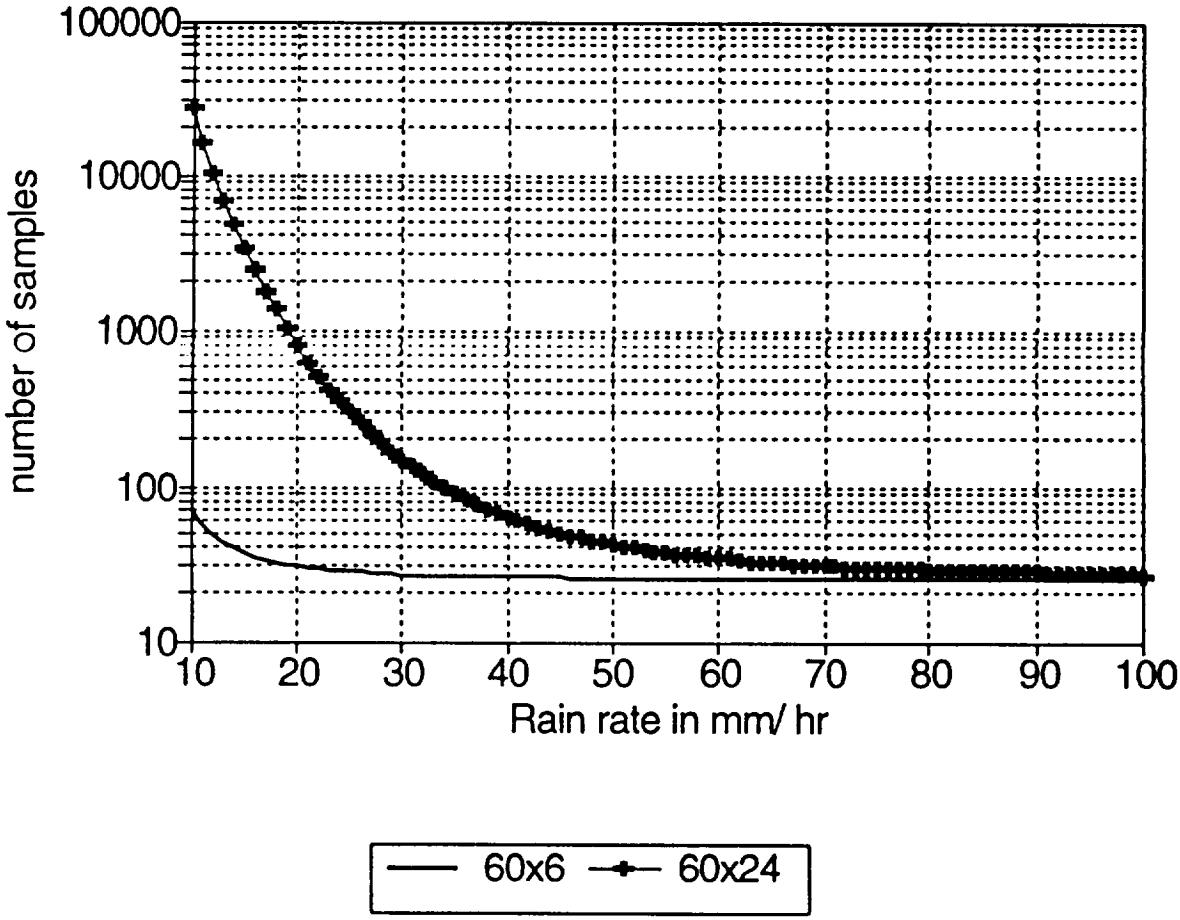

Fig. 6.1(b) Number of samples required to estimate the signal within 20% at 60°, X-Band for 6 m/s (60X6) and 24 m/s (60X24) cross wind.

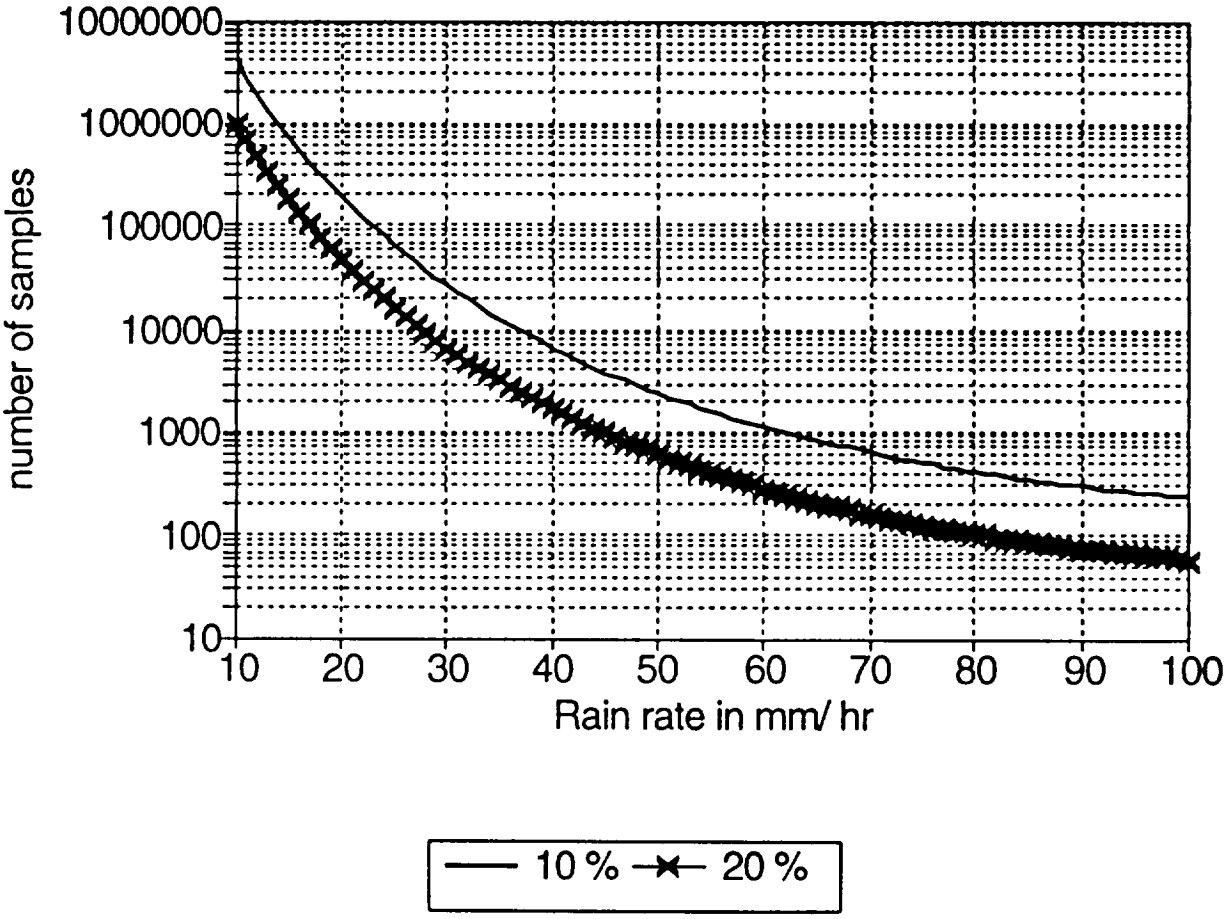

Fig. 6.1(c) Number of samples required to successfully estimate the signal at 60°, C-band, cross wind, for surface wind speed of 6 m/s at the given variance.

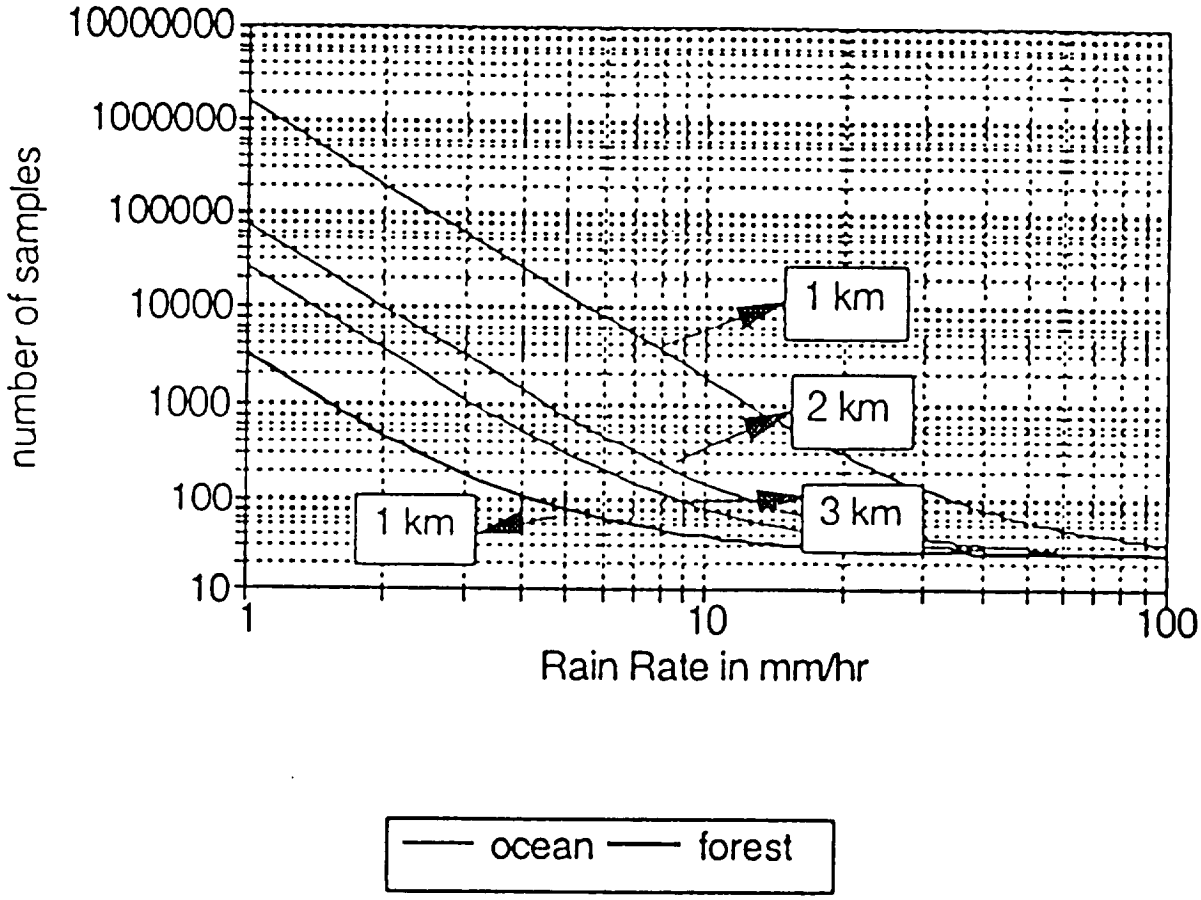

Fig. 6.2 Number of samples required to estimate the signal within 20% at vertical, X-Band.

For example, (6.11) shows that a change in SCR of 3 dB from -10 dB to -13 dB gives a fourfold increase in the number of samples required for successful signal estimation. Fig. 6.1(a) and 6.1(b) give us a bound of the required number of samples for different ocean-surface wind speeds at angle of incidence 60° at X band. Fig. 6.1(c) has the required number of samples for successful estimation of the signal for a wind speed of 6 m/s at C band. These plots give us an idea of the number of independent samples required to estimate the signal to within 10 % to
20 % accuracy at off-vertical angles of incidence. Here, for rain rates less than 10 mm/hr, the number of samples required is very large. This is because the SCR at these rain rates decreases to small values and the numerator of (6.11) increases rapidly. Fig. 6.2 has plots of the number of independent samples required at the vertical angle of incidence for different rain heights over the oceans and 6.2(b) has the same parameters at C band. As in the off-vertical case the number of samples required for successful estimation for rain rates > 5 mm/hr is very large, but feasible.

6.3 POSSIBLE NUMBER OF INDEPENDENT SAMPLES

Two approaches may be used to obtain independent samples in a SAR. In one approach the finest possible resolution r_{ap} is obtained and the resulting fine resolution image has these pixels averaged together. In another approach several looks are taken from slightly different directions, each with the final resolution r_{aa}, and these pixels are averaged together. In terms of the observation time we may write the number of

independent samples as

$$N_r = \Delta f_D \, T = \frac{2 \, \beta_h^2 \, R}{\lambda} \qquad (6.12)$$

which reduces to the simple relation

$$N_r = \frac{r_{aa}}{r_{ap}} \qquad (6.13)$$

6.31 OFF-VERTICAL ANGLES OF INCIDENCE

For the X-SAR the dimensions of the antenna are 12.1 x 0.3 m. The potential resolution is 6.05 meters. We write the actual azimuth resolution as

$$r_{aa} = \frac{2 \, \sigma_v \, R}{U} \qquad (6.14)$$

where β_h is assumed to be r_{aa} / R. Values of σ_v may go up to 6 m/s. The actual resolution, for an altitude of 215 km, r_{aa} is 688 meters at 60°, assuming 6 m/s turbulence. The number of samples available in azimuth is about 113. If we obtain N_R independent samples in the range by degrading the range resolution, the total number of independent samples available is $113N_R$. The effect of degradation of resolution on the SCR is minimal because any change in the surface area is offset by a corresponding change in the rain volume.

From Fig. 6.1(b), for the angle of incidence 60° and rain rate 10 mm/hr, the

number of samples required to estimate the clutter within 20 % is 30000 for a surface wind speed of 24 m/s. We have 113 samples in the azimuth and need about 300 in range. This number in range can be obtained by degrading the range resolution to 4500 m from the possible 15 m. For lower wind speeds the required number of independent samples is much smaller.

At 60°, C-band, for wind speed of 6 m/s (see Fig. 6.1(c)), using similar calculations, it is seen that the number of samples required to estimate the signal is enormously high. Hence the minimum detectable rain rate is still > 10 mm/hr.

6.32 VERTICAL INCIDENCE

The potential resolution of the X-SAR is 6.05 meters. We write actual the azimuth resolution as

$$r_{aa} = \frac{2\ \sigma_v\ R}{U} \qquad (6.15)$$

where β_h is assumed to be r_{aa} / R. Values of σ_v may go up to 6 m/s. The actual resolution, for an altitude of 215 km, r_{aa} is 344 meters at vertical. The number of samples available in azimuth is about 57. By degrading the range resolution and hence the range sidelobes, the total number of independent samples available is 57 N_R. However, since the number of rain cells available are limited in this case compared to off-vertical angles of incidence, the range resolution cannot be degraded to an arbitrarily large value.

Fig. 6.2 shows that, for a rain rate of 5 mm/hr, estimation within 20 % and a rain cell 3 km high, the number of samples required is 323. We have 57 samples in the azimuth and need about 6 in range. This number in range can be easily obtained by degrading the range resolution to 90 m from the possible 15 m. For a range cell 2 km high the corresponding numbers are 831 samples required with 15 in range and a degraded range resolution of 225 m. For a range cell 1 km high, however, the required number of samples is very large, and it is not possible to obtain a reasonable estimate for resolution cells below this height.

6.4 ESTIMATION OF THE SIGNAL

To obtain an estimate of the signal using this method, first a measurement of the signal and clutter is made from the rain volume. Then, with the same resolution, measurement of the clutter is made outside the rain volume. To obtain an adequate number of independent samples, the degradation of resolution may be performed during post-processing by averaging N_R x N_A samples.

The accuracy of the estimation heavily depends on the knowledge of the radar backscatter cross section in the presence and the absence of the rain. The ratio of the surface backscatter radar cross section in the presence of rain σ^o to that in the absence of rain σ^o_I is assumed to be unity. This, however, is a questionable assumption since the cross section is modified due to the impinging rain drops (Hansen, 1986). To overcome this limitation it is suggested that the estimation of the clutter be made in

the same rain volume but with the synthetic aperture. When the synthetic aperture is used, because of the narrow Doppler bandwidth, the interference due to rain is minimal. However, the rain appears as a noise component to the clutter estimate. This noisy clutter estimate is assumed to give better results than that obtained using the clutter estimate made outside the rain volume.

CHAPTER VII
CONCLUSIONS AND RECOMMENDATIONS

7.1 CONCLUSIONS AND RECOMMENDATIONS.

The limitation of the SIR-C/X-SAR experiment is inadequate SCR at low rain rates. At moderate rain rates, for off vertical look angles, there is adequate SCR if the angle of incidence is high ($\theta > 60^{o}$). At vertical due to the use of non-ideal weighting (raised $\cos^2$) of the chirp pulse causes range sidelobes that couple enormous amounts of clutter to the rain signal. However, if the experiment is over a dense forest, due to the smaller magnitude of the forest clutter, moderate to low rain rates may be detected (> 5 mm/hr). The altitude of the rain is also important; throughout the study it is assumed that the rain has an altitude of 3 km. Measurements with rain having smaller thickness are more affected at vertical. To overcome the clutter problem induced due to the use of the raised $\cos^2$ pulse, we recommend the use of a pulse that has very low and rapidly falling range sidelobes.

Another suggestion is to estimate the clutter and subtract the clutter from the combination of the signal and clutter. This is possible due to the availability of independent samples. The number of independent samples required to estimate the clutter to within 20 % is very large. However, this number can be obtained by degrading the resolution in both the range and the azimuth and by using multiple looks. Nevertheless, the resolution cannot be increased to an arbitrarily large value. As the resolution increases so does the size of the cell volume. Since the observable rain volume is fixed, the number of cells available for processing decreases. Further, as the cell size is increased, the probability of a cell being partially rain filled

increases. Partially rain filled cells have smaller returned signal power, which decreases the SCR. Thus, it is concluded that the minimum detectable rain rate is fixed to be > 10 mm at 60°. But for vertical angle of incidence rain rates > 5 mm can be detected.

In obtaining an estimate of the clutter, which involves taking a separate measurements in absence of rain, we assume that surface echo modification due to impinging rain drops is negligible. Further we assume that the ocean surface wind speeds are the same in the rain volume as they are outside it. Sometimes these assumptions, as in the case of convective storms, are not true and these are the limitations of this approach. To overcome this limitation it is suggested that the estimation of the clutter be made in the same rain volume but with a fully focussed synthetic aperture. When full focussing is used, because of the narrow Doppler bandwidth used for the surface echo, the interference due to rain is minimal. To illustrate this consider Fig. 7.1(a), the figure shows a rain drop's resultant velocity vector. Using some typical numbers to obtain the magnitude of the resultant the Doppler spectrum is shown in Fig. 7.1(b). Clearly the Doppler from the ground is wide enough apart from the Doppler due to the rain to allow separating them. However, the magnitude and direction of the wind determines the magnitude of the resultant velocity vector and hence the Doppler spectrum. Due to the Doppler shift caused by earth's rotation, it may sometimes be impossible to separate the two Doppler components.

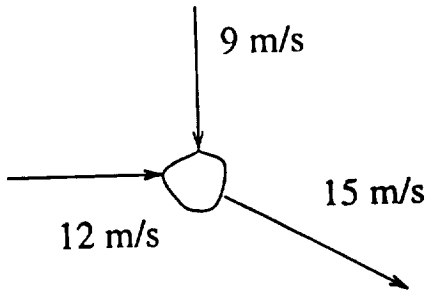

(a)The resultant velocity vector.

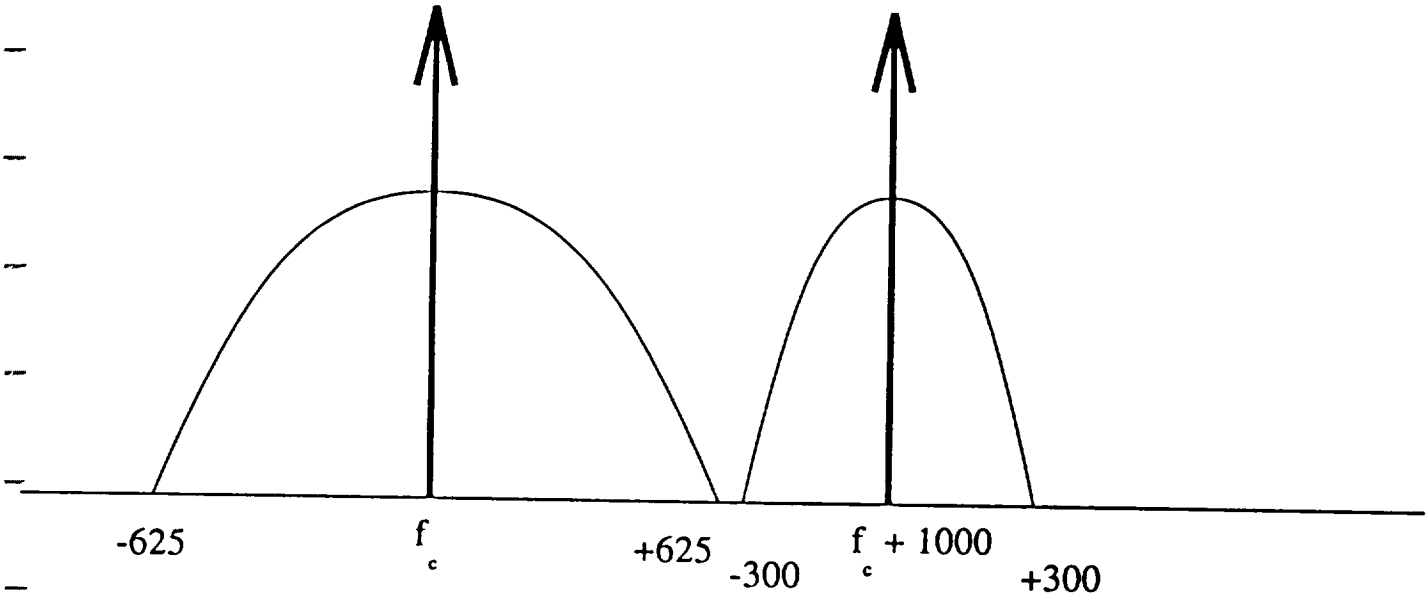

(b) The resultant Doppler.

Fig. 7.1 The Doppler spectrum from the surface and that from the falling rain drops is far enough apart to separate them.

However, this is a better approach to estimate the clutter component than estimating the clutter at a location where it is not raining.

Another approach that is feasible at vertical is try to eliminate the effect of the range sidelobes by transmitting a short pulse (chirped or not), but processing the returns without dechirping. A 3 μsec pulse was used during the SIR-C mission and the resulting resolution is 450 meters. Though no data are available at this point, it is certain that range cells as high as 500 meters above the ground have little or no clutter associated with their signal. However, since the rain thickness is 3 to 4 km the number of range cells available is limited.

APPENDIX - A

Drop diam (cm)	Rain rate (mm hr^{-1})	Percent of Total Volume								
		0.25	1.25	2.5	5	12.5	25	50	100	150
0.05		28.0	10.9	7.3	4.7	2.6	1.7	1.2	1.0	1.0
0.1		50.1	37.1	27.8	20.3	11.5	7.6	5.4	4.6	4.1
0.15		18.2	31.3	32.8	31.0	24.5	18.4	12.5	8.8	7.6
0.2		3.0	13.5	19.0	22.2	25.4	23.9	19.9	13.9	11.7
0.25		0.7	4.9	7.9	11.8	17.3	19.9	20.9	17.1	13.9
0.3			1.5	3.3	5.7	10.1	12.8	15.6	18.4	17.7
0.35			0.6	1.1	2.5	4.3	8.2	10.9	15.0	16.1
0.4			0.2	0.6	1.0	2.3	3.5	6.7	9.0	11.9
0.45				0.2	0.5	1.2	2.1	3.3	5.8	7.7
0.5					0.3	0.6	1.1	1.8	3.0	3.6
0.55						0.2	0.5	1.1	1.7	2.2
0.6							0.3	0.5	1.0	1.2
0.65								0.2	0.7	1.0
0.7										0.3

Table. 2.1 Laws-Parson drop-size distribution table for various precipitation rates. (Ulaby et, al., 1981).

$320A^{1.46}$	Wexler, R. (1947)	Washington, D.C.	8 rain intensities, each a mean of about 10 storms of same intensity
$214A^{1.46}$	Wexler (1948)	Washington, D.C.	98 storms – original data
$224A^{1.46}$		Yapalax, Great Britain	3 rainstorms
$630A^{1.46}$		Shawburyness, England	4 rainstorms
$200A^{1.46}$		Hawaii	30 storms, orographic rain
$190A^{1.46}$	Marshall, Langille, and Palmer (1947)	Various locations	Various types of rain
$220A^{1.46}$	Marshall and Palmer (1948)	Various locations	Various types of rain
$295A^{1.496}$	Hood (1930)	Canada	270 samples, 7 rainstorms; light rain 1–3 mm/hr; heavy thunderstorms 50 mm/hr
$180A^{1.48}$	Boucher (1951)	Cambridge, Mass.	63 rain samples, widespread rain both uniform and variable, showers and thunderstorms
$127A^{1.48}$	Higgs (1952)	Australia	Showers, 8 months of observation
$16.6A^{1.48}$	Blanchard (1953)	Hawaii	Orographic rain within cloud
$31A^{1.48}$			Orographic rain at cloud base
$290A^{1.48}$			Nonorographic rain – thunderstorms
$396A^{1.5}$	Jones (1953)	Central Illinois	1,270 1-minute observations – all rains
$484A^{1.49}$			360 1-minute observations – thunderstorms
$380A^{1.46}$			330 1-minute observations – rain showers
$313A^{1.48}$			380 1-minute observations – continuous rain
$130A^{1.48}$	Litvinov (1956)	Mount El'brus, USSR	Rain (melted granular snow and strongly granulated particles), 344 spectra, 6 rains
$237A^{1.48}$			Rain (melted snow of average granulations), 367 spectra, 7 rains
$398A^{1.49}$			Rain (melted non-granulated snow), 148 spectra, 4 rains
$162A^{1.48}$	Atlas and Chmela (1957)	Lexington, Mass.	Stratiform rain, 16 April 1954
$213A^{1.48}$			Stratiform rain, 23 April 1954
$350A^{1.48}$			Stratiform rain, 27 April 1954
$310A^{1.48}$			Stratiform rains, 28 April 1954
$230A^{1.48}$	Sal'man (1957)	Near Leningrad, USSR	Showers and steady rain
$303A^{1.5}$	Shupiatskii (1957)	Near Moscow, USSR	Various types of rain, $R < 7$ mm/hr
$403A^{1.49}$			Various types of rain, $7 < R < 60$ mm/hr
$259A^{1.48}$			Various types of rain, $R > 60$ mm/hr
$109A^{1.48}$	Ramana Murty and Gupta (1959)	Kandla, India	Orographic, Monsoon rains
$342A^{1.48}$		Delhi, India	Nonorographic, Monsoon rains
$700A^{1.5}$	Imai (1960)	Tokyo, Japan	One day, probably warm rain
$300A^{1.5}$			One day continuous rain
$200A^{1.5}$			Air mass showers
$200A^{1.5}$			Prewarm frontal rain
$219A^{1.48}$	Sivaramakrishnan (1961)	Poona, India	Thunderstorms
$67.6A^{1.48}$			Steady rains
$66.5A^{1.48}$			Warm rains
$204A^{1.48}$	Mochnik (1961)	Kiev, USSR	Showers and steady rains
$203A^{1.48}$	Fujiwara (1965)	Mostly Miami, Florida	Continuous rain
$300A^{1.48}$			Rainshowers
$450A^{1.48}$			Thunderstorms
$184A^{1.48}$	Deem (1966)	Various locations	
$238A^{1.48}$		Entebbe, Uganda	
$240A^{1.48}$		Luiza, Congo	
$176A^{1.48}$		Palma	
$151A^{1.48}$		Barra, Italy	
$179A^{1.48}$		Karlsruhe, Germany	Spring
$227A^{1.48}$		Karlsruhe, Germany	Summer
$175A^{1.48}$		Karlsruhe, Germany	Fall
$130A^{1.48}$		Karlsruhe, Germany	Winter
$137A^{1.48}$		Axel Heiberg Land	
$310A^{1.48}$	Gorelik et al. (1967)	Chernozem (near Moscow)	About 10 days, 20,000 samples on filter paper, all types of rain
$295A^{1.48}$		Vashcovo (3 km away)	32 showers and thunderstorms on mountain peak, 2,500 meters
$320A^{1.48}$	Foote (1964)	Tucson, Arizona	Measured on 12 March 1964
$230A^{1.48}$	Doumouliu and Cogombles (1966)	France	Measured on 4 September 1964
$253A^{1.48}$		France	107 drop size distributions
$426A^{1.48}$		France	
$286A^{1.48}$	Mueller and Sims (1966)	Miami, Florida	
$221A^{1.48}$		Majuro, Marshall Islands	
$301A^{1.48}$		Corvallis, Oregon	
$311A^{1.48}$		Bogar, Indonesia	
$267A^{1.48}$	Sims and Mueller (1968)	Woody Island, Alaska	
$230A^{1.48}$		Franklin, North Carolina	
$372A^{1.48}$		Champaign, Illinois	
$391A^{1.48}$		Flagstaff, Arizona	
$256A^{1.48}$		Island Beach, N.J.	
$140A^{1.5}$	Joss et al. (1970)	Locarno-Monti, Switzerland	Drizzle
$230A^{1.5}$			Widespread rain
$500A^{1.5}$			Thunderstorm rain

Table. 2.2 Empirical relations between reflectivity factor Z_e (mm^6/m^3) and rain fall rate in mm/hr. (Battan 1973)

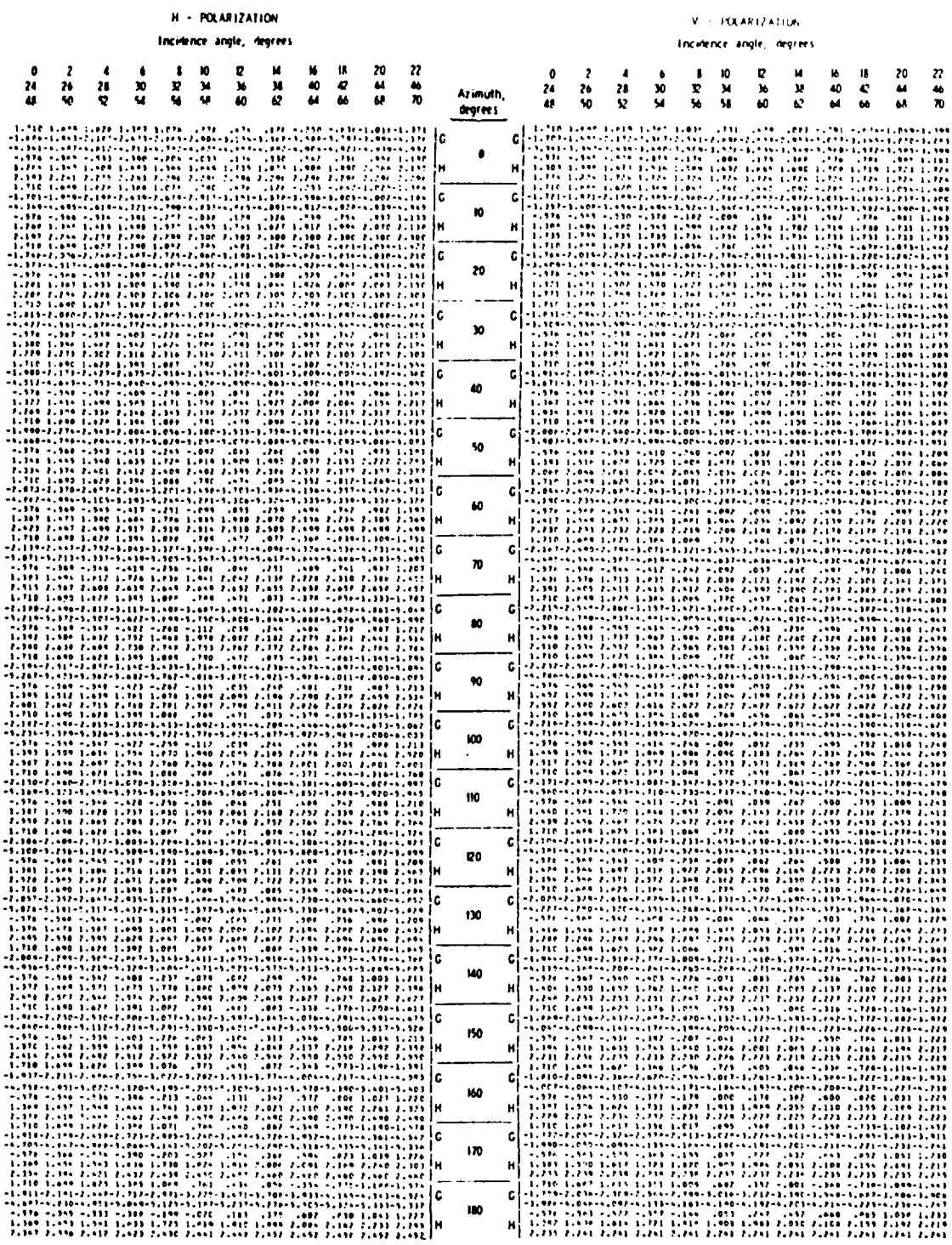

Table. 3.1(a) G and H coefficients used in the SASS model. These coefficients depend on wind direction and angle of incidence.

The CMOD4 Model Formulation and Coefficients

The form of the ECMWF CMOD4 model is:

$$\sigma^{o}_{km} = b_0.(1 + b_1 \cos\phi + b_3 \tanh b_2 . \cos 2\phi)^{1.6}$$

where:

$$b_0 = b_r.10^{\alpha + \gamma.\mathcal{F}^1(V,\theta)}$$

and

$$\mathcal{F}^1(y) = \begin{cases} 0 & \text{if } y \le 0 \\ \log y & \text{if } 0 < y \le 5 \\ \sqrt{y}/3.2 & \text{if } y > 5 \end{cases}$$

and $\alpha, \beta, \gamma, b_1, b_2$ and b_3 are expanded as Legendre polynomials to a total of 18 coefficients. b_r is a residual correction factor to b_0, and is given as a look-up table as a function of incidence angle.

$$\begin{aligned} \alpha &= c_1 P_0 + c_2 P_1 + c_3 P_2 \\ \gamma &= c_4 P_0 + c_5 P_1 + c_6 P_2 \\ \beta &= c_7 P_0 + c_8 P_1 + c_9 P_2 \\ b_1 &= c_{10} P_0 + c_{11}.V + (c_{12} P_0 + c_{13}.V).\mathcal{F}^2(x) \\ b_2 &= c_{14} P_0 + c_{15}.(1 + P_1).V \\ b_3 &= 0.42(1 + c_{16}(c_{17} + x)(c_{18} + V)) \\ b_r &= LUT(\theta) \\ \mathcal{F}^2(x) &= \tanh\{+2.5(x + 0.35)\} - 0.61(x + 0.35) \end{aligned}$$

where the Legendre polynomals in x are:

$$P_0 = 1 \qquad P_1 = x \qquad P_2 = (3x^2 - 1)/2 \qquad \text{with } x = (\theta - 40)/25$$

V is the wind speed in ms^{-1}, ϕ the relative wind direction in degrees and θ the incidence angle in degrees.

CMOD4 Coefficients

Model:		CMOD4
α	c_1	-2.301523
	c_2	-1.632686
	c_3	0.761210
γ	c_4	1.156619
	c_5	0.595955
	c_6	-0.293819
β	c_7	-1.015244
	c_8	0.342175
	c_9	-0.500786
b_1	c_{10}	0.014430
	c_{11}	0.002484
	c_{12}	0.074450
	c_{13}	0.004023
b_2	c_{14}	0.148810
	c_{15}	0.089286
b_3	c_{16}	-0.006667
	c_{17}	3.000000
	c_{18}	-10.00000

Residual Factors for CMOD4

θ°	b_r	θ°	b_r	θ°	b_r
16	1.076	31	0.927	46	1.054
17	1.076	32	0.923	47	1.053
18	1.075	33	0.930	48	1.052
19	1.072	34	0.937	49	1.047
20	1.069	35	0.944	50	1.038
21	1.066	36	0.955	51	1.028
22	1.056	37	0.967	52	1.016
23	1.030	38	0.978	53	1.002
24	1.004	39	0.988	54	0.989
25	0.979	40	0.998	55	0.965
26	0.967	41	1.009	56	0.941
27	0.958	42	1.021	57	0.929
28	0.949	43	1.033	58	0.929
29	0.941	44	1.042	59	0.929
30	0.934	45	1.050	60	0.929

Table. 3.1(b) Coefficients used in the CMOD-4 model.

Quantity	Temperature (°C)	Wavelength (Cm)			
		10	3.21	1.24	0.62
n	20	8.88	8.14	6.15	4.44
	10	9.02	7.80	5.45	3.94
	0	8.99	7.14	4.75	3.45
	− 8	. . . . .	6.48	4.15	3.10
κ	20	0.63	2.00	2.86	2.59
	10	0.90	2.44	2.90	2.37
	0	1.47	2.89	2.77	2.04
	− 8	. . . . .	. . . . .	2.55	1.77
$\lvert K\rvert^2$	20	0.928	0.9275	0.9193	0.8926
	10	0.9313	0.9282	0.9152	0.8726
	0	0.9340	0.9300	0.9055	0.8312
	− 8	. . . . .	. . . . .	0.8902	0.7921
$\mathrm{Im}(-K)$ . . .	20	0.00474	0.01883	0.0471	0.0915
	10	0.00688	0.0247	0.0615	0.1142
	0	0.01102	0.0335	0.0807	0.1441
	− 8	. . . . .	. . . . .	0.1036	0.1713

Source: Gunn and East 1954.

Table 3.2 $|K|^2$, and the imaginary part of (-K) of water as a function of temperature and wavelength.

Wavelength (Cm)	R Interval (Mm/Hr)	M-P (0°C)	Z_e (Mm^6/M^3) Gunn and East (18C)	Mueller and Jones (0°C)
0.62	0–5	$240R^{1.5}$	.....	$450R$
	5–20	$345R^{0.9}$	.....	.....
	20–100	$540R^{0.78}$	.....	.....
0.86	0–5	$350R^{1.32}$	.....	$950R$
	5–20	$450R^{1.15}$	.....	.....
	20–100	$780R^{0.95}$	.....	.....
1.24	0–5	$356R^{1.5}$	.....	$1280R$
	5–20	$460R^{1.35}$	.....	.....
	20–100	$820R^{1.15}$	.....	.....
1.87	0–20	$330R^{1.54}$	.....	$1150R$
	20–50	$500R^{1.4}$	.....	.....
	50–100	$750R^{1.2}$	.....	.....
3.21	.....	$275R^{1.55}$	$310R^{1.36}$	$890R$
4.67	.....	$280R^{1.45}$	.....	$860R$
5.5	.....	$280R^{1.45}$	.....	$860R$
5.7	.....	.....	$210R^{1.6}$	.....
10	.....	$295R^{1.45}$	$210R^{1.6}$	$810R$

Source: Wexler and Atlas 1963.

Table 3.3 Z_e-R relations calculated using Mie Scattering. (Battan 1973)

Frequency (GHz)	Logarithmic model[a] κ_l V	κ_l H	b V	b H	Linear model κ_l	Comments[b]
2.8	0.000459		0.954		—	(1)
7.5	0.00459		1.06		0.00481	(1)
9.4	0.0087		1.10		0.00932	(1)
11.0	0.012	0.014	1.23	1.24	—	(2)
16.0	0.0374		1.10	1.24	0.0403	(1)
18.0	0.053	0.061	1.07	1.10	—	(2)
24.0	0.10	0.11	1.03	1.06	—	(2)
30.0	0.17	0.19	0.98	1.00	—	(2)
34.9	0.225		1.05		0.234	(1)
40.0	0.31	0.38	0.91	0.93	—	(2)
60.0	0.63	0.71	0.81	0.82	—	(2)
69.7	0.729		0.893		—	(1)
80.0	0.86	0.93	0.76	0.77	—	(2)
100.0	1.06	1.15	0.73	0.73	—	(2)

[a]The symbols V and H refer to vertical and horizontal polarizations.

[b](1) Computed for spherical particles by Crane (1971); (2) computed for oblate spheroidal drops, reported by Harden et al. (1978).

Table 3.4 Values of parameters in the relationships $k_{er} = \kappa_l R_r^b$, both log and linear models.

REFERENCES

Atlas, D., C. Elachi, and W.E Brown, Jr., "Precipitation mapping with an airborne synthetic aperture radar," *Journal of Geophysical Research*, vol 82, pp.3445-3451, 1977.

Atlas, D., O.W. Thiele, *Precipitation measurement from space*, Workshop report, NASA Goddar Flight Center, Greenbelt, MD, 1981.

Atlas, D. and R.K. Moore, "The measurement of precipitation with the synthetic aperture radar," *Journal of Atmospheric and Oceanic Technology*, vol.4, pp.368-376, 1987.

Atlas, D., D. Rosenfeld, and D. B. Wolff, "Climatologically tuned reflectivity-rain rate relations and links to area-time integral," *American Meteorology: 24th conference on radar meteorology*, Tallahassee, Florida, March 27-31, 1989.

Barrett, E.C., and D.W Martin, "The use of satellite data in rainfall monitoring," Academic press, London, pp.340, 1981.

Battan, L.J., *Radar Observation of the Atmosphere*, University of Chicago Press; Chicago, 1973.

Blivens, L.F. and G.Norcross, "Effects of rainfall on scatterometer derived wind speeds," *IGARSS'88 Digest*, vol I, pp.565-567, 1988.

Chan, H.L. and A.K. Fung, "A theory of sea scatter at large incidence angles," *Journal of Geophysical Res.*, vol. 82, pp.3429-3444, 1977.

Chong, M., P. Amayenc, G. Scialom, and J .Testud, "A tropical squall line observed during the COPT 81 experiment in west Africa. Part I: Kinematic structure inferred from Dual-Doppler Radar Data," *Monthly Weather review*, vol.115, pp.670-694, 1987.

Chui, L.S., "Rain estimation from satellites: Area rainfall-area relation," third Conf. satellite Metro. and Oceanog., *Amer. Metro. Soc.*, Anaheim California, pp.363-368, Feb 1-5, 1988.

Crane, R.K., and D.W. Blood, *Hand book for the estimation of microwave propagation effects-link calculations for earth paths*, Environmental Research Technology Inc., Concord, MA. Rep. P-7376-TR1, pp.80, 1979.

Fujita, Masaharu, "An algorithm for estimating rain rate by dual frequency radar," *Radio Science*, vol 18, Number 5, pp.697-708, sept-oct 1983.

Fuk Li, Personal communication, 1994.

Gamache, J.F., and R. A. Houze, Jr., "Mesoscale air motions associated with a tropical squall line," *Monthly Weather Review*, vol 110, pp.118-135, 1982.

Goldhirsh, J., and J.R. Rowland, "A tutorial assessment of atmospheric height uncertainties for high-precision satellite altimeter missions to monitor ocean currents," *IEEE Trans. Geo. and Rem. Sens.*, vol. GE-20, pp.418-434, 1982.

Goldhirsh, J., "Analysis of algorithms for retrieval of rain-rate profiles from a space borne dual wavelength radar," *IEEE Trans. on Geo. and Rem. Sensing*, vol. 26, no.2, pp.98-114, 1988.

Gunn, K.L.S., and T.W.R. East, "The Microwave Precipitation of particles," *Quart. J .Royal Meteorol. Soc.*, 80, pp. 522-545, 1954.

Griffith, C.G., W.L. Woodley, P.G. Grube, D.W. Martin, J.Stout, and D.N.Sidkar, "Rain estimation from geosynchronous satellite imagery-visible and IR studies," *Mon. Weather rev.*, 106, pp.1153-1171, 1978.

Hansen, J.P., "Rain backscatter test dispel old theories," *Microwaves and RF*, vol. 25, pp.97-102, June 1986.

Im, K.E. and D. Atlas, "The estimation of precipitation intensity in the presence of surface backscatter and the converse using a spaceborne radar," presented at the International Symposium on Tropical Precipitation Measurements, Tokyo, 1987.

Jones, W.L., L.C Schroeder, and J.L. Mitchell, "Aircraft measurement of the anisotropic scattering signature over the ocean for the JONSWAP and 1976 east coast missions," NASA TMX 28646, 1978.

Jones, W.L and L.C. Schroeder, "Radar backscatter from the ocean: dependence on surface friction velocity," *Boundary Layer Meteorology* vol. 13, pp.133-149, 1978(b).

Kieu, Duc, *Radar rainfall measurements from space*, Phd Dissertation, The University of Kansas, 1991.

Kummerow, C., *Microwave radiance from horizontally finite, vertically structured precipitation clouds*, PhD thesis, University of Minnesota, pp.146, 1987.

Lin, S.H, "A method for calculating rain attenuation distributions on microwave paths," *Bell Syst. Tech. J.* , 54, pp 1051-1086, 1975.

Meneghinini, R, J. Eckerman, and D. Atlas, "Determination of rain rate from a spaceborne radar using measurements of total attenuation," *IEEE Transactions on Geoscience and Remote Sensing*, vol. GE-21, number 1, January 1983.

Meneghinini, R, and D. Atlas "Simultaneous ocean cross section and rainfall measurements from space with a nadir-looking radar," *Journal of Atmospheric and Oceanic Technology*, vol.3, pp.400-413, September 1986.

Meneghinini, R, Kozu T, *Spaceborne Weather Radars*, Artech House: Norwood MA, 1990.

Moore, R.K., and J.D Young, "Active Microwave Measurements from Space of Sea Surface Winds," *IEEE J. Ocean. Engr.*, OE-2, pp.309-317, 1977.

Moore, R.K., A.K. Fung, G.J. Dome, and I.J. Birrer, " Estimation of Oceanic Surface Wind Speed and Direction Using Orthogonal Beam Scatterometer, Measurements and Comparison of Recent Sea Scattering Theories," University of Kansas Remote Sensing Laboratory Technical Report TR 186-17, 1978.

Moore, R.K., Y.S. Yu, A.K. Fung, D. Kaneko, G.J. Dome, and R.E. Werp "Preliminary study of rain effects on rain scattering from water surfaces," *IEEE J. Ocean. Engr.*, vol. OE-4, pp.31-31, 1979.

Morrison, J.A and M. J Cross, "Scattering of a plane Electromagnetic wave by axi-Symmetric rain-drops," *Bell Syst. Tech. J.*, 53 pp 955-1020, 1974 North, G R., *Tropical Rain Mapping Radar (TRAMAR) Volume I*, A proposal to the National Aeronautics and Space Administration for the announcement of opportunity No. OSSA-1-88 on the earth observing system (Eos), Texas A&M University, July 1988.

Olson, W.S., "Model-based retrieval of tropical cyclone rainfall rates using th Nimbus-7 SMRR," Second conference of satellite meteorology/remote sensing applications, American Meteorology society, Williamsburg, VA, pp.438-443, 1986.

Schroeder, L.C.,D. H. Boggs, G. Dome, I. M.Halberstam, W. L. Jones, W. J. Pierson, and F. J. Wentz, " The relationship between wind vector and normalized radar cross-section used to derive SEASAT-A satellite scatterometer winds," *J. Geophysical Res.*, 87, pp. 3318-3336, 1982.

Schroeder, L.C., P.R. Send, J.L. Mitchell, and L.W Jones, "AAFE RADSCAT 13.9 G-Hz measurements and analysis: Wind-speed signature of the ocean," *IEEE J. Ocean. Engr.*, vol OE-10 no.4, pp.346-357, 1985.

Soofi.K, "Clutter model for land, forest, snow, sea ice and ocean," RSL Tech. Report 2923-2,1978.

Spencer, R.W., "A satellite passive 37 GHz scattering based method for measuring oceanic rain rates," *Journal of Climatological and Applied Meteorology*, 25, pp.754-766, 1986.

Stuart, M. A, *Radar sensitivity and antenna scan pattern study for a satellite based radar wind sounder*, MS thesis, University of Kansas, 1992.

Thiele, O.W., ed.:On requirements for a satellite mission to measure tropical rainfall, NASA Ref.publ. No. 1183, pp.49, 1987.

Ulaby, F.T., R.K. Moore, and A.K. Fung, *Microwave Remote Sensing*, Vol I Artech House:Norwood, MA, 1981.

Ulaby, F.T., R.K. Moore, and A.K. Fung, *Microwave Remote Sensing*, Vol II Artech House:Norwood, MA, 1982.

Ulaby, F.T., R.K. Moore, and A.K. Fung, *Microwave Remote Sensing*, Vol III Artech House:Norwood, MA, 1986.

Weinman, J. A., R. Meneghini, and K. Nakamura, "Retrieval of precipitation profiles from an airborne radar and passive radiometer measurements: comparison with dual-frequency radar measurements," *Journal of Applied Meteorology*, August 1989.

Wiley, C.A., personal communication, 1967.